LBNL-44715

ERNEST ORLANDO LAWRENCE
BERKELEY NATIONAL LABORATORY

Photodissociation Spectroscopy and Dynamics of Free Radicals, Clusters, and Ions

Hyeon Choi

Chemical Sciences Division

RECEIVED
APR 12 2000
OSTI

December 1999

Ph.D. Thesis

DISCLAIMER

This document was prepared as an account of work sponsored by the United States Government. While this document is believed to contain correct information, neither the United States Government nor any agency thereof, nor The Regents of the University of California, nor any of their employees, makes any warranty, express or implied, or assumes any legal responsibility for the accuracy, completeness, or usefulness of any information, apparatus, product, or process disclosed, or represents that its use would not infringe privately owned rights. Reference herein to any specific commercial product, process, or service by its trade name, trademark, manufacturer, or otherwise, does not necessarily constitute or imply its endorsement, recommendation, or favoring by the United States Government or any agency thereof, or The Regents of the University of California. The views and opinions of authors expressed herein do not necessarily state or reflect those of the United States Government or any agency thereof, or The Regents of the University of California.

Ernest Orlando Lawrence Berkeley National Laboratory
is an equal opportunity employer.

DISCLAIMER

Portions of this document may be illegible in electronic image products. Images are produced from the best available original document.

LBNL-44715

Photodissociation Spectroscopy and Dynamics of Free Radicals, Clusters, and Ions

Hyeon Choi
Ph.D. Thesis

Department of Chemistry
University of California, Berkeley

and

Chemical Sciences Division
Ernest Orlando Lawrence Berkeley National Laboratory
University of California
Berkeley, CA 94720

December 1999

This work was supported by the Director, Office of Science, Office of Basic Energy Sciences, Chemical Sciences Division, of the U.S. Department of Energy under Contract No. DE-AC03-76SF00098.

Photodissociation spectroscopy and dynamics of Free Radicals, Clusters, and Ions

by

Hyeon Choi

Bachelor of Science (Seoul National University) 1991

A dissertation submitted in partial satisfaction of the

requirements for the degree of

Doctor of Philosophy

in

Chemistry

in the

GRADUATE DIVISION

of the

UNIVERSITY OF CALIFORNIA, BERKELEY

Committee in charge:

Professor Daniel M. Neumark, chair

Professor C. Bradley Moore

Professor Robert W. Dibble

Photodissociation spectroscopy and dynamics of Free Radicals, Clusters, and Ions

Copyright © 1999

by

Hyeon Choi

The U.S. Department of Energy has the right to use this thesis for any purpose whatsoever including the right to reproduce all or any part thereof

ABSTRACT

Photodissociation spectroscopy and dynamics of Free Radicals, Clusters, and Ions

by

Hyeon Choi

Doctor of Philosophy in Chemistry

University of California, Berkeley

Professor Daniel M. Neumark, Chair

The photodissociation spectroscopy and dynamics of free radicals and ions is studied to characterize the dissociative electronic states in these species. To accomplish this, a special method of radical production, based on the photodetachment of the corresponding negative ion, has been combined with the technique of fast beam photofragment translational spectroscopy. The photofragment yield as a function of photon energy is obtained, mapping out the dissociative and predissociative electronic states. Branching ratios to various product channels, the translational energy distributions of the fragments, and bond dissociation energies are then determined at selected photon energies. The detailed picture of photodissociation dynamics is provided with the aid of *ab initio* calculations and a statistical model to interpret the observed data.

Important reaction intermediates in combustion reactions have been studied: CCO, C_2H_5O, and linear C_n (n=4-6).

The spectroscopy and dissociation dynamics of the CCO radical following excitation of the $\tilde{A}\ ^3\Pi \leftarrow \tilde{X}\ ^3\Sigma^-$ and $\tilde{c}\ ^3\Pi \leftarrow \tilde{a}\ ^3\Sigma^-$ electronic transitions are investigated. Analysis of the translational energy distribution yields the accurate value for the C-CO bond dissociation energy and heat of formation of CCO. Consideration of the potential energy surfaces indicates that the $C(^3P)$ +$CO(X\ ^1\Sigma^+)$ products are produced via radiationless transitions to the $\tilde{X}\ ^3\Sigma^-$ state.

The dominant channel in ethoxy dissociation following ultraviolet excitation is $C_2H_5O \rightarrow C_2H_3+H_2O$. The translational distribution for $C_2H_3+H_2O$ from ethoxy dissociation shows that the electronically excited state of product is produced larger than or equal to 5.51eV.

The photofragment yield (PFY) spectra for linear carbon clusters (C_n, n=4-6) consist of several continua spanning the whole visible and ultraviolet region. The product mass distributions for dissociation of C_n clusters are dominated by C_3 and its partner fragment C_{n-3}, although some minor channels are also identified for dissociation of C_4 and C_5 clusters. The PFY spectra and $P(E_T)$ distributions indicate that multi-photon dissociation occurs at photon energies below the dissociation threshold, and that both single- and multi-photon dissociation occur above the threshold. The one-photon components of the $P(E_T)$ distributions can be modeled by phase space theory (PST), suggesting that photoexcitation is followed by internal conversion to the ground state.

In addition, the photodissociation of a negative ion, I_3^-, and radical, I_3, are also explored. These molecules photodissociate into channels with two different photofragment mass ratio: 1:1 and 1:2 mass ratios. Based on our detection scheme and appearance of sharp peak in translational distribution for channel with 1:1 mass ratio, this

channel is assigned as a symmetric three-body dissociation. The $P(E_T)$ distributions with 1:2 mass ratio from the photodissociation of I_3^- and I_3 show that electronic transitions produce the I_2^- ($\tilde{X}$) or I_2 in various electronic states along with atomic I in its $^2P_{3/2}$ or $^2P_{1/2}$ state.

This thesis is dedicated

to

My Father and Mother.

Table of Contents

Acknowledgments

Chapter 1: Introduction 1

Photodissociation Studies 1

Fast Photofragment Translational Spectrometer 4

Limitation by Fragment mass resolution 7

Summary 8

References 10

Chapter 2: Photodissociation of triplet and singlet states of the CCO radical 12

I. Introduction 13

II. Experimental Details 16

III. Results 19

A. Photoelectron spectrum of CCO^- anion 19

B. Photofragment yield spectrum 21

C. Translational energy distribution of photofragments 24

D. *Ab initio* calculations 26

IV. Analysis 28

A. Photofragment yield spectrum 28

B. Translational energy distributions 31

1. CCO thermochemistry 31

2. Product energy distributions 33

V. Discussion 34

VI. Conclusions..... 37

Acknowledgements..... 39

References..... 39

Chapter 3: Photodissociation dynamics of the Ethoxy radical (C_2H_5O)..... 43

I. Introduction..... 44

II. Experimental Setup..... 46

III. Results..... 49

A. Photofragment yield (PFY) spectrum of C_2H_5O..... 49

B. Product mass distribution..... 50

C. Translational Energy $P(E_T)$ distributions of C_2H_5O and C_2D_5O..... 51

IV. Discussion..... 54

A. Origin of the diffuse band in the PFY spectrum..... 54

B. Dissociation Mechanism..... 57

V. Conclusions..... 62

Acknowledgements..... 63

References..... 63

Chapter 4: PHOTODISSOCIATION OF LINEAR CARBON CLUSTERS C_n (n=4-6)..... 67

I. Introduction..... 68

II. Experimental..... 71

III. Results..... 74

A. Spectroscopy..... 74

B. Photofragment mass distributions 76

C. Translational Energy $P(E_T)$ distributions 76

IV. Analysis 81

V. Discussion 90

VI. Conclusions 93

Acknowledgements 95

References 96

Chapter 5: Photodissociation Dynamics of Triiodide anion (I_3^-) ... 101

I. Introduction 102

II. Experimental Setup 105

III. Results 107

A. Photofragment Yield (PFY) Spectrum 107

B. Photodissociation dynamics of I_3^- 109

1. Photofragment mass ratio (m_1/m_2) 109

2. 1:2 mass channel 112

3. 1:1 mass channel 115

IV. Classical Trajectory calculation for symmetric three-body dissociation of I_3^- 118

V. Discussion 121

A. PFY Spectrum 121

B. Photodissociation dynamics of I_3^- 122

VI. Conclusions 125

Acknowledgements 125

References.....126

Chapter 6: Photodissociation Dynamics of Triiodide radical (I_3)..129

I. Introduction..... 130

II. Experimental Setup..... 131

III. Results..... 134

A. Photoelectron Spectrum of I_3^- anions.....134

B. Photodissociation of I_3 radical..... 137

1. Photofragment mass ratio (m_1/m_2).....139

2. 1:2 mass channel..... 141

3. 1:1 mass channel..... 144

IV. Discussion.....146

Acknowledgements..... 148

References..... 148

Appendix: Fortran Code for Phase-Space theory calculation.....151

Acknowledgment

I first thank Professor Daniel Neumark for allowing me to join his group. His constant support and encouragement make my work in this Thesis possible and my life at Berkeley more pleasant.

I am very fortunate to work with outstanding colleague on FRBM project. Dr. David Osborn was my first mentor in gas phase. When I joined this project five and half years ago, I did not have any clue how to do experiment in the gas phase. He was such a perfectionist to teach me every single detail in a very organized way. Right now, he is in Sandia National Laboratory and I am sure that he will have a wonderful career. Ryan Bise joined this project one year later than I and has a tremendous effect on our project. He is one who thought about changing detachment photon energy to generate the electronically excited state of neutral. His idea makes CCO paper (Chapter 2) more fruitful. Alexandra Hoops is our new member in this project. She is so patient and becomes familiar with machine very fast. She even had her own data in the very short period of time. I wish Ryan and Alex best luck in the FRBM project and their careers.

I joined this group with Travis Taylor and Martin Zanni. Fortunately, all of three graduate at the same time. Even though we worked in the different project, we had a chance to study the same molecule – I_3^- and I_3. Actually, Marty and Travis persuade me to study these molecules and it produced very interesting results such as symmetric three-body dissociation. During this study, I really enjoyed discussion with them.

I am not very good at computers. Therefore, I got tremendous help from Michel Furlanetto and Harry Gomez, who manage the UNIX and PC in our group. My ignorance on computer often bothers them and they are always kind to answer my stupid questions.

Alison Davis, Harry Gomez, Nick Pivonka and Jason Robinson joined this group at the same time and brought lots of spirit to our group. I wish that they also have a chance to graduate at the same time as Marty, Travis, and I do now.

I have a great opportunity to share the knowledge on chemistry with wonderful Post Doc: Dr. Knut Asmis, Dr. Christian Frischkorn, Dr. Thomas Lenzer, and Dr. Weizhong Sun.

I thank Professor Seong Keun Kim in Seoul National University who was my former advisor in Korea. He introduced me into Physical Chemistry.

I would like to thank Lisa Torres, Cheryn Gliebe and Noreen Buyes, three wonderful administrative assistants associated with Dan's group. I also thank Eric Granlund of machine shop who gave me numerous tips on machining.

Special thanks must go to my preliminary exam committee: Professor Bradley Moore (Chair), Professor Evan Williams, Professor Martin Head-Gordon and Professor Robert Dibble (Mechanical Engineering).

I am very lucky to have a very supportive family, who lives in Korea. Especially, my father called me every single day and his constant care help me go through lots of obstacle in my graduate life. Finally, I want to thank my lovely wife, Youri Kang, who always stands by me and supports me.

Chapter 1. Introduction

Free radicals are chemical species with non-zero spin. Most of radicals are chemically unstable even though they are physically stable; that is, if undisturbed by collisions they do not spontaneously decompose. Therefore, radicals have a short lifetime in the gaseous phase under ordinary laboratory conditions.

Some of these radicals play important roles in various chemical reactions, such as combustion and chemistry in atmosphere. Therefore, it is very critical to characterize these radicals. However, both the inability to generate such species purely and their high reactivity have hindered the study of these radicals.[1]

In spite of these difficulties, spectroscopy on the bound states of these radicals has been extensively investigated.[2] However, limited amount of work have been done on the dissociative states of free radicals. Therefore, we investigate the dissociative states of free radicals using photofragment translational spectroscopy. Through this method, we measure the dissociation cross-section as a function of photon energy to map out the dissociative states, identify the photofragment to determine the product channels and branching ratio, and measure the translational distribution of fragments for each channel to study the photodissociation dynamics.

Photodissociation studies

Photodissociation experiments have become one of the most valuable tools in chemical physics for the purpose of understanding how excited electronic states coupled to the dissociation asymptote. These experiments and the theory developed to explain them have yielded considerable insight into the variety of dynamical processes that

occurs subsequent to electronic excitation.[3] From these studies, one hopes to obtain the bond dissociation energies, characterize the symmetry of the excited state, measure the product branching ratios, and determine if the excited state undergoes direct dissociation on an excited state surface or internal conversion to the ground state followed by statistical decay to products.

The vast majority of photodissociation studies measure either the product quantum-state distributions or translational energy and angular distributions of the products. For state-specific detection of product, laser-induced fluorescence (LIF), multiphoton ionization (MPI), and coherent anti-stokes Raman scattering (CARS) have provided extremely detailed information on the dynamics of photodissociation, which are nicely reviewed by Butler and Neumark.[4] However, the vast majority of photofragments cannot be detected by these methods. There are many reasons for that. First, the identities of all the products of the photolysis must be well known. Second, these molecules must have optical transitions that can be efficiently probed. Third, their line strengths and transition frequencies must be well characterized.

For most polyatomic photofragments one or more of these conditions cannot be satisfied. Even when they are, because of the large excess of energy disposed into the products, a great deal of knowledge on spectroscopy of these products may be required. In addition, for highly internally excited molecules the density of states may be too high to resolve the product state distributions.

Another direction to study the photodissociation is to measure the translational energy of photofragments, which we employ in this thesis. This technique was originally developed by Wilson and coworkers[5] and significantly improved over the last thirty

years.[4,6-8] In this method, they measured the time required for one of photofragment to travel from the interaction region of the laser and molecular beam to the detector by using the detector consisting of an electron-bombardment ionizer followed by mass spectrometer. In this configuration, any neutral photofragment, including reactive radicals, can be detected regardless of its internal energy and is thus termed as a universal detector. Using the linear momentum conservation of the dissociation of the parent molecule, the measured flight information of one photofragment can be converted into the translational energy of photofragments.

Because of the universality of this detector, this translational spectrometer has been successfully applied to study the closed-shell molecules, such as CH_3I[9] and H_2S,[8] which successfully resolved the vibrational progression of CH_3 and rovibrational state of SH photoproduct. However, there are two problems to study the radicals with this method: First, the dissociation inherent in the ionization process has made it difficult to distinguish experimentally between daughter ions from electron-impact-induced dissociative ionization and photon-induced fragmentation of primary photoproduct. Second, there is no appropriate way to generate the pure radical source. Recently, the several experiments have been successfully done using the pyrolysis source to produce the high density of hydrocarbon radicals, such as CH_3,[10] C_3H_5,[11] C_3H_3,[12] and C_2H_5.[13] However, for most of studies, the radicals of interest are generated by photolysis of closed shell precursor. In this process, it can generate various radicals and chemical reaction products along with radicals of interest.

In our experiment, we overcome these problems to use the photodetachment of the mass-selected anion. The free radical has unpaired electron, so that corresponding

anions are usually stable. Therefore, we first generate stable anions with a combination of fast electron beam and pulsed electric discharge. Only anions of interest are selected by time-of-flight mass spectrometer and photodetached just above the detachment threshold. In this way, we can generate the pure source of radicals in the vibrationally ground state. Also, anions are accelerated up to 6-8keV before the detachment, so that the photofragments generated from photodissociation of radicals also have the large kinetic energy (1-4 keV) in the laboratory frame, which makes the detection efficiency up to 50% and independent of mass or chemical composition with a microchannel plate.[14] In our experiment, we are detecting two photofragments from one parent radical in coincidence. In this scheme, our data collection rate must be less than one dissociation event out of 10 laser shots. Therefore, despite of low density (10^3~10^4/cm^3) of radicals produced by photodetachment of anions, our experimental scheme is very sensitive to study the photodissociation dynamics.

Fast Photofragment Translational Spectrometer

The fast photofragment translational spectrometer, constructed for these study by Cyr, Osborn, and Neumark,[15,16] is shown in Fig. 1. A complete description of this apparatus is given in the PhD. Dissertation of Douglas Cyr.[17]

Fast Radical Beam Machine

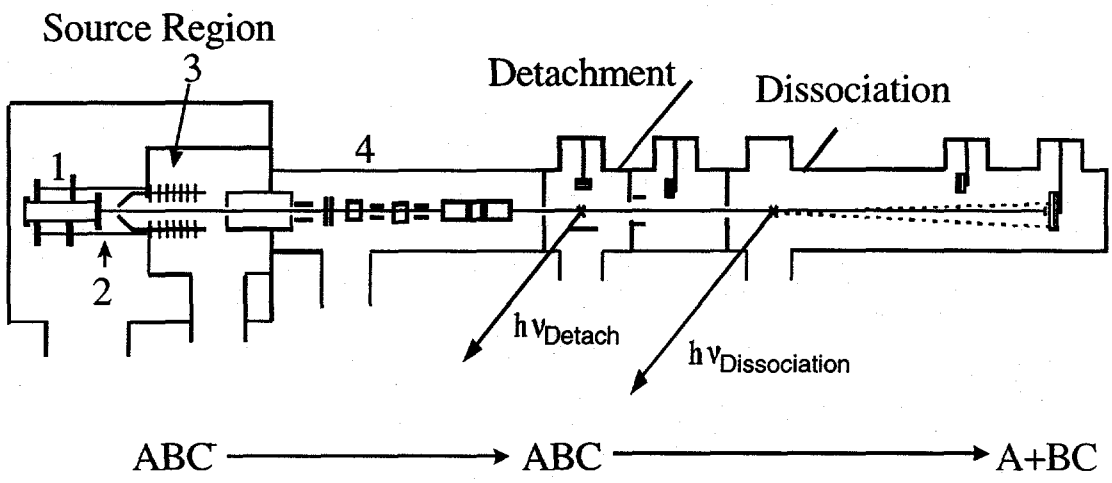

Figure 2 : Schematic of fast radical beam photofragment translational spectrometer. 1. Pulsed valve, 2. Electric discharge, 3. Acceleration plates, 4. Bakker-type time-of-flight mass spectrometer. Detachment, dissociation and detection regions are also indicated.

Briefly, a gas mixture including precusor for ions of interest supersonically expands into the source chamber through a pulse valve operating at 60 Hz. Ions are generated in the throat of the ensuing supersonic expansion by either 1 keV electron beam from electron gun or a pulsed electronic discharge. Ions formed are cooled by the supersonic expansion to their ground vibrational state and to a rotational temperature of 35-50K.

The ion beam passes through a skimmer and is accelerated to high laboratory energy (typically 6-8 keV). The anions of interest are selected by a Bakker type time-of-flight mass spectrometer and photodetached with a pulsed dye laser to create the corresponding neutral. The energy of the detachment laser is just above the threshold of anions, so that only radicals in their vibrationally ground states are generated. The remaining ions are deflected from the beam.

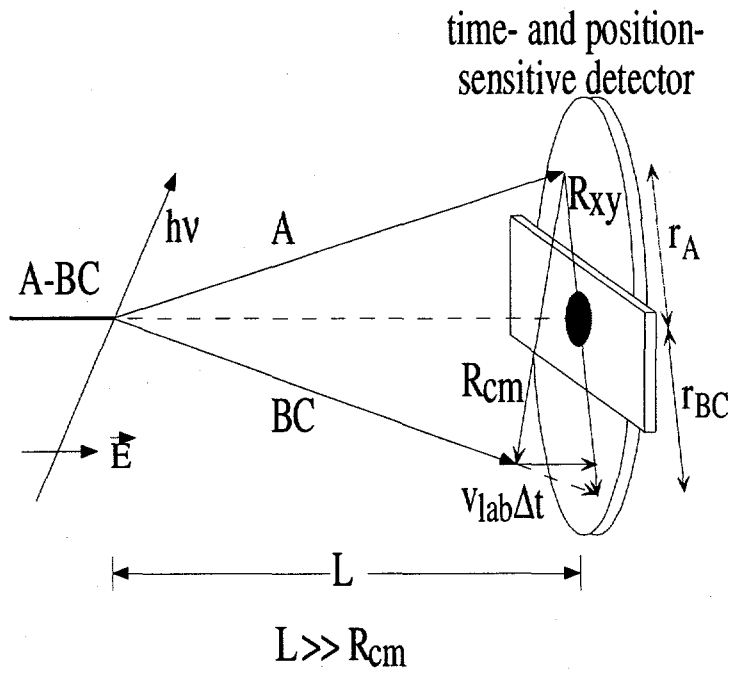

Figure 2: Kinematics of photodissociation using the time- and position-sensitive detector.

The radicals are collimated by another 1.0 mm pinhole and intersect a second pulsed laser. If photodissociation occurs, fragments recoiling out of the parent radical beam are detected with high sensitivity, *without* an ionization step, using microchannel plate detectors. A beam block immediately in front of the detector stops the remaining neutral beam. Photodissociation occurs under collisionless conditions (10^{-9} Torr), and two types of experiments are performed. First, the photofragment yield spectrum is obtained by integrating the total fragment flux as a function of photodissociation laser wavelength. Second, at selected fixed photon energies, the dissociation dynamics are investigated by detecting both fragments *in coincidence* from dissociation of a single parent radical.

In this experiment, three parameters are measured using the time- and position-sensitive detector: the difference in fragment arrival times at the detector, τ, and the distances from the center of the parent neutral beam to each fragment on the detector

face, r_A and r_{BC}. These three quantities can then be analytically converted to the desired experimental quantities, namely the fragment masses (m_A and m_{BC}), their relative translational energy (E_T), and their scattering angle (θ) with respect to the $\vec{E}$ vector of the dissociation laser. The kinematics of the process shown in Fig. 2 are described by the equations:

$$\frac{m_A}{m_{BC}} = \frac{r_{BC}}{r_A}\left(1 - \frac{v_0\tau}{L}\right) \tag{1}$$

$$E_T = E_0 \cdot \frac{m_A m_{BC}}{(m_A + m_{BC})^2} \cdot \frac{\left[(v_0\tau)^2 + (r_A + r_{BC})^2\right]}{L^2} \tag{2}$$

$$\theta = \arctan\left(\frac{r_A + r_{BC}}{v_0\tau}\right), \tag{3}$$

where E_0, v_0 and L are the energy and velocity of parent neutral beam and distance from the photolysis interaction region to the detector.

Limitation by Fragment mass resolution

We consider the fragment mass resolution. According to equation (1), fragment masses (m_A and m_{BC}) depend on the distance (r_A and r_{BC}) from the center of the beam to fragment and time difference (τ) in their arrival at the detector. Our detector has excellent spatial (~0.14mm) and time resolution (0.5ns), which enable us to determine the r_A+r_{BC} and τ with that accuracy. However, accuracy on the individual distance, r_A and r_{BC}, is limited by the size of parent radical beam, which is determined by two 1mm pin hole inside the machine. Therefore, the fragment mass resolution can be determined by following equation:

$$\frac{m_A}{\Delta m_A} \approx \frac{r_{BC}}{\Delta r_{BC}}. \tag{4}$$

Assuming $\tau = 0$, equation (4) can be expressed as a function of E_T by using equation (2).

$$\frac{m_A}{\Delta m_A} \approx \frac{L}{\Delta r_{BC}} \cdot \left(\frac{m_A}{m_{BC}}\right)^{1/2} \cdot \left(\frac{E_T}{E_0}\right)^{1/2}. \tag{5}$$

In the normal experimental condition ($L = 1000$ mm, $\Delta r_{BC} = 1$ mm, $E_0 = 8000$ eV, $E_T =$ 1eV, and $m_A = m_{BC}$), the fragment mass resolution ($m_A/\Delta m_A$) is 11.2.

In our photodissociation study on the simple radical, such as CCO, C_n (n = 4-6), and I_3, only one or two dissociation channels with very different fragment mass are energetically possible. Therefore, the fragment mass resolution is still enough to identify the fragment mass. However, as the number of atoms in radical increases, especially the number of hydrogen atoms, such as in C_2H_5O, it increases the number of dissociation channels with similar fragment mass, which are energetically possible in our experimental condition. In this case, our mass distribution fails to identify the fragment mass and other supplementary method is needed, like experiments with isotope substitution.

Summary

Photodissociation of free radicals is qualitatively different from that on closed-shell molecule for two principal reasons. First, due to their open-shell electronic structure, radical tend to have low-lying electronic states. This increased state number density will results in a higher probability of surface crossings following the photoexcitation. Therefore, photodissociation of free radicals cannot be often explained by a single-potential energy surface and can be model systems for study of these non-

adiabatic processes. Second, open-shell molecules often dissociate to an open-shell and a closed-shell pair of fragments, which implies that the dissociation energies of free radicals are typically less than for similar closed-shell molecules. The photon energy (3-6 eV) we use in our experiment is often enough to generate electronically excited photoproducts.

In this thesis, we present photodissociation studies of CCO, linear carbon clusters (C_n, n=4-6), C_2H_5O, I_3^- and I_3. In Chapter 2, the photodissociation from $\tilde{A}\ ^3\Pi - \tilde{X}\ ^3\Sigma^-$ and $\tilde{c}\ ^1\Pi - \tilde{a}\ ^1\Delta$ electronic transitions of CCO radical has been studied. Especially, the first excited singlet state ($\tilde{a}\ ^1\Delta$) of CCO radical, which has been postulated as the reaction intermediate in hydrocarbon combustion, is produced by changing photodetachment energy and investigate the photodissociation of CCO after the electronic transition to the $\tilde{c}\ ^1\Pi$ of CCO. In Chapter 3, the photodissociation spectroscopy and dynamics of linear carbon clusters (C_n, n=4-6) are investigated. In this study, we observe absorption over much of the whole visible and ultraviolet. This is due to the vibronic and symmetry forbidden transition of linear carbon clusters, which are very uncommon in this small size of molecules. We also find linear carbon clusters dissociates after absorbing one or more than two photon. The $P(E_T)$ distribution from one-photon process is successfully described by phase-space theory, indicating dissociation occurs on the ground state after internal conversion. In Chapter 4, photodissociation of C_2H_5O radicals is investigated. Surprisingly, the C_2H_5O radical dominantly dissociates into $C_2H_3 + H_2O$. Through the analysis of $P(E_T)$ distribution, it reveals that the isomerization of C_2H_5O on the excited state before the dissociation is very important and production of electronically excited state of C_2H_3 products is

proposed. In Chapter 5 and 6, we present the photodissociation studies on I_3^- and I_3. In these studies, we found these two molecules undergo symmetric three-body dissociation after the electronic excitation. Also, photodissciation studies of these molecules reveal an abundance of non-adiabatic processes.

References

[1] G. Herzberg, *The Spectra and Structure of Simple Free Radicals* (Cornell University Press, New York, 1971).

[2] M. E. Jacox, *Vibrational and electronic energy levels of polyatomic transient molecues* (American Institute of Physics, New York, 1994).

[3] R. Schinke, *Photodissociation Dynamics* (Cambridge University Press, Cambridge, 1993).

[4] L. J. Butler and D. M. Neumark, J. Phys, Chem. **100,** 12801 (1996).

[5] G. E. Busch, J. F. Cornelius, R. T. Mahoney, R. I. Morse, D. W. Schlosser, and K. R. Wilson, Rev. Sci. Instrum. **41,** 1066 (1970).

[6] A. M. Wodtke and Y. T. Lee, in *Molecular Photodissociation Dynamics*, edited by M. N. R. Ashfold and J. E. Baggot (Royal Society of Chemistry, London, 1987), pp. .

[7] R. N. Zare, Mol. Photochem. **4,** 1 (1972).

[8] L. Schnieder, W. Meier, K. H. Welge, M. N. R. Ashfold, and C. M. Western, J. Chem. Phys. **92,** 7027 (1990).

[9] R. K. Sparks, K. Shobatake, L. R. Carlson, and Y. T. Lee, J. Chem. Phys. **75,** 3838 (1981).

[10] S. W. North, D. A. Blank, P. M. Chu, and Y. T. Lee, J. Chem. Phys. **102,** 792 (1995).

[11] H. Deyerl, I. Fischer, and P. Chen, J. Chem. Phys, **119,** 1450 (1999).

[12] H. Deyerl, I. Fischer, and P. Chen, J. Chem. Phys. **111,** 3441 (1999).

[13] T. Gilbert, T. L. Grebner, I. Fischer, and P. Chen, J. Chem. Phys. **110,** 5485 (1999).

[14] H. Kerstein, (FOM-Institute for Atomic and Molecular Physics, Amsterdam, 1987).

[15] R. E. Continetti, D. R. Cyr, R. B. Metz, and D. M. Neumark, Chem. Phys. Lett. **182,** 406 (1991).

[16] R. E. Continetti, D. R. Cyr, D. L. Osborn, D. J. Leahy, and D. M. Neumark, J. Chem. Phys. **99,** 2616 (1993).

[17] D. R. Cyr, Ph.D., University of California, 1993.

Chapter 2. Photodissociation of excited triplet and singlet states of the CCO radical

Abstract

The triplet and singlet states of the ketenylidene (CCO) radical are investigated using fast radical beam photofragment translational spectroscopy, in which CCO is generated by laser photodetachment of CCO^- and subsequently photodissociated, and anion photoelectron spectroscopy. In the photodissociation experiment, two bands in which the upper state of CCO predissociates are studied. Photodissociation from excitation of the $\tilde{A}\ ^3\Pi - \tilde{X}\ ^3\Sigma^-$ band in CCO is observed from 16,666 – 23,529 cm^{-1}; resonances are observed and assigned to excited vibrational levels involving all three vibrational modes. We also report the first observation of the $\tilde{c}\ ^1\Pi - \tilde{a}\ ^1\Delta$ band in CCO. Here, the $\tilde{a}\ ^1\Delta$ state of CCO is generated by laser photodetachment at higher photon energy than was used to generate the $\tilde{X}\ ^3\Sigma$ state. The $\tilde{c}\ ^1\Pi$ state is approximately located by photoelectron spectroscopy of CCO^-, and the photodissociation experiment shows that the origin of the $\tilde{c}\ ^1\Pi - \tilde{a}\ ^1\Delta$ band occurs around 17,170 cm^{-1}. Kinetic energy release spectra from both bands yield accurate values for the C—CO bond dissociation energy and heat of formation of CCO: D_0(C—CO) = 2.24 ± 0.02 eV (51.7 ± 0.5 kcal/mol) and $\Delta H^0_{f,298}$ (CCO) = 4.04 ± 0.02 eV (91.1 ± 0.5 kcal/mol). Although the kinetic energy distributions resulting from excitation to the $\tilde{A}\ ^3\Pi$ and $\tilde{c}\ ^1\Pi$ states are clearly non-statistical, consideration of the potential energy surfaces indicates that dissociation from both states occurs via radiationless transitions to the $\tilde{X}\ ^3\Sigma^-$ state.

I. Introduction

The ketenylidene (CCO) radical is an important reaction intermediate in interstellar cloud formation[1-3] and hydrocarbon combustion.[4-6] There is also growing interest in metal ketenylidene (CCO) complexes which can facilitate C-O, C-C and C-H bond formation and cleavage in organometallic chemistry.[7] Two unresolved issues are addressed in this article. First, large uncertainties have existed in the heat of formation of CCO, hindering our understanding of these fundamental reaction mechanisms. Secondly, although many reactions are believed to proceed via singlet CCO species, a lack of spectroscopic information on the singlet states of CCO has prevented the identification of any singlet CCO radicals. In this paper, we address these two issues using a combination of photofragment translational spectroscopy and photoelectron spectroscopy.

The CCO radical was first identified spectroscopically by Jacox *et al.*[8] Its infrared spectrum was observed in a matrix isolation experiment and the CCO ground state was tentatively assigned to be a $^3\Sigma^-$ state. In addition, an unstructured absorption was seen near 500 nm which was attributed to CCO photodissociation, an interpretation supported by the depletion of the CCO absorption when the matrix was irradiated at that wavelength. The gas phase absorption spectrum of CCO was subsequently recorded by Devillers and Ramsay.[9] They observed a rotationally resolved band with origin at 11,651 cm^{-1} and assigned it to the $\tilde{A}\ ^3\Pi - \tilde{X}\ ^3\Sigma^-$ transition, obtaining spectroscopic constants for both states. Laser induced fluorescence (LIF),[10] microwave[11] and near IR spectroscopy[12-16] were used to further establish the vibrational frequencies and spectroscopic constants for the $\tilde{X}\ ^3\Sigma^-$ and the $\tilde{A}\ ^3\Pi$ states.

The photoelectron spectrum of CCO^- was first taken by Oakes *et al.*[17] and the electron affinity of CCO was determined as 1.848 ± 0.003 eV. A more recent photoelectron spectrum by Zengin *et al.*[18] showed the electron affinity to be 2.29 ± 0.02 eV; the earlier value was attributed to vibrational hot bands.

CCO is known to have several low-lying singlet states in addition to the $\tilde{A}\,^3\Pi$ state. Walch[19] used polarization-configuration-interaction (POL-CI) with generalized valence bond (GVB) theory to characterize the triplet and singlet states. Chabalowski *et al.*[20] also performed calculations at the multi-reference double-excitation (MRCI) method.

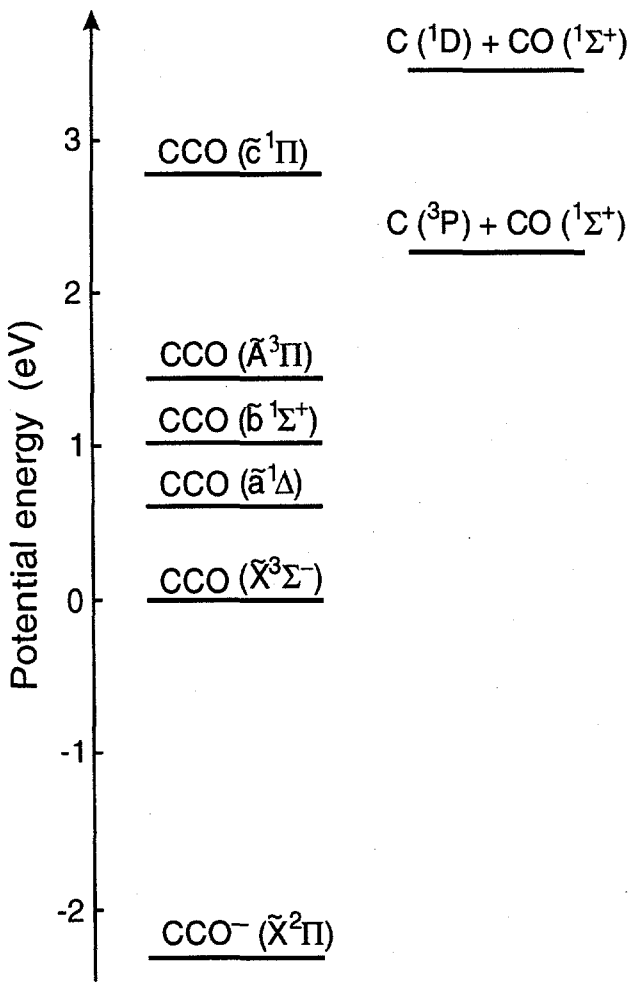

Figure 1 : Energetics of CCO electronic states

According to these studies, the molecular orbital configuration … $(6\sigma)^2\,(1\pi)^4\,(7\sigma)^2\,(2\pi)^2$ leads to the $\tilde{X}\ ^3\Sigma^-$, $\tilde{a}\ ^1\Delta$, and $\tilde{b}\ ^1\Sigma^+$ states, and the $\tilde{A}\ ^3\Pi$ and $\tilde{c}\ ^1\Pi$ states are derived from the …$(6\sigma)^2\,(1\pi)^4\,(7\sigma)^1\,(2\pi)^3$ configuration. The energy ordering of the five electronic states is shown in Fig. 1. While the singlet states are not accessible by optical excitation from the $\tilde{X}\ ^3\Sigma^-$ state, they are accessible by anion photodetachment; the molecular orbital configuration for the $\tilde{X}\ ^2\Pi$ ground state of CCO^-

is $(\ldots 6\sigma^2 1\pi^4 7\sigma^2 2\pi^3)$. Term values for the $\tilde{a}\ ^1\Delta$ and $\tilde{b}\ ^1\Sigma^+$ states were experimentally determined from the CCO^- photoelectron spectrum by Zengin *et al*;[18] the higher lying $\tilde{c}\ ^1\Pi$ state was apparently too high in energy to be seen at their highest photodetachment energy, 4.66 eV.

The heat of formation of CCO has been determined in several ways. The apparent photodissociation at 500 nm seen by Jacox *et al.*[8] places a lower limit of 3.7 eV on its heat of formation. Becker and Bayes[4,5] observed CO chemiluminescence from the O + CCO reaction; based on this, along with the observation of Jacox, they deduced the CCO heat of formation to be 4.0 ± 0.2 eV. Both of these values are at variance with the 1985 "literature value" [21] of 2.9 ± 0.7 eV, obtained from the decomposition rate of C_3O_2.[22] However, the earlier values are in good agreement with recent values from *ab initio* calculation (3.86 eV)[19] and combined electron affinity and gas phase acidity measurements[18,23] (4.0 ± 0.2 eV). In this paper, we confirm and further refine the higher value for the CCO heat of formation.

Although experiment and theory have established the existence of low-lying singlet states in CCO, no optical transitions between these states have been observed. The absence of a spectroscopic probe for singlet CCO species has hindered verification of proposed reaction mechanisms in combustion, interstellar clouds and photolysis of C_3O_2. For example, the ground states of C_3O_2 and CO molecules are $^1\Sigma^+$ states, so the formation of triplet CCO from the photolysis of C_3O_2 [24-32] is spin-forbidden. Triplet CCO radicals are not observed under collisionless photolysis conditions, but are seen in the presence of collisions, presumably due to collisional quenching of singlet CCO.[10,27,29]

In this paper, we investigate the photodissociation spectroscopy and dynamics of triplet and singlet CCO using our fast radical beam photofragment translational spectrometer. In this experiment, CCO is generated by photodetachment of CCO^- and subsequently photodissociated. In all prior investigations of this type, care was taken to photodetach the ions at sufficiently low energy so that only ground state radicals are produced. This scheme is used to generate CCO $\tilde{X}\ ^3\Sigma^-$ and we observe dissociation from upper state excited vibrational levels of the $\tilde{A}\ ^3\Pi$ - $\tilde{X}\ ^3\Sigma^-$ band. In addition, we demonstrate that we can generate the CCO $\tilde{a}\ ^1\Delta$ state by photodetachment at higher energy, and thus identify the $\tilde{c}\ ^1\Pi - \tilde{a}\ ^1\Delta$ transition for the first time. This work on the singlet state is aided considerably by photoelectron spectroscopy of CCO^- at a higher photon energy than used by Zengin *et al.*,[18] enabling us to determine the approximate location of the $\tilde{c}\ ^1\Pi$ state prior to performing the photodissociation experiments.

II. Experimental Details

Two different instruments, a negative ion photoelectron spectrometer and a fast radical beam photofragment translational spectrometer, are used for this study. In both, the CCO^- anion is produced by electrical discharge of C_3O_2 molecules. C_3O_2 is synthesized by the dehydration of malonic acid with phosphorus pentoxide, as described by Brauer.[33] Ne gas (40 psi) flows over C_3O_2 which is kept in a glass bubbler cooled in a acetone/dry ice bath. The resultant mixture supersonically expands through a pulsed value and electrical discharge[34] into the source region of the apparatus. A pulsed electrical discharge (-700 V) forms CCO^- anions; the discharge occurs in the beginning of supersonic expansion and the CCO^- anion are made and cooled to 20-50K.

Fast Radical Beam Machine

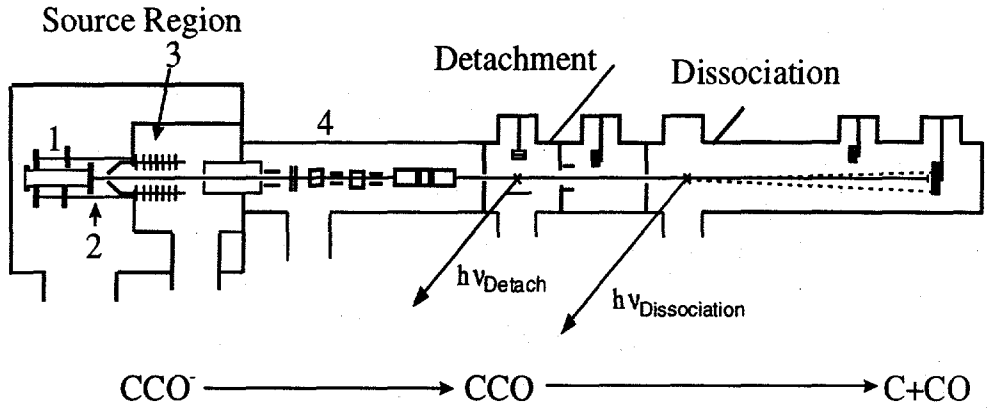

Figure 2 : Schematic of fast radical beam photofragment translational spectrometer. 1. Pulsed valve, 2. Electric discharge, 3. Acceleration plates, 4. Bakker-type time-of-flight mass spectrometer. Detachment, dissociation and detection regions are also indicated.

A detailed description of the photoelectron spectrometer is given elsewhere[35,36] Briefly, negative ions generated in the ion source are injected into a time-of-flight mass spectrometer using a pulsed electric field. The ions separate in time and space according to their mass-to-charge ratio and are detected with a microchannel plate detector. The ion of interest is selectively photodetached using the fifth harmonic (5.822 eV) of a pulsed Nd:YAG laser. After detachment the kinetic energy of the electrons is determined by time-of-flight analysis, as described by Xu *et al.*[36] The instrumental resolution is 8 meV at 0.65 eV and degrades as $(eKE)^{3/2}$.

CCO photodissociation was studied using the fast radical beam photofragment spectrometer shown in Fig. 2. The experimental apparatus has been described in detail previously.[37,38] Negative ions formed in the source region are accelerated to 6 keV and separated temporally by a time-of-flight (TOF) mass spectrometer. The CCO^- ion packet is intersected by an excimer pumped pulsed dye laser beam, photodetaching some anions

to yield neutral CCO radicals. By changing the photodetachment energy, we can selectively detach CCO^- to make either ground $\tilde{X}\ ^3\Sigma^-$ state only or ground $\tilde{X}\ ^3\Sigma^-$ state plus $\tilde{a}\ ^1\Delta$ state of CCO. Any remaining ions are removed by the application of an electrical deflection pulse. The neutral beam is then crossed by a second excimer-pumped tunable dye laser beam. Some neutrals absorb a photon and dissociate. These photofragments are detected by microchannel plates. The high center-of-mass kinetic energy (6 keV) allows the fragment to be detected with high efficiency (~50%). The overall experiment is summarized as:

$$CCO \xrightarrow{h\nu\ (\text{detach})} CCO \xrightarrow{h\nu\ (dissociate)} C + CO \qquad (1)$$

Two types of experiment are performed. The photofragment yield (PFY) spectrum is obtained by collecting the total flux of fragments as a function of the photodissociation laser wavelength. We also probe the photodissociation dynamics by detecting both fragments in coincidence from a single parent CCO at a fixed photon energy for photodissociation. Using a time- and position-sensitive (TPS) wedge-and-strip anode detector[37] to measure the separation between the fragments and the interval between their arrival times, we obtain the kinetic energy release and scattering angle for each dissociation event. From this the translational energy distribution $P(E_T)$ is determined. Because of the low translational energy release for this system, a very limited range of scattering angles is probed in this experiment, so angular distributions are not reported.

III. Results

In this section, the experimental results are summarized, followed by *ab initio* calculations on the CCO radical. Specifically, the photoelectron spectrum of CCO^- at 5.822 eV is presented. The PFY spectra of CCO radicals are shown for the $\tilde{A}\ ^3\Pi$ - $\tilde{X}\ ^3\Sigma^-$ and the $\tilde{c}\ ^1\Pi - \tilde{a}\ ^1\Delta$ bands. Finally, KER spectra are presented for selected $\tilde{A}\ ^3\Pi$ - $\tilde{X}\ ^3\Sigma^-$ and $\tilde{c}\ ^1\Pi - \tilde{a}\ ^1\Delta$ transitions.

A. Photoelectron spectrum of CCO^- anion

The photoelectron spectrum of CCO^- taken at 5.822 eV (213 nm) is shown in Fig. 3. The absolute peak positions and assignments are located in Table 1. The spectrum consists of a series vibrationally-resolved bands corresponding to transitions to several neutral electronic states. We observe all of the peaks reported by Zengin *et al.*[18] except for the $\tilde{a}\ ^1\Delta$ (200) transition. In addition we see peaks labeled K, L and M that were not observed previously. Peak K is assigned as the transition to the $\tilde{A}\ ^3\Pi$ (003) state. Peaks L and M are too high in energy to correspond to a vibrational transition within the $\tilde{A}\ ^3\Pi$ manifold, so we assign L and M to the origin and the (001) vibrational level of the $\tilde{c}\ ^1\Pi$ state, respectively. Note that the $\tilde{A}\ ^3\Pi$ and $\tilde{c}\ ^1\Pi$ neutral states result from detachment of an electron from the 2π anion orbital and should therefore have the same photoelectron angular distribution. This is confirmed by photoelectron spectra taken at other laser polarization angles (not shown). From these assignments, the adiabatic electron affinity of CCO is 2.310 ± 0.012 eV and the term values for the $\tilde{a}\ ^1\Delta$ and $\tilde{c}\ ^1\Pi$ states of CCO are

0.653 ± 0.017 eV and 2.775 ± 0.017 eV, respectively. The error bars on the electron affinity and $\tilde{a}\ ^1\Delta$ term value are somewhat smaller than those reported by Zengin *et al.*[18]

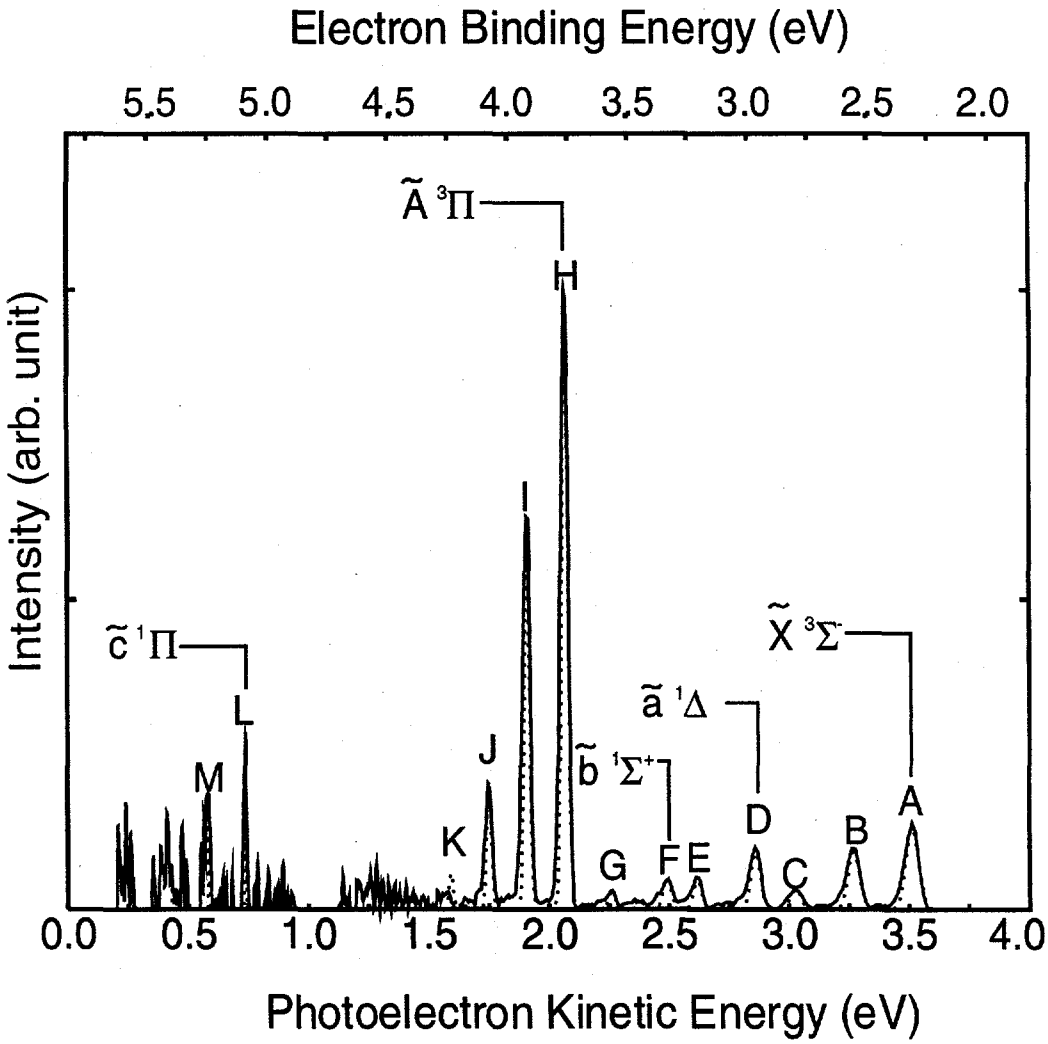

Figure 3 : Photoelectron spectrum of CCO^- at 5.822 eV taken at laser polarization $\theta = 0^0$.

Table 1. Peak position and assignments for the CCO^- photoelectron spectrum.

Peak	Assignment	Position (eV)	Splitting from origin (cm^{-1})[a]
A	$\tilde{X}\ ^3\Sigma^-$ (000)	3.512	-------
B	$\tilde{X}\ ^3\Sigma^-$ (100)	3.269	1960
C	$\tilde{X}\ ^3\Sigma^-$ (200)	3.019	3976
D	$\tilde{a}\ ^1\Delta$ (000)	2.859	5267
E	$\tilde{a}\ ^1\Delta$ (100)	2.618	7211
F	$\tilde{b}\ ^1\Sigma^+$ (000)	2.488	8259
G	$\tilde{b}\ ^1\Sigma^+$ (100)	2.262	10082
H	$\tilde{A}\ ^3\Pi$ (000)	2.066	11663
I	$\tilde{A}\ ^3\Pi$ (001)	1.909	12929
J	$\tilde{A}\ ^3\Pi$ (002)	1.748	14228
K	$\tilde{A}\ ^3\Pi$ (003)	1.577	15607
L	$\tilde{c}\ ^1\Pi$ (000)	0.737	22382
M	$\tilde{c}\ ^1\Pi$ (001)	0.584	23616

[a] All peak positions have an uncertainty of 12 meV.

B. Photofragment yield spectrum

With the aid of photoelectron spectrum by Sec. IIIA, we can selectively form CCO in the ground $\tilde{X}\ ^3\Sigma^-$ state, or in a combination $\tilde{X}\ ^3\Sigma^-$ and $\tilde{a}\ ^1\Delta$ states. To form neutral CCO in its ground $\tilde{X}\ ^3\Sigma^-$ state with no vibrational excitation, we detach at 18,690 cm^{-1}, just above the photodetachment threshold (18,630 cm^{-1}). We can then measure the PFY spectrum from CCO $\tilde{X}\ ^3\Sigma^-$ radicals.

To form neutral CCO in its $\tilde{a}\ ^1\Delta$ electronic state with zero quanta of vibrational excitation, we detach at 24,210 cm^{-1}, just above the photodetachment threshold for this state (23,900 cm^{-1}). At this energy, one also produces CCO in its $\tilde{X}\ ^3\Sigma^-$ state with the vibrational distribution shown in the photoelectron spectrum (Fig. 3). To identify dissociation signal from the $\tilde{a}\ ^1\Delta$ state, PFY spectra are repeated at a detachment energy

23,070 cm^{-1}, just below the $\tilde{a}\ ^1\Delta$ detachment threshold. The difference between PFY spectra obtained at 24,210 cm^{-1} and 23,070 cm^{-1} is from CCO $\tilde{a}\ ^1\Delta$ radicals.

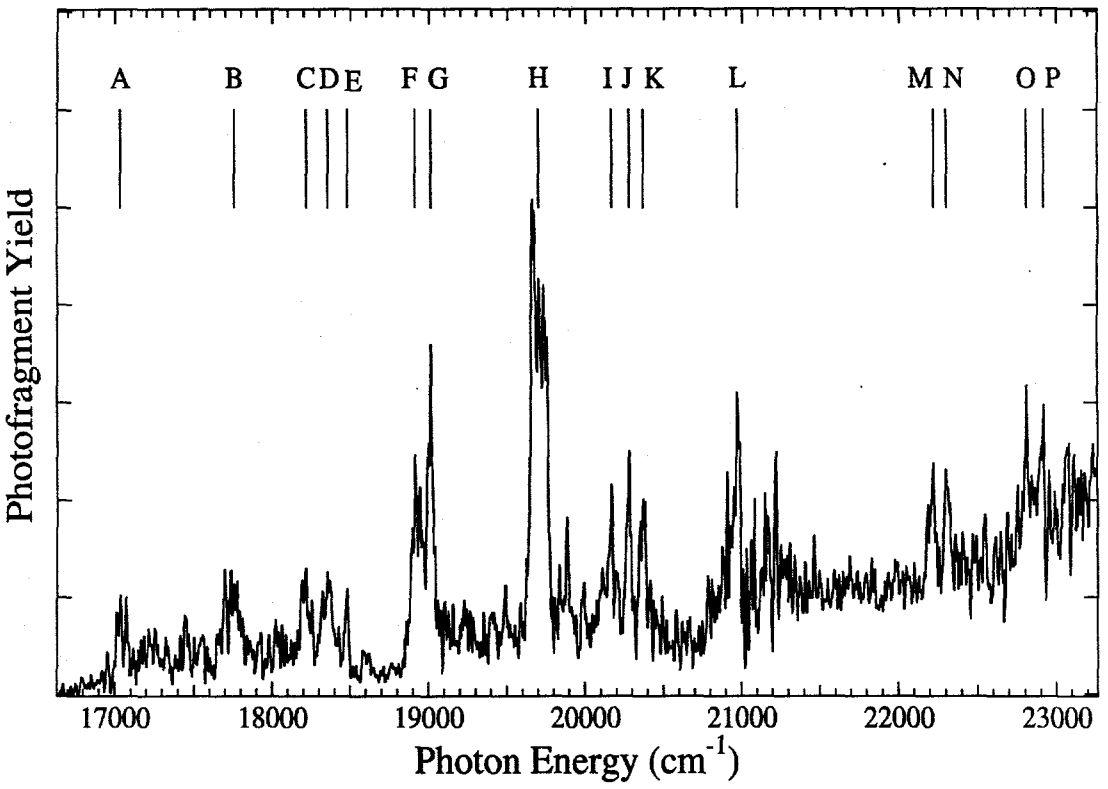

Figure 4 : Photofragment Yield (PFY) spectrum of CCO for the $\tilde{A}\ ^3\Pi$ - $\tilde{X}\ ^3\Sigma^-$ band. Assignments of labeled peaks are given in Table 3.

The PFY spectrum obtained from CCO ($\tilde{X}\ ^3\Sigma^-$) is shown Fig. 4. This spectrum covers 16,660 cm^{-1} to 23,529 cm^{-1} with 5.5 – 2.8 cm^{-1} (0.1 nm) steps. Although the signal is weak, several sharp features are observed that are assigned to transitions to excited vibrational levels of the $\tilde{A}\ ^3\Pi$ state (see Sec. IVA) that lie above the bond dissociation energy. The signal is weak because of poor Franck-Condon factors combined with low translational energy release (see Sec. IVB); the latter effect reduces our photofragment collection efficiency. Note that no dissociation is observed until well

above the $\tilde{A}\ ^3\Pi$ - $\tilde{X}\ ^3\Sigma^-$ origin at 11,651 cm^{-1},[9] because the lower vibrational levels are bound. Also, we do observe dissociation around 500 nm (19,994 cm^{-1}), a result consistent with the interpretation of the matrix experiments put forth by Jacox *et al.*[8]

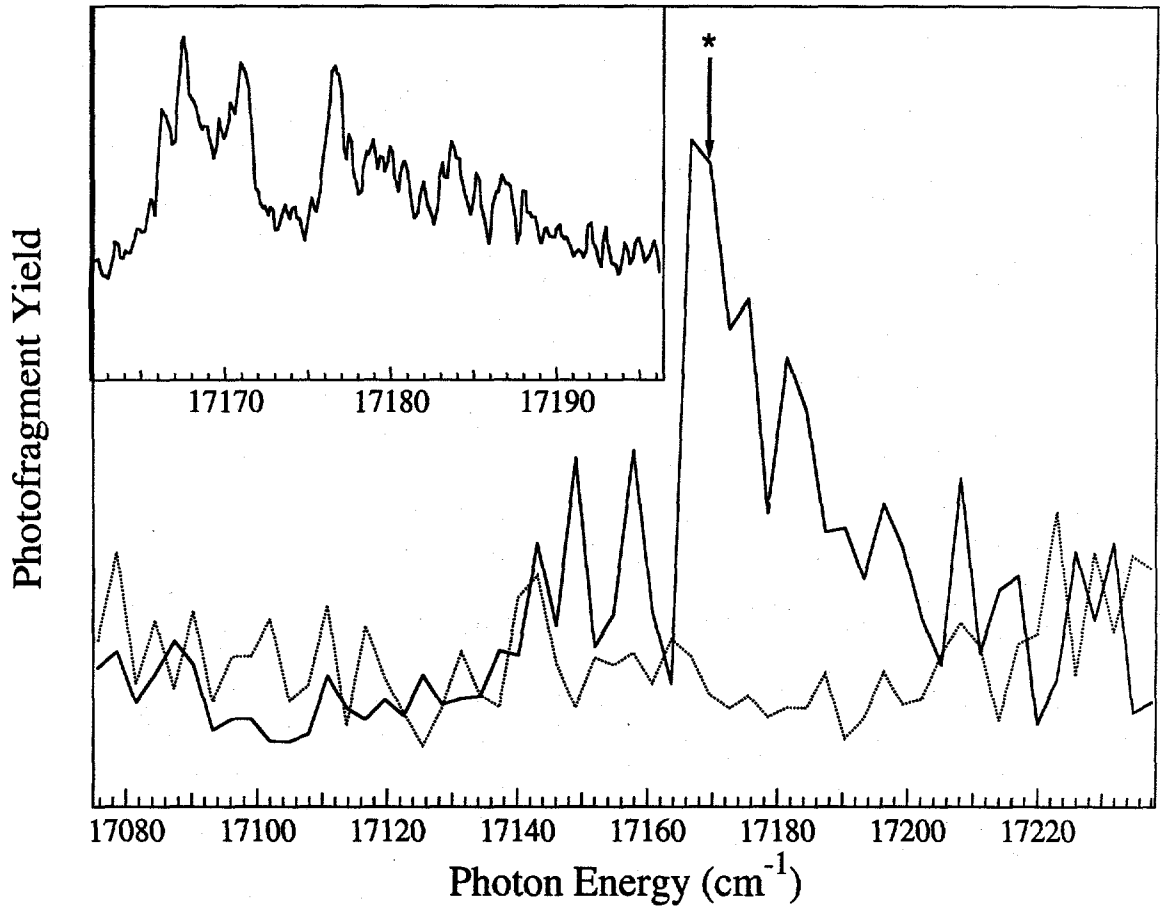

Figure 5 : Photofragment Yield (PFY) spectrum of CCO for $\tilde{c}\ ^1\Pi$ - $\tilde{a}\ ^1\Delta$ origin. Solid line: ν_{Detach} = 24,210 cm^{-1} (above the $\tilde{a}\ ^1\Delta$ threshold). Dotted line: ν_{Detach} = 23,070 cm^{-1} (below the $\tilde{a}\ ^1\Delta$ threshold. Inset shows finer scan (0.005 nm step) of the $\tilde{c}\ ^1\Pi$ - $\tilde{a}\ ^1\Delta$ origin.

The PFY spectrum obtained from CCO ($\tilde{a}\ ^1\Delta$) is shown Fig. 5. Based on the photoelectron spectrum in Fig. 3, the origin of the $\tilde{c}\ ^1\Pi$ – $\tilde{a}\ ^1\Delta$ band should occur at 17,115 ± 140 cm^{-1}. The main part of Fig. 5 shows spectra taken from 17,080-17,220 cm^{-1} at 0.1 nm(~3 cm^{-1}) resolution. The dotted line shows data using ν_{detach} = 23,070 cm^{-1} and

the solid line shows data using ν_{detach} = 24,210 cm^{-1}. The large peak seen at 17,170 cm^{-1} in the spectrum taken at the higher detachment energy is assigned to the $\tilde{c}\ ^1\Pi - \tilde{a}\ ^1\Delta$ origin. The inset in Fig. 5 shows a finer scan with 0.005 nm (~0.15 cm^{-1}) step and shows partially resolved rotational structure. No further structure is resolved using an etalon, with which the resolution of the laser is 0.04 cm^{-1}. Based on our term value for the $\tilde{a}\ ^1\Delta$ state, 0.653 ± 0.017 eV, the term value for the $\tilde{c}\ ^1\Pi$ state is 2.782 ± 0.017 eV.

C. Translational energy distribution of photofragments

Translational energy distributions $P(E_T)$ were obtained at selected peaks in the $\tilde{A}\ ^3\Pi$ - $\tilde{X}\ ^3\Sigma^-$ and $\tilde{c}\ ^1\Pi - \tilde{a}\ ^1\Delta$ absorption bands. Fig. 6 shows the $P(E_T)$ distribution obtained at 19,660 cm^{-1} (2.44 eV), the strongest peak in the $\tilde{A}\ ^3\Pi$ - $\tilde{X}\ ^3\Sigma^-$ band. The distribution is binned in steps of 10 meV. The photofragment mass spectrum in the inset of Fig. 6 shows peaks at mass 12 and 28, corresponding to C+CO. The $P(E_T)$ distribution consists of a sharp peak centered around 0.15 eV with an abrupt drop in intensity toward higher translational energy. The maximum kinetic energy at which signal is seen is 0.20 ± 0.02 eV.

Figure 7 shows the $P(E_T)$ distribution obtained from excitation of the $\tilde{c}\ ^1\Pi - \tilde{a}\ ^1\Delta$ band at 17,170 cm^{-1}, marked with a * in Fig.5. The same photofragment mass spectrum is seen as in Fig. 6. This $P(E_T)$ distribution consists of two peaks centered at 0.5 and 0.23 eV, corresponding to C + CO (υ=0,1). The higher energy peak drops off abruptly at a maximum kinetic energy of 0.54 ± 0.02 eV.

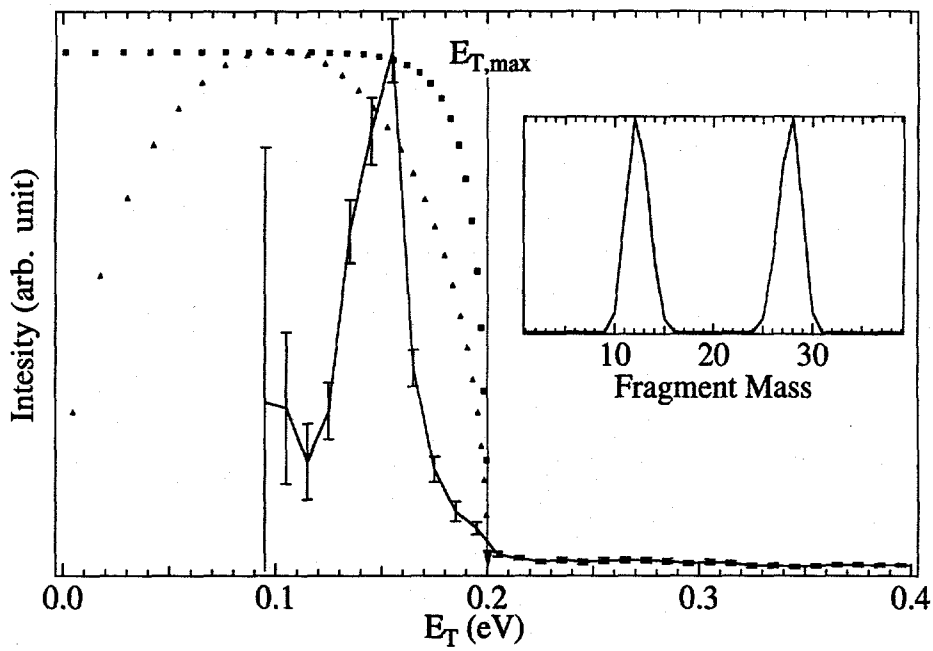

Figure 6 : Translational energy distribution $P(E_T)$ of C + CO products from excitation of 1_0^4 $\tilde{A}\ ^3\Pi$ - $\tilde{X}\ ^3\Sigma^-$ transition ($h\nu_{dissociate} = 2.44$ eV). Inset shows the photofragment mass spectrum of CCO. Solid line: experimental data. The $P(E_T)$ distributions calculated from the prior distribution and phase space theory are shown as ▲ and ■, respectively.

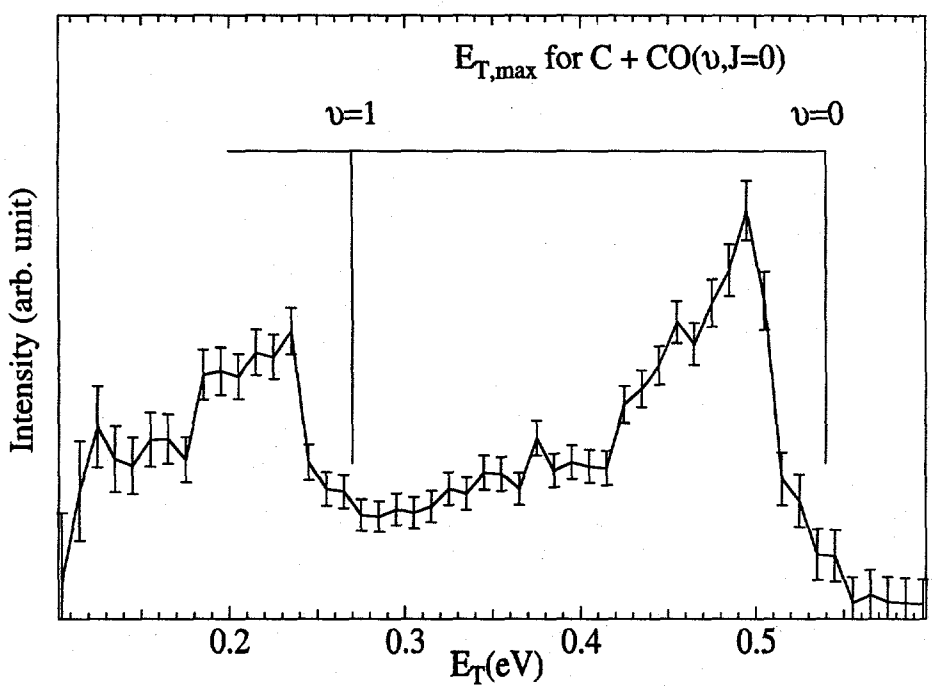

Figure 7 : Kinetic Energy Release (KER) spectrum of CCO at the $\tilde{c}\ ^1\Pi$ - $\tilde{a}\ ^1\Delta$ origin transition ($h\nu_{Diss}$ = 2.13 eV).

D. *Ab initio* calculations

Ab initio calculations were performed to better understand how the various electronic states of CCO are coupled to the dissociation continuum. The lowest energy dissociation channel, $C(^3P) + CO(^1\Sigma^+)$, correlates with the $\tilde{X}\ ^3\Sigma^-$ state and a $^3\Pi$ state. The molecular orbital configuration for this $^3\Pi$ state (hereafter referred to as the $\tilde{U}\ ^3\Pi$ state) is $....(6\sigma)^2\ (1\pi)^4\ (7\sigma)^2\ (2\pi)^1\ (8\sigma)^1$. This is therefore not the $\tilde{A}\ ^3\Pi$ state, for which the molecular orbital configuration is $....(6\sigma)^2\ (1\pi)^4\ (7\sigma)^1\ (2\pi)^3$; the $\tilde{A}\ ^3\Pi$ state asymptotically correlates with excited state triplet products, $C(^3P) + CO(^3\Pi)$. The 8σ orbital is C-C antibonding, suggesting that the $\tilde{U}\ ^3\Pi$ state is repulsive. These qualitative considerations imply that a diabatic crossing occurs between the $\tilde{A}\ ^3\Pi$ state and a repulsive $^3\Pi$ state, as shown in Fig. 8. The object of our *ab initio* calculations was to determine the effect of this crossing on the dissociation dynamics.

Calculations were performed using the CASSCF(8,8) method with a 6-31G* basis within the Gaussian 92 suite of programs.[39] The active space consists of six Π orbitals (1Π, 2Π, 3Π) and two σ orbitals (7σ, 8σ). R_{CO} is optimized at each R_{CC} and the linear configuration is determined to be the minimum energy configuration for all values of R_{CC}. The calculation predicts the crossing between the $\tilde{A}\ ^3\Pi$ state and a repulsive $^3\Pi$ state to occur at R_{CC} = 1.774 Å and R_{CO} = 1.142 Å, which is 5.5 eV above the $\tilde{X}\ ^3\Sigma^-$ minimum for which R_{CC}=1.388 Å and R_{CO}=1.149 Å.

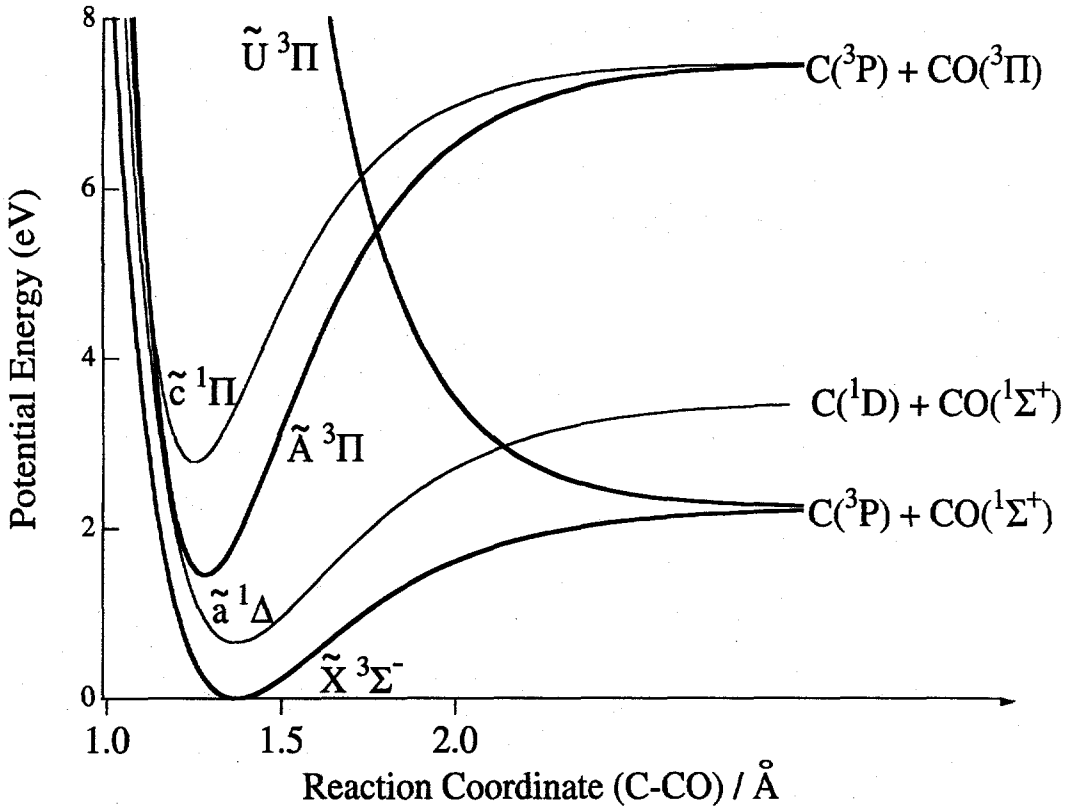

Figure 8 : Schematic potential energy curves for the ground and excited states of CCO radical, illustrating correlations with the ground and excited state C + CO products. The energy spacings from the ground state to excited states of CCO and the C-CO bond dissociation energy are determined by our present work. Minimum energy configurations are obtained from Ref. 18 and the crossing point between the $\tilde{A}\ ^3\Pi$ and the $\tilde{U}\ ^3\Pi$ is obtained from the *ab initio* calculation described in the text.

At this level of calculation, the term value for the $\tilde{A}\ ^3\Pi$ state is 1.617eV, while the experimental value is 1.445eV.[12] Also, the calculated sum of R_{CC} and R_{CO} is 2.54 Å for the $\tilde{X}\ ^3\Sigma^-$ state and 2.45 Å for the $\tilde{A}\ ^3\Pi$ state, both of which lie close to the experimental values of 2.52 Å and 2.45 Å, respectively.[9]

The diabatic crossing occurs well above the onset of dissociation in the PFY spectrum (~2.4 eV). The energy of this crossing may be too high because of the limited accuracy of the calculation. Moreover, the two *adiabatic* curves repel each other in the

crossing region, so that the effective barrier to dissociation of the $\tilde{A}\,^3\Pi$ along the lower adiabatic will be somewhat less than the energy of the diabatic crossing point. Nonetheless, the calculations certainly suggest that dissociation of the $\tilde{A}\,^3\Pi$ in the energy range probed by our experiment does not occur by coupling to the repulsive $\tilde{U}\,^3\Pi$ state. The dissociation mechanism is discussed further in Section V.

IV. Analysis

In this section, we analyze the resonances in the photofragment yield spectrum for the $\tilde{A}\,^3\Pi$ - $\tilde{X}\,^3\Sigma^-$ band of CCO and discuss the energetics of CCO radical dissociation.

A. Photofragment yield spectrum

Previous LIF and absorption studies of the CCO $\tilde{A}\,^3\Pi$ - $\tilde{X}\,^3\Sigma^-$ transition[9,10,12,15,16] have yielded an accurate set of spectroscopic constants for the lower vibrational levels of the $\tilde{A}\,^3\Pi$ state, including vibrational frequencies for the ν_1 (C-O stretch), ν_2 (CCO bend), and ν_3 (C-C stretch) modes, anharmonicities for the ν_1 and ν_2 modes, rotational constants, spin-orbit coupling and Renner-Teller parameters. These are listed in Table 2. The energy level pattern due to Renner-Teller coupling in a $^3\Pi$ electronic state is given by Hougen.[40] We can use these constants to predict the location of the higher-lying vibrational levels, and thus assign most of the features seen in the PFY spectrum in Fig. 4. The predicted energies and assignments of the PFY resonances are listed in Table 3.

Peak H, the most prominent peak, centered at 19,698 cm^{-1}, is assigned to the 1_0^4 transition. This peak is actually a triplet split by 35 cm^{-1} corresponding to the three spin-orbit components of the $\tilde{A}\,^3\Pi$ state. This splitting agrees well with that seen for several of the lower-lying levels.[9,12,15,16] Transitions involving the other two modes also contribute to the PFY spectrum. Although this is a linear-to-linear transition, the bending mode is active due to the large difference of bending frequency in the $\tilde{X}$ (379.53 cm^{-1})[14] and $\tilde{A}$ (594.75 cm^{-1})[15] states and strong Renner-Teller coupling in the $\tilde{A}$ state.[15,16] Some of the assignments are ambiguous, especially those involving the bending mode. These problems arise in part because of a 2:1 Fermi resonance between the ν_2 and ν_3 modes (see Table 2) as noted in previous studies. [9,10,16] Nonetheless the agreement between the experimental and predicted energies is generally reasonable, supporting the assignments in Table 3.

Table 2 : Fitting Parameters for calculating position of absorption ($\tilde{A}\,^3\Pi$ - $\tilde{X}\,^3\Sigma^-$ of CCO). (Unit : cm^{-1})

		$\tilde{A}\,^3\Pi$ (cm^{-1})
T_o		11,651.2[12]
ω_1		2068.6[9]
$\omega_1\chi_1$		11.45
ω_2		601.25[15,16]
$\omega_2\chi_2$		3.25
ω_3		1284[16]
$\omega_3\chi_3$		0.0
	$n_2 = 2$	$n_2 = 1$
A_{SO}	-35.614[16]	-35.1667[15]
$\varepsilon\omega_2$	104[16]	104.5[15]

Table 3: Peak assignment (cm^{-1}) for PFY spectrum of CCO. Numbers in brackets are calculated values in cm^{-1} based on parameters in Table 2.

	Experimental peak position (cm^{-1})	Calculated position (cm^{-1})	Assignment/$E(n_2,K,P)$[a]
A	17 035	17 046	$1_0^2 2_0^2$/$E^+(2,1,0)$
B	17 756	17 720	1_0^3
C	18 216	18 288	$1_0^2 3_0^2$
D	18 353	18 330	$1_0^2 2_0^2 3_0^1$ / $E^+(2,10)$
E	18 479	18 414	$1_0^3 2_0^1$ / $E^+(1,0,0)$
F	18 911	18 982	$1_0^2 2_0^1 3_0^2$ / $E^+(1,0,0)$
G	19 012	19 004	$1_0^3 3_0^1$
		19 046	$1_0^3 2_0^2$ / $E^+(2,1,0)$
H	19 698	19 697	1_0^4
I	20 166	20 288	$1_0^3 3_0^2$
J	20 277	20 330	$1_0^3 2_0^2 3_0^1$ / $E^+(2,1,0)$
K	20 367	20 391	$1_0^4 2_0^1$ / $E^+(1,0,0)$
L	20 970	20 981	$1_0^4 3_0^1$
		21 023	$1_0^4 2_0^2$ / $E^+(2,1,0)$
M	22 219	22 265	$1_0^4 3_0^2$
N	22 298	22 307	$1_0^4 2_0^2 3_0^1$ / $E^+(2,1,0)$

[a] Energies $E(n_2,K,P)$ of various vibronic states are characterized by a set of quantum numbers, n_2, K(the resultant vibronic angular momentum = $|\pm\Lambda\pm l|$), and P(the resultant vibronic angular momentum including spin = $|\pm\Omega\pm l|$). The upper Renner -Teller state is expressed by E^+, and the lower by E^-, which is not observed in our present work.

B. Translational energy distributions

1. CCO thermochemistry

The $P(E_T)$ distributions in Figures 6 and 7 yield information on the CCO dissociation energy and the partitioning of excess energy among the product degrees of freedom. Energy conservation dictates that

$$h\nu_{diss} + E_{INT}(CCO) = D_0(C—CO) + E_{INT}(C + CO) + E_T(C + CO), \quad (2)$$

where $E_{INT}(CCO)$ is the initial energy of the CCO, $E_{INT}(C + CO)$ is the product internal energy, and $E_T(C + CO)$ is the product translational energy. At the maximum allowed kinetic energy, E_{Tmax}, $E_{INT}(C + CO)=0$. The bond dissociation energy can therefore be determined from the $P(E_T)$ distribution provided that the value of E_{Tmax} is clear.

The $P(E_T)$ spectrum for the $\tilde{A}\ ^3\Pi$ - $\tilde{X}\ ^3\Sigma^-$ transition shown in Fig. 6 is obtained at $h\nu_{diss}$ = 19,660 cm^{-1} (2.44 eV). The spectrum drops off abruptly on the high energy side of the peak maximum at 0.15 eV; no signal is seen beyond E_T=0.20± 0.02 eV, and this is taken to be E_{Tmax}. Although no rotational structure is resolved in the PFY spectrum of CCO, we estimate a rotational temperature of 35 K from our previous study of HCCO photodissociation,[41] so $\langle E_{INT}(CCO)\rangle \approx 0.002$ eV. Thus the bond dissociation energy for C—CO is determined: D_0(C—CO) = 2.24 ± 0.02 eV (51.7 ± 0.5 kcal/mol) at 0 K.

The $P(E_T)$ distribution in Fig. 7 is obtained from excitation of the $\tilde{c}\ ^1\Pi - \tilde{a}\ ^1\Delta$ vibrational band origin at $h\nu_{diss}$ = 2.128 eV (17,170 cm^{-1}). The abrupt drop-off in the higher energy peak yields E_{Tmax}= 0.54 ± 0.02 eV. For this band, $E_{INT}(CCO)$ includes the term energy for the $\tilde{a}\ ^1\Delta$ state, 0.653 ± 0.017 eV. We then obtain a bond dissociation energy for C—CO, D_0(C—CO) = 2.24 ± 0.03 eV (51.7 ± 0.7 kcal/mol) at 0 K. This

value is in excellent agreement with that obtained from Fig. 6, supporting our selection of E_{Tmax} in both cases. The uncertainty in D_0(C—CO) is slightly higher when derived from the data in Fig. 7 because of the uncertainty in the electronic term value of the $\tilde{a}\ ^1\Delta$ state.

Based on our value of D(C-CO), no dissociation signal should be observed at excitation energies below 18,065 cm^{-1}. However, peaks A and B in the PFY spectrum, Fig. 4, lie below this energy. While these could be hot band transitions, Table 3 shows that they can be assigned to transitions originating from the (000) level of the $\tilde{X}\ ^3\Sigma^-$ state. It is possible that they arise from resonant two-photon excitation via the intermediate $\tilde{A}\ ^3\Pi$ levels listed in Table 3. Unfortunately the dissociation signal at these energies was too low to permit measurement of the translational energy distributions.

The heat of formation of CCO is determined from the bond dissociation energy and heats of formation of C ($\Delta H^0_{f,0}$(C) = 7.371 ± 0.005 eV) and CO ($\Delta H^0_{f,0}$(CO) = -1.180 ± 0.002 eV)[21]. This yields $\Delta H^0_{f,0}$ (CCO) = 3.95 ± 0.02 eV (91.1 ± 0.5 kcal/mol). These values can be scaled to values at standard temperature (298.15 K). Using known vibrational frequencies of the CCO $\tilde{X}\ ^3\Sigma^-$ state,[10,13,14] we obtain $\Delta H^0_{f,298}$ (CCO) = 4.04 ± 0.02 eV. This value agrees with the recent determination from the CCO^- photoelectron spectrum, $\Delta H^0_{f,298}$ (CCO) = 3.99 ± 0.20 eV,[18] but our error bars are considerably lower.

The heat of formation of CCO^- can be determined from this heat of formation, the electron affinity of CCO and the integrated heat capacity of electron: $\Delta H^0_{f,\,298}$ (CCO^-) = 1.67 ± 0.02 eV. The gas phase acidity of HCCO can be also calculated from the heats of formation of H^+,[21] CCO^- and HCCO,[41] as follows.

$$\Delta H^0_{acid,\,298}\,(HCCO) = \Delta H^0_{f,\,298}\,(H^+) + \Delta H^0_{f,\,298}\,(CCO^-) - \Delta H^0_{f,\,298}\,(HCCO)$$

$$= 15.76 \pm 0.04 \text{ eV}. \qquad (3)$$

The enthalpy for acid association of HCCO was determined by Van Doren *et al*: 15.45 (±0.12) eV < $\Delta H^0_{acid,\,298K}$ (HCCO) < 15.87 (±0.12) eV. [23] This is in good agreement with our value.

2. Product energy distributions

From the bond dissociation energy determined above, the single peak seen in the $P(E_T)$ spectrum in Fig. 6 corresponds entirely to C+CO(v=0); C+CO(v=1) products are not energetically accessible. The width of the peak in this spectrum therefore indicates the extent of rotational excitation in the CO fragment. We find that f_R=0.25, where f_R is the fraction of available energy appearing as product rotation. In Fig. 7, however, E_{INT}(CCO) is sufficiently large so that the C + CO(v=1) state is energetically accessible. This is the origin of the lower energy peak centered at 0.23 eV. Roughly 40% of the CO product is in the v=1 state. We also observe broad features to the low energy side of each peak, which correspond to the rotational excitation of CO product. The overall partitioning of available energy among product translation, vibration, and rotation is f_T=0.6, f_v=0.2, and f_R=0.2, respectively.

It is useful to compare the experimental distributions with those obtained from simple statistical models. Shown in Fig. 6 along with the experimental data are the translational energy distributions expected for a prior distribution (▲)[42] and from phase space theory (■).[43-45] The prior and PST distributions are calculated using Eqns. (4) and (5) respectively:

$$P(E_T) = \sum_{J_{CO}} (2J_{CO}+1)(E_T)^{1/2} \cdot \delta(h\nu - D_0 - E_t - B \cdot J_{CO}(J_{CO}+1)) \quad (4)$$

$$P(E_T) = \sum_{J_{CCO}} \sum_{J_{CO}} P_{Bolt}(J_{CCO}) \cdot (2J'+1) \cdot \delta(h\nu - D_0 - E_T - B \cdot J_{CO}(J_{CO}+1)) \quad (5)$$

where J_{CO} and J_{CCO} are the angular momenta of CO and CCO, B is the rotational constant of CO fragment, and $P_{Bolt}(J_{CCO})$ is the Boltzmann distribution assuming T_{rot}= 35K. In Eqn. (5), J' = J_{CCO} when $J_{CO} \geq J_{CCO}$ and J'=J_{CO} when $J_{CO} < J_{CCO}$. Both statistical models predict a considerably broader rotational distribution with more rotational excitation of the CO than is observed experimentally.

We have also calculated the prior distribution expected for the singlet-singlet transition in Fig. 7. This predicts 26% of the CO product to be in v=1, with the overall energy partitioning given by f_T=0.52, f_V=0.13, and f_R=0.35. The experimental distribution shows more CO vibrational excitation and less rotational excitation. It therefore appears that neither of the experimental $P(E_T)$ distributions can be reproduced by statistical models. This is discussed further in the next section.

V. Discussion

In this section we consider the dissociation mechanism subsequent to excitation of the $\tilde{A}\,^3\Pi$ and $\tilde{c}\,^1\Pi$ states. The PFY spectra in Figs. 4 and 5 are structured, indicating that excitation in each case is to a bound state that undergoes predissociation. As discussed in Section IIID and displayed in Fig. 8, the $\tilde{A}\,^3\Pi$ state correlates diabatically to excited $C(^3P)$ + $CO(^3\Pi)$ products that lie well above the excitation energies in this study.

In order to undergo dissociation to $C(^3P) + CO(^1\Sigma^+)$ products, the $\tilde{A}\,^3\Pi$ state must decay either by coupling to the repulsive $\tilde{U}\,^3\Pi$ state, or by internal conversion to the ground $\tilde{X}\,^3\Sigma^-$ state.

The PFY spectrum and $P(E_T)$ distribution in Fig. 6 shows that the onset for dissociation from the $\tilde{A}\,^3\Pi$ state occurs at or just above the C-CO bond dissociation energy. Given the high energy of the crossing point between the $\tilde{U}\,^3\Pi$ and $\tilde{A}\,^3\Pi$ states, it is unlikely that predissociation via the repulsive $\tilde{U}\,^3\Pi$ state would occur so close to the thermodynamic threshold for dissociation. On the other hand, if there were no barrier along the reaction coordinate for dissociation of the $\tilde{X}\,^3\Sigma^-$ state, internal conversion to this state would lead to dissociation as soon as the bond dissociation energy is exceeded. This therefore appears to be the dissociation mechanism for the $\tilde{A}\,^3\Pi$ state.

In Fig. 6, both statistical distributions result in considerably more CO rotational excitation than is seen experimentally, indicating that dissociation on the ground state following internal conversion is non-statistical in nature. This is qualitatively consistent with the relatively shallow well and small number of vibrational modes, both of which might be expected to lead to very rapid dissociation. More quantitatively, one does not expect statistical dissociation unless the RRKM dissociation rate is considerably less than the characteristic vibrational frequencies; this condition allows IVR to occur prior to dissociation.[46]

The RRKM dissociation rate is given by

$$k_{RRKM}(E) = \frac{G(E - D_0)}{hN(E)}, \qquad (6)$$

where $G(E-D_0)$ is the sum of states for the active degrees of freedom in the transition state and $N(E)$ is the reactant density of states. The ground state of CCO ($\tilde{X}\ ^3\Sigma^-$ state) can correlate with the lowest dissociation channel ($C(^3P) + CO(^1\Sigma^+)$) without orbital change, so no barrier on $\tilde{X}\ ^3\Sigma^-$ state of CCO is expected. We thus take the transition state to correspond to C+CO products. The RRKM dissociation rate is then calculated by using the four vibrational degrees of freedom of CCO ($\tilde{X}\ ^3\Sigma^-$ state) for the reactant and the two rotational and one vibrational degrees of freedom of CO fragment for the transition state. We find $k_{RRKM}(E) = 5.04*10^{12}\ s^{-1}$, which is higher than the bend frequency on the ground state, $2.51*10^{12}\ s^{-1}$. Under these circumstances it is not surprising that a non-statistical product energy distribution is observed.

We next consider dissociation of the $\tilde{c}\ ^1\Pi$ state. Only the $C(^3P) + CO(^1\Sigma^+)$ channel is energetically accessible, so intersystem crossing to a triplet state must occur prior to dissociation. As was the case with the $\tilde{A}\ ^3\Pi$ state, the crossing point with the $\tilde{U}\ ^3\Pi$ state is most likely too high in energy for dissociation by this state to be a viable mechanism, and it is more reasonable to expect dissociation to occur by intersystem crossing to the $\tilde{X}\ ^3\Sigma^-$ state. This may occur directly, or through one or both of the electronic states that lie between the $\tilde{c}\ ^1\Pi$ and $\tilde{X}\ ^3\Sigma^-$ states. Since the internal energy on the ground state resulting from this process is considerably higher than for the $\tilde{A}\ ^3\Pi$ state level responsible for the translational energy distribution in Fig. 6, one again expects a non-statistical product energy distribution. This is consistent with the experimental distribution in Fig. 7, which, as discussed in Section IVB2, has considerably less energy

in CO rotation and more energy in CO vibration than would be expected from a statistical model.

We have previously found that the dissociation yield from the vibrationless level of an excited electronic state is less than unity even if this level is well above the dissociation threshold. [41,47] This suggests that it may be possible to observe the vibrational origin of the $\tilde{c}\ ^1\Pi$ - $\tilde{a}\ ^1\Delta$ band by laser-induced fluorescence. Such an observation would be extremely useful as a probe of singlet CCO.

VI. Conclusions

This paper reports the first study of the photodissociation spectroscopy and dynamics of the CCO radical. Photofragment yield (PFY) spectra and photofragment kinetic energy distributions are obtained using our fast radical beam photofragment translation spectroscopy instrument. We observe predissociation from excited vibrational levels of the $\tilde{A}\ ^3\Pi$ state that are accessed by excitation of the $\tilde{A}\ ^3\Pi$ - $\tilde{X}\ ^3\Sigma^-$ band, and from the ground vibrational level of the $\tilde{c}\ ^1\Pi$ state via excitation of the $\tilde{c}\ ^1\Pi$ - $\tilde{a}\ ^1\Delta$ band. In both cases, the lower state of CCO is generated by laser photodetachment of CCO^-. The $\tilde{X}\ ^3\Sigma^-$ state is formed using a detachment energy just above the electron affinity of CCO, while the $\tilde{a}\ ^1\Delta$ state is formed at a detachment energy sufficiently high to access this low-lying excited state of CCO. The location of the $\tilde{c}\ ^1\Pi$ was unknown prior to this work. We located it approximately by photoelectron spectroscopy of CCO^- at a photodetachment energy of 5.82 eV, obtaining a term value of 2.775±0.020 eV for the

$\tilde{c}\ ^1\Pi$ state. This enabled us to find the $\tilde{c}\ ^1\Pi$ - $\tilde{a}\ ^1\Delta$ band origin at 17,170 cm^{-1} (2.128 eV) using photodissociation spectroscopy.

The PFY spectrum for the $\tilde{A}\ ^3\Pi$ - $\tilde{X}\ ^3\Sigma^-$ band consists of a series of transitions to vibrationally excited levels of the $\tilde{A}\ ^3\Pi$ state that lie above the dissociation threshold. These transitions, reported here for the first time, can be assigned based on spectroscopic constants from earlier absorption and laser-induced fluorescence studies of CCO. Our observation of the $\tilde{c}\ ^1\Pi$ - $\tilde{a}\ ^1\Delta$ band origin represents the first observation of a transition between singlet states of CCO, and may be useful as a diagnostic for singlet CCO in combustion and other applications.

Product kinetic energy distributions from excitation of the triplet and singlet bands yield the CCO bond dissociation energy and the partitioning of available energy among the product degrees of freedom. The bond dissociation energy is 2.24 ± 0.02 eV, yielding $\Delta H^0_{f,298}$(CCO)=4.04 ± 0.02 eV. The kinetic energy distribution for the 1^4_0 transition of the triplet band shows that all the CO is in its v=0 level (the only energetically accessible level), while a mixture of CO v=0 and v=1 level results from the origin transition of the $\tilde{c}\ ^1\Pi$ - $\tilde{a}\ ^1\Delta$ band. In both cases, the distributions are highly non-statistical. Nonetheless, comparison with *ab initio* calculations implies that the $\tilde{A}\ ^3\Pi$ and $\tilde{c}\ ^1\Pi$ states dissociate via internal conversion and intersystem crossing, respectively, to the ground $\tilde{X}\ ^3\Sigma^-$ state.

ACKNOWLEDGEMENTS

This research is supported by the Director, Office of Energy Research, Office of Basic Energy Sciences, Chemical Sciences Division, of the U. S. Department of Energy under Contract No. DE-AC03-76SF00098. We thank Professor Robert E. Continetti for sharing his results prior to publication.

References

[1] R. D. Brown, D. M. Cragg, P. D. Godfrey, W. M. Irvine, D. McGonagle, and M. Ohishi, Origins of Life and Evolution of the Biosphere **21,** 399 (1992).

[2] W. M. Irvine, Adv. Space Res. **15,** 35 (1995).

[3] M. Ohishi, H. Suzuki, S. I. Ishikawa, C. Yamada, H. Kanamori, W. M. Irvine, R. D. Brown, P. D. Godfrey, and N. Kaifu, Astrophys. J. **380,** L39 (1991).

[4] K. H. Becker and K. D. Bayes, J. Chem. Phys. **48,** 653 (1968).

[5] K. D. Bayes, J. Chem. Phys. **52,** 1093 (1970).

[6] A. Fontijn and S. E. Johnson, J. Chem. Phys. **59,** 6193 (1973).

[7] G. Geoffroy and S. L. Bassner, Adv. Organomet. Chem. **28,** 1 (1988).

[8] M. E. Jacox, D. E. Milligan, N. G. Moll, and W. E. Thompson, J. Chem. Phys. **43,** 3734 (1965).

[9] C. Devillers and D. A. Ramsay, Can. J. Phys. **49,** 2839 (1971).

[10] W. M. Pitts, V. M. Donnelley, A. P. Baronavski, and J. R. McDonald, Chem. Phys. **61,** 451 (1981).

[11] Y. Ohshima, Y. Endo, and T. Ogata, J. Chem. Phys. **102,** 1493 (1995).

[12] M. Fujitake, R. Kiryu, and N. Ohashi, J. Mol. Spectrosc. **154,** 169 (1992).

[13] C. Yamada, H. Kanamori, H. Horiguchi, S. Tsuchiya, and E. Hirota, J. Chem. Phys. **84,** 2573 (1986).

[14] N. Ohashi, R. Kiryu, S. Okino, and M. Fujitake, J. Mol. Spectrosc. **157,** 50 (1993).

[15] H. Abe, T. Kikuchi, K. Takahashi, M. Fujitake, and N. Ohashi, J. Mol. Spectrosc. **167,** 353 (1994).

[16] H. Abe, Y. Kawamoto, M. Fujitake, N. Ohashi, T. Momose, and T. Shida, J. Mol. Spectrosc. **180,** 277 (1996).

[17] J. M. Oakes, M. E. Jones, V. M. Bieberbaum, and G. B. Ellison, J. Phys. Chem. **87,** 4810 (1983).

[18] V. Zengin, B. J. Persson, K. M. Strong, and R. E. Continetti, J. Chem. Phys. **105,** 9740 (1996).

[19] S. P. Walch, J. Chem. Phys. **72,** 5679 (1980).

[20] C. F. Chabalowski, R. J. Buenker, and S. D. Peyerimhoff, J. Chem. Phys. **84,** 268 (1986).

[21] M. W. Chase Jr., C. A. Davies, J. R. Downey Jr., D. J. Fruip, R. A. McDonald, and A. N. Syverud, *JANAF Thermochemical Tables, 3rd Ed., J. Chem. Phys. Ref. Data* ***14****, Suppl. No. 1.* (1985).

[22] H. B. Palmer and W. D. Cross, Carbon **3,** 475 (1966).

[23] J. M. Van Doren, T. M. Miller, A. E. S. Miller, A. A. Viggiano, R. A. Morris, and J. F. Paulson, J. Am. Chem. Soc. **115,** 7407 (1993).

[24] D. G. Williamson and K. D. Bayes, J. Am. Chem. Soc. **90,** 1957 (1968).

[25] K. D. Bayes, J. Am. Chem. Soc. **84,** 4077 (1962).

[26] K. D. Bayes, J. Am. Chem. Soc. **85,** 1730 (1963).

[27] T. Morrow and W. D. McGrath, Trans. Faraday Soc. **62,** 3142 (1966).

[28] W. Bauer, R. Meuser, and K. H. Becker, Journal of Photochemistry **24,** 99 (1984).

[29] K. H. Becker, R. Konig, R. Meuser, P. Wiesen, and K. D. Bayes, J. Photochem. and Photobiology, A : Chem. **64,** 1 (1992).

[30] J. McFarlane, J. C. Polanyi, J. G. Shapter, and J. M. Williamson, J. Photochem. and Photobiology, A: Chem. **46,** 139 (1989).

[31] D. J. Anderson and R. N. Rosenfeld, J. Chem. Phys. **94,** 7857 (1991).

[32] C. E. M. Strauss, S. H. Kable, G. K. Chawla, P. L. Houston, and I. R. Burak, J. Chem. Phys. **94,** 1837 (1991).

[33] G. Brauer, *Handbook of Preparative Inorganic Chemistry*, 2nd edition ed. (Academic, New York, 1963).

[34] D. L. Osborn, D. J. Leahy, D. R. Cyr, and D. M. Neumark, J. Chem. Phys. **104,** 5026 (1996).

[35] R. B. Metz, A. Weaver, S. E. Bradforth, T. N. Kitsopoulos, and D. M. Neumark, J. Phys. Chem. **94,** 1377 (1990).

[36] C. Xu, G. R. Burton, T. R. Taylor, and D. M. Neumark, J. Chem. Phys. **107,** 3428 (1997).

[37] R. E. Continetti, D. R. Cyr, R. B. Metz, and D. M. Neumark, Chem. Phys. Lett. **182,** 406 (1991).

[38] D. R. Cyr, R. E. Continetti, R. B. Metz, D. L. Osborn, and D. M. Neumark, J. Chem. Phys. **97,** 4937 (1992).

[39] GAUSSIAN 92, M. J. Frisch, G. W. Trucks, M. Head-Gordon, P. M. W. Gill, M. W. Wong, J. B. Foresman, B. G. Johnson, H. B. Schlegel, M. A. Robb, E. S. Replogel, R. Gomperts, J. L. Andres, K. Raghavachari, J. S. Binkley, C. Gonzalez, R. L. Martin, D. J. Fox, D. J. Defrees, J. Baker, J. J. P. Stewart, and J. A. Pople (Gaussian Inc., Pittsburgh, PA, 1992).

[40] J. T. Hougen, J. Chem. Phys. **36,** 1874 (1962).

[41] D. L. Osborn, D. H. Mordaunt, H. Choi, R. T. Bise, and D. M. Neumark, J. Chem. Phys. **106,** 10087 (1997).

[42] R. D. Levine and R. B. Bernstein, *Molecular Reaction Dynamics and Chemical Reactivity* (Oxford University Press, New York, 1987).

[43] P. Pechukas and J. C. Light, J. Chem. Phys. **42,** 3281 (1965).

[44] P. Pechukas, J. C. Light, and C. Rankin, J. Chem. Phys. **44,** 794 (1966).

[45] M. Hunter, S. A. Reid, D. C. Robie, and H. Reisler, J. Chem. Phys. **99,** 1093 (1993).

[46] R. G. Gilbert, *Theory of Unimolecular and Recombination Reactions* (Blackwell Scientific Publications, Oxford, 1990).

[47] D. L. Osborn, H. Choi, D. H. Mordaunt, R. T. Bise, D. M. Neumark, and C. M. Rohlfing, J. Chem. Phys. **106,** 3049 (1997).

Chapter 3. Photodissociation Dynamics of the Ethoxy Radical (C_2H_5O)

Abstract

Photodissociation of the ethoxy (C_2H_5O) radical is investigated using photofragment translational spectroscopy. The ethoxy radical is generated by photodetachment of $C_2H_5O^-$ and subsequently dissociated by photon absorption in the range of 270-220 nm; no dissociation is seen at higher wavelengths. The photofragment yield (PFY) spectrum is structureless, but exhibits abrupt increases in intensity at 260 and 225 nm. The product mass distribution shows that C_2H_5O dissociates into a vinyl radical (C_2H_3) and a water (H_2O) throughout the entire absorption band. The translational energy $P(E_T)$ distributions for this channel are largely insensitive to photon energy. However, at the two highest photon energies (5.51 and 5.96eV), a new feature appears at $E_T \leq 0.3$eV which is tentatively assigned as production of an excited state of C_2H_3.

I. Introduction

Alkoxy radicals play a significant role as reaction intermediates in hydrocarbon combustion chemistry. The ethoxy (C_2H_5O) radical is particularly important, as it is believed to be a reaction intermediate in the C_2H_4 + OH[1-15] and C_2H_5 + O reactions,[16,17] undergoing dissociation to CH_3 + CH_2O and H + CH_2CHO. However, the excited state photochemistry of ethoxy radical is largely unknown. It is expected to be considerably more complex than in the methoxy radical, for which electronic excitation at hν < 4.65 eV leads solely to CH_3 + O products,[18] because ethoxy has many more low-lying dissociation channels: the four given above plus C_2H_3 + H_2O and CH_3CO + H_2. In this paper, we present the first study of the photodissociation spectroscopy and dynamics of ethoxy radical.

The electronic spectroscopy of C_2H_5O has been investigated in several laboratories. The emission spectrum from the $\tilde{B}\ ^2A' \rightarrow \tilde{X}\ ^2A''$ transition of the ethoxy radical was first observed in the range of 500-330 nm after photolysis of C_2H_5ONO.[19] Laser induced fluorescence spectra were subsequently recorded in a gas cell by two different groups, showing the origin transition at 342.4 nm (29,204 cm^{-1}) and a vibrational progression in the C-O stretching mode.[20,21] This set of measurements yielded a $\tilde{B}\ ^2A'$ state radiative lifetime of 1-1.8 μs. Rotationally resolved laser induced fluorescence was recorded for the origin and 9_0^2 transitions.[22,23] Recently, several additional vibrational modes of the $\tilde{X}\ ^2A''$ and $\tilde{B}\ ^2A'$ states were assigned in a laser induced fluorescence experiment by Zhu *et al.*[24]

Ruscic and Berkowitz[25] found the ionization potential of ethoxy to be 10.29±0.08 eV using photoionization mass spectrometry. Photoelectron (PES) spectra for the ethoxide anion were taken by Lineberger[26,27] and Ellison[28] groups and the electron affinity of ethoxy radical was determined to be 1.712±0.004eV. In a recent PES spectrum by Lineberger and coworkers,[27] transitions to the ground ($\tilde{X}\ ^2A''$) and low-lying excited ($\tilde{A}\ ^2A'$) states of C_2H_5O radical were resolved; these states are separated by only 355±10 cm^{-1} and are distinguished by their photoelectron angular distributions.

An interesting property of C_2H_5O particularly relevant to the results presented in this paper is the existence of chemically distinct isomers. Two stable isomers are known in addition to ethoxy radical (CH_3CH_2O): the 1-hydroxyethyl (CH_3CHOH), and 2-hydroxyethyl (CH_2CH_2OH) radicals. These chemically important species are less well-characterized than the ethoxy radical. Anastasi *et al.*[29,30] observed broad absorption spectra for both radicals in the range of 300-210 nm using a pulse radiolysis/kinetic absorption technique, although their assignment of the CH_2CH_2OH spectrum is called into question by the results reported here. The ionization potential of CH_3CHOH was measured to be <6.85 eV by photoionization mass spectrometry;[25] a more precise value of 6.64 ± 0.03 eV was recently obtained by Dyke *et al.*[31] using photoelectron spectroscopy.

Energetics of the three isomers were calculated by Schlegel and coworkers[32,33] and Curtiss *et al.*[34] In both studies, CH_3CHOH was found to be the most stable isomer, followed by CH_2CH_2OH and then CH_3CH_2O, with all three isomers lying within a 0.5 eV energy range. The study by Schlegel and coworkers[32,33] was primarily concerned with the OH + C_2H_4 reaction; in addition to the local minima, they calculated barrier heights for the various isomerization and dissociation pathways associated with this reaction. They

found the most facile reaction path to be the addition of OH to C_2H_4 to form CH_2CH_2OH, followed by isomerization to ethoxy radical over a 1.2 eV barrier and dissociation to CH_3 + CH_2O.

Ab initio calculations have also been applied to geometric isomers of $C_2H_5O^-$ anion and $C_2H_5O^+$ cation by Chiu *et al.*[35] and Curtiss *et al.*,[34] respectively. The ethoxide anion was found to lie almost 1 eV below the next most stable structure ($CH_2CH_2OH^-$) while CH_3CHOH^+ was the most stable cation. The cation has more stable isomers than either the neutral or anion, including protonated vinyl alcohol ($CH_2CHOH_2^+$), which lies 1.28 eV above CH_3CHOH^+.

In this paper, we investigate the photodissociation dynamics of C_2H_5O using our fast radical beam photofragment spectrometer. Here, a beam of C_2H_5O neutrals is prepared by laser photodetachment mass-selected $C_2H_5O^-$ ions and subsequently photodissociated by a second laser. We present a new dissociation band of ethoxy radicals and identify dissociation products as C_2H_3 + H_2O using our time- and position-sensitive detector.

II. Experimental Setup

The fast radical beam photofragmentation apparatus has been described in detail previously.[36,37] Briefly, oxygen gas (40 psi) bubbles through ethanol (C_2H_5OH) at 0 ^{O}C. The resulting mixture supersonically expands through a pulsed value and electric discharge channel into the source region of the apparatus.[38] Ions are created in the discharge channel by applying a voltage pulse of -600 V just after the valve opens, and

cool to ~50 K[39] during expansion. Deuterated ethoxide $C_2D_5O^-$ was produced by the same method.

Negative ions formed in the source region are accelerated to 6 keV and separated temporally by a time-of-flight (TOF) mass spectrometer. The $C_2H_5O^-$ ion packet is intersected by an excimer-pumped pulsed dye laser beam, photodetaching some anions to yield neutral C_2H_5O radicals. The photon energy used in these experiments, 1.80 eV, is just above the detachment threshold for the $\tilde{A}\ ^2A'$ state of the ethoxy radical,[27] so both the $\tilde{X}\ ^2A''$ and $\tilde{A}\ ^2A'$ states are populated in our radical beam, albeit with no vibrational excitation in either state. Since ethoxide is predicted[35] to be the lowest energy anion structure, no other isomers are expected in the anion beam. This is supported by the absence of photodetachment below the electron affinity of ethoxy radical, because any other isomers would have considerably lower vertical detachment energies.[32,34,35]

Any remaining ions after the photodetachment pulse are removed by application of an electrical deflection pulse. The neutral beam is then crossed by a second excimer-pumped tunable dye laser beam. The resulting photofragments are detected by microchannel plates with high efficiency (~50%) because of the high laboratory kinetic energy (6 keV). A beam block prevents undissociated radicals from impinging on the detector, while the photofragments with sufficient recoil energy E_T clear the beam block and strike the detector.

Two types of experiment are performed. First, the photofragment yield (PFY) spectrum is obtained by collecting the total flux of fragments as a function of the photodissociation laser wavelength. Second, at selected photon energies, the photofragments are collected in coincidence using a time- and position-sensitive detector.

By measuring the distance between the photofragments and the interval between their arrival times, we obtain the fragment masses, translational energy release, and scattering angle for each photodissociation event. From these we obtain the translational energy $P(E_T)$ distributions for each product mass channel.

The fragment masses are determined by the distance of the two fragments from the center of the detector. As a consequence, the fragment mass resolution mainly depends on the diameter of the parent radical beam at the detector. This diameter is around 1 mm, yielding a fragment mass resolution ($m/\Delta m$) of ~10.

In the coincidence experiment, the flight length from the photodissociation laser to the detector can be varied to optimize collection of low or high translational energy fragments. At longer flight lengths, more low energy fragments clear the beam block and hit the detector, but more high energy fragments miss the detector because of its finite size (40 mm diameter). In this paper, most of $P(E_T)$ distributions are obtained at 1m flight length, while some $P(E_T)$ distributions are obtained at 2m flight length to enhance detection of low energy product. In either case, the $P(E_T)$ distributions are generated from the raw data using a "detector acceptance function" that accounts for these effects.[40]

III. Results

A. Photofragment Yield (PFY) Spectrum of C_2H_5O

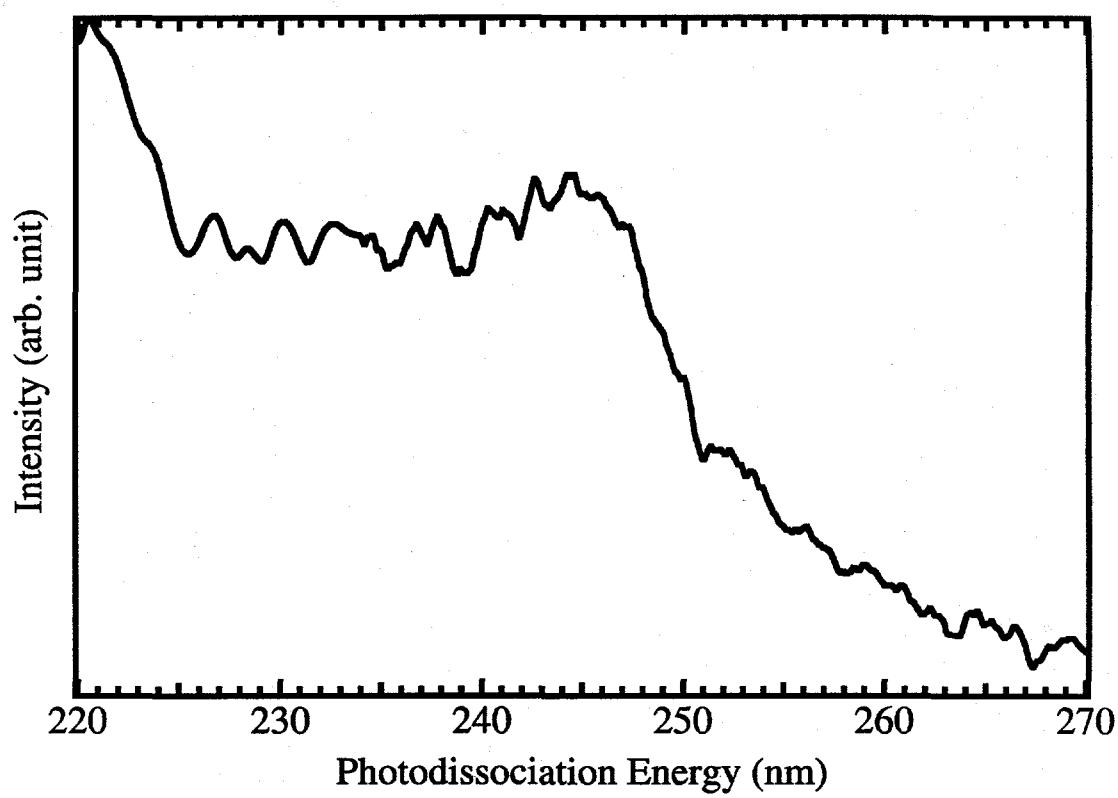

Figure 1: Photofragment Yield (PFY) spectrum of C_2H_5O.

The PFY spectrum obtained from C_2H_5O is shown in Fig. 1. This spectrum covers 270 – 220 nm (4.59- 5.64 eV) with 0.04 nm steps. No additional structure is resolved with finer step sizes. No significant dissociation signal was observed in the region of 342-311 nm, where laser-induced fluorescence from the $\tilde{B}\ ^2A' \rightarrow \tilde{X}\ ^2A''$ transition of C_2H_5O

radicals was previously reported.[20,21,24] The photofragment flux increases around 260 nm and 225 nm.

B. Product mass distribution

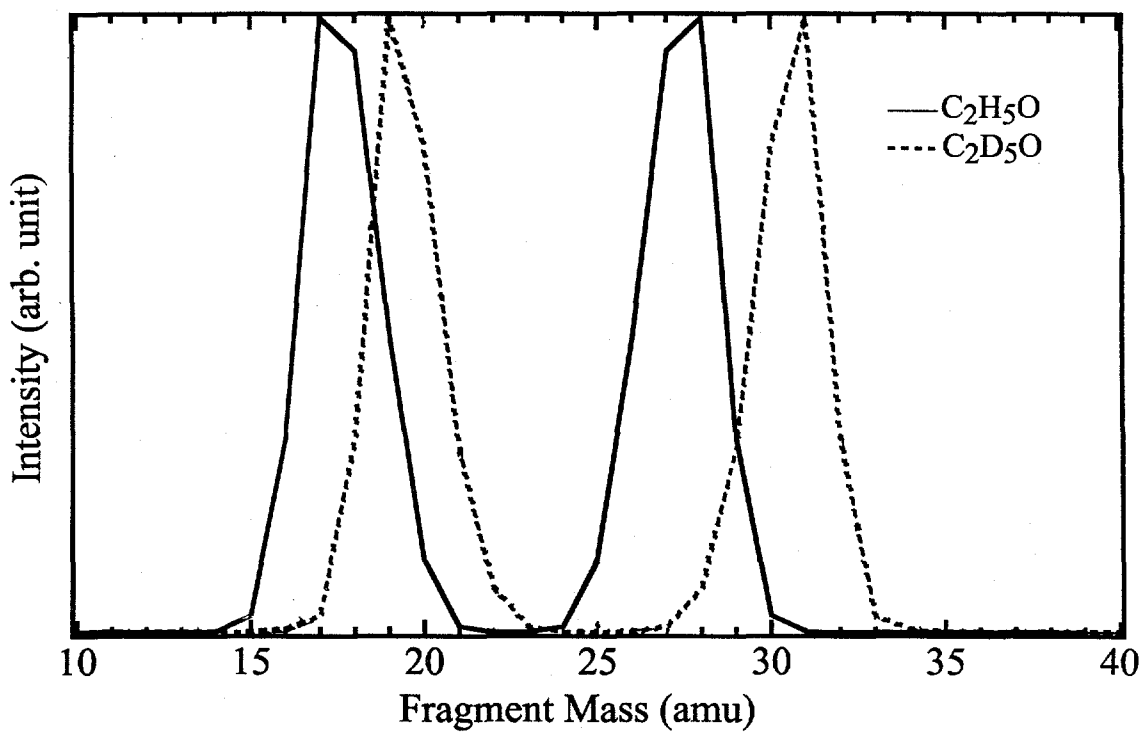

Figure 2: Photofragment mass spectrum of C_2H_5O and C_2D_5O. Solid line: with C_2H_5O. Dotted line: with C_2D_5O.

Several dissociation channels are energetically accessible in the photon energy range of Fig. 1:[41-43]

$C_2H_5O\ (\tilde{X}\ ^2A'') + h\nu \rightarrow$	$CH_3CO + H_2$	$\Delta_r H_0$	= -0.24 eV	(1)
	$CH_2O + CH_3$		= 0.40 eV	(2)
	$CH_3CHO + H$		= 0.65 eV	(3)
	$C_2H_3 + H_2O$		= 0.69 eV	(4)
	$C_2H_4 + OH$		= 1.05 eV	(5)

$$C_2H_5 + O \qquad = 3.92\ eV \qquad (6)$$

The coincidence detection scheme works well only if the fragment mass ratio is less than 5:1, otherwise the heavy fragment is generally blocked by the beam block and/or the light fragment misses the detector. Consequently, channels (1) and (3) cannot be detected in this experiment.

Figure 2 shows the product mass distribution for C_2H_5O and C_2D_5O photodissociation at 5.17eV. For C_2H_5O photodissociation, the average photofragment masses are 17.6 amu and 27.4 amu for the light and heavy masses, respectively, a result which could originate from channel (4) and/or (5) given our relatively poor fragment mass resolution. However, isotopic substitution from C_2H_5O to C_2D_5O results in a shift of 2 amu for the light mass and 3 amu for the heavy mass while showing no increase in peak width, indicating there are two hydrogen atoms on the light fragment and three on the heavy fragment. There is no significant change in mass distribution or isotope shift over the range of photon energies investigated here, nor over the translational energy range at a particular photon energy. Hence channel (4), $C_2H_3 + H_2O$, appears to be the dominant dissociation channel for which the product mass ratio is less than 5:1.

C. Translational Energy $P(E_T)$ distributions of C_2H_5O and C_2D_5O

Figure 3 shows $P(E_T)$ distributions for C_2H_3+H_2O from C_2H_5O and C_2D_5O at selected photon energies using a flight length of 1 m. $P(E_T)$ distributions from C_2H_5O are shown on the left side of Figure 3 and those from C_2D_5O are shown on the right side of Figure 3.

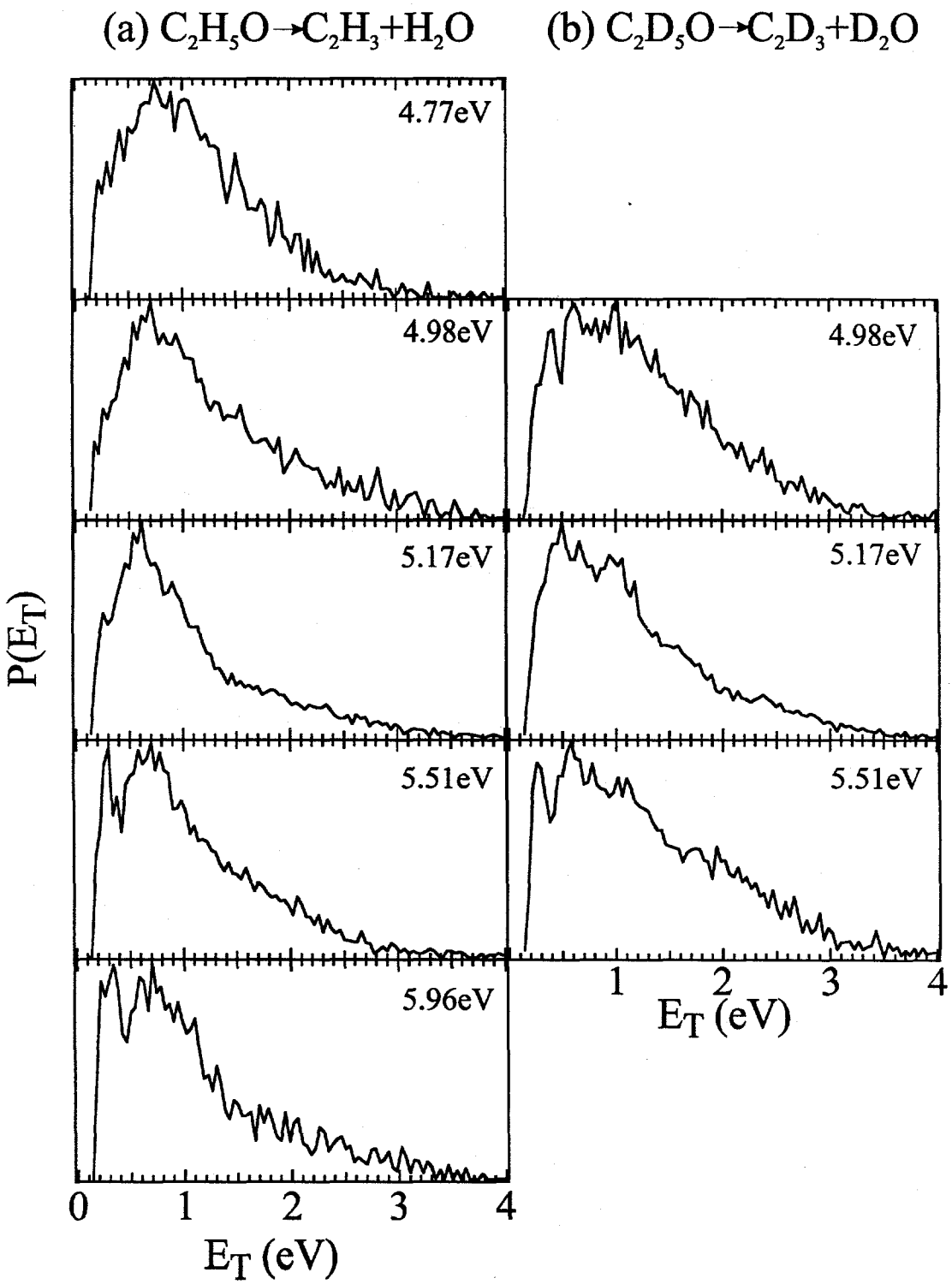

Figure 3: Translational energy distributions $P(E_T)$ of (a) C_2H_5O and (b) C_2D_5O at excitation energies shown at the right upper corner.

For C_2H_5O dissociation at $h\nu \leq 5.17$ eV, the $P(E_T)$ distributions show a single feature, peaking around 0.7 eV and extending to 4 eV. This feature narrows somewhat as the photon energy is raised. The $P(E_T)$ distributions for C_2D_5O dissociation at the same photon energies have the same general shape, although the peak is slightly broader toward high E_T. For $h\nu \geq 5.51$eV, a new peak appears around $E_T = 0.3$ eV. At 1 m flight length, most of the signal at $E_T \leq 0.3$ eV is blocked, so the flight length was increased to 2 m to better investigate this new feature.

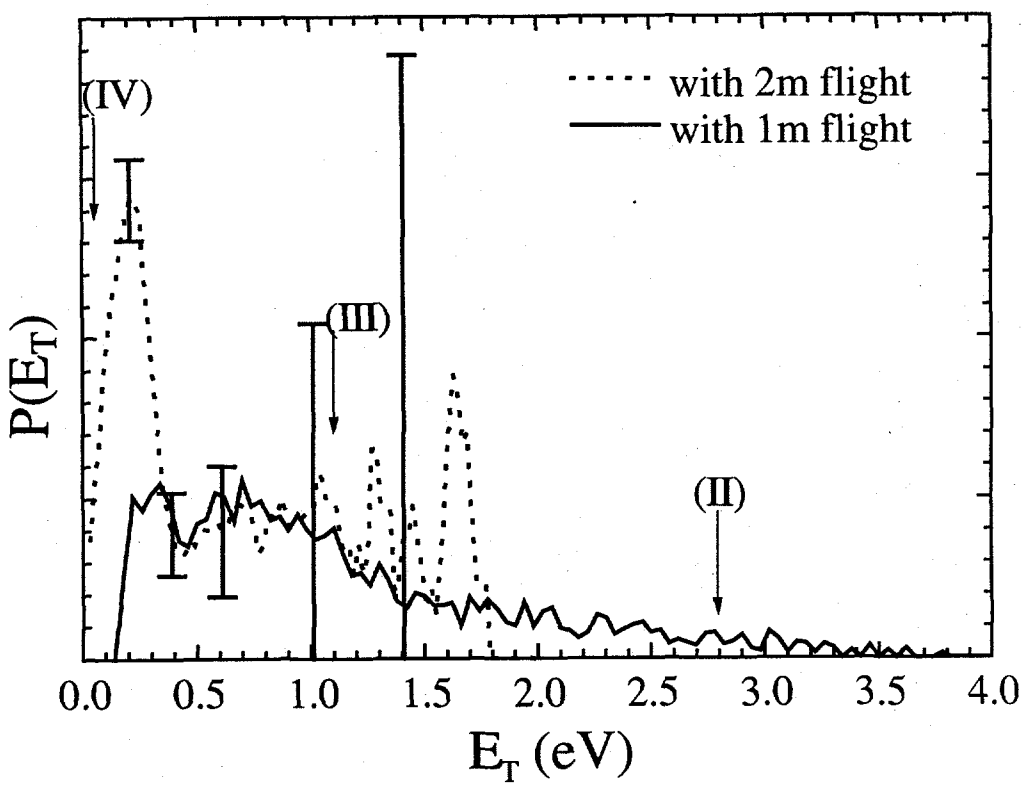

Figure 4: Translational energy distributions $P(E_T)$ of C_2H_5O at 5.96 eV with the different flight length. Solid and dotted lines represent data with 1m and 2m flight lengths, respectively. Arrows indicate the maximum E_T for channels (II)-(IV).

Fig. 4 shows the $P(E_T)$ distributions of C_2H_5O obtained at 5.96eV at flight lengths of 1 m (solid) and 2 m (dotted). The distribution at 2 m is now dominated by the low energy feature, which appears to peak at an energy even lower than 0.3 eV. Note that the error bars for the data with 2 m flight length increase dramatically above 1.0 eV due to the poor collection efficiency of the fragments, since many of the lighter fragments (H_2O) miss the detector.

IV. Discussion

In this section, we consider the origin of the diffuse band in the PFY spectrum and the dissociation mechanism associated with excitation of this band.

A. Origin of the diffuse band in the PFY spectrum

Our PFY spectrum shows a very broad band extending from 270-220 nm, with intensity increases at 260nm and 225nm. This band lies well to the blue of the $\tilde{B}\,^2A' \rightarrow \tilde{X}\,^2A''$ transition, a highly structured band covering 342-311 nm which has been seen previously using laser-induced fluorescence. It therefore appears likely that we are observing a new electronic transition in C_2H_5O rather than the blue tail of the $\tilde{B}\,^2A' \rightarrow \tilde{X}\,^2A''$ transition.

The $\tilde{B}\,^2A' \rightarrow \tilde{X}\,^2A''$ transition in ethoxy is similar to the well-studied $\tilde{A}\,^2A_1 \leftarrow \tilde{X}\,^2E$ transition in the methoxy (CH_3O) radical.[18,44] Both occur in approximately the same energy range and show significant vibrational activity in the C-O stretch (ν_3 in CH_3O, and ν_{10} in C_2H_5O), and both have been assigned to excitation of a C-O σ-bonding electron into a half-filled $p\pi$ localized on the O atom. More specifically,

the ground state of C_2H_5O has the electronic configuration $\ldots(8a')^2(2a'')^2(9a')^2(10a')^2(3a'')^1$. The 3a" and 10a' orbitals are O pπ orbitals, the 9a' orbital is the C-O σ-orbital, and the $\tilde{B}\ ^2A' \rightarrow \tilde{X}\ ^2A''$ transition corresponds to 3a"←9a' excitation. The PFY spectrum in Fig. 1 appears to consist of two electronic bands, with the higher energy band commencing at 225 nm. We tentatively assign these two bands to excitation of the 2a" (C-H σ of CH_3 component in C_2H_5O) and 8a'(C-C σ and C-O σ) electrons to the half-filled O pπ orbital.

Note that the $\tilde{A}\ ^2A'$ state of ethoxy is also formed at the photodetachment energy used to generate the radicals. This state, which lies only 350 cm^{-1} above the ground state,[27] has the electronic configuration ... $(10a')^1(3a'')^2$ and differs from the $\tilde{X}\ ^2A''$ state only in the orientation of the half-filled O pπ orbital. Hence, transitions originating from the $\tilde{A}\ ^2A'$ state should also contribute to the PFY spectrum in Fig. 1. However, based on the above assignment, the upper state will be the same as for the transitions originating from the $\tilde{X}\ ^2A''$ state. We thus expect that bands originating from the two states should be separated by only 350 cm^{-1}, and the excited state dynamics will be the same.

There are two additional points of interest concerning the ethoxy PFY spectrum. First, the band in Fig. 1 is remarkably similar, although not identical, to the electronic absorption band assigned by Anastasi *et al.*[30] to the 2-hydroxyethyl (CH_2CH_2OH) radical. In their experiment, OH was reacted with C_2H_4 at pressures high enough to collisionally stabilize the CH_2CH_2OH adduct, which was then observed as a transient absorption feature. However, the calculations by Schlegel *et al.*[32] show that the isomerization barrier for $CH_2CH_2OH \rightarrow CH_3CH_2O$ is comparable to the entrance channel barrier for addition of OH to C_2H_4. This calculation suggests that at least some

isomerization to ethoxy could occur in the experiment by Anastasi *et al.* Such a process would explain the similarity between our PFY spectrum, which originates solely from ethoxy radical, and their transient absorption spectrum. Our observation of the ethoxy band in Fig. 1 also resolves a discrepancy in the product branching ratio of the F + C_2H_5OH reaction, for which Anastasi *et al.* find a lower value for CH_3CH_2O production relative to CH_2CH_2OH and CH_3CHOH than in previous work that used isotopic labeling to distinguish among product isomers;[45] Anastasi *et al.* obtained their branching ratios by analyzing the transient absorption from 300-225 nm and assuming the ethoxy absorption in this region was negligible.

Finally, we consider the absence of dissociation from the $\tilde{B}\ ^2A'$ state of ethoxy. As mentioned above, this state is similar to the $\tilde{A}\ ^2A_1$ excited state of CH_3O, which is known to undergo predissociation to CH_3 + O when six or more quanta are excited in the C-O stretch;[44] this corresponds to 3793 cm^{-1} of vibrational excitation in the upper state. The 3_0^6 transition in CH_3O exhibits a shorter fluorescence lifetime than lower energy 3_0^n transitions,[46] consistent with the onset of predissociation for the ν_3=6 upper level. The predissociation results from a crossing between the bound $\tilde{A}\ ^2A_1$ state and several repulsive states leading to CH_3+O.[47]

Because of the similarity between the $\tilde{A}\ ^2A_1$ state of CH_3O and $\tilde{B}\ ^2A'$ state of C_2H_5O, the possibility of predissociation on the $\tilde{B}\ ^2A'$ state of ethoxy radical was pointed by Inoue *et al.*[20] In the ethoxy radical, the origin of the $\tilde{B}\ ^2A' \leftarrow \tilde{X}\ ^2A''$ transition at 29,204 cm^{-1} is 2,440 cm^{-1} lower in energy than the $\tilde{A}\ ^2A_1 \leftarrow \tilde{X}\ ^2E$ transition in methoxy (T_0=31,644 cm^{-1}), and the dissociation threshold for C-O bond fission is about 900 cm^{-1}

higher in ethoxy (31,620 cm^{-1}). As a consequence, the highest energy ethoxy transition seen by laser-induced fluorescence[24] at 32,139 cm^{-1} results in an excited state with five quanta in the C-O bond that lies only 520 cm^{-1} above the C_2H_5+O asymptote, while the ν_3=6 level of the $\tilde{A}\,^2A_1$ in methoxy lies 4732 cm^{-1} above the threshold for dissociation to CH_3 + O.[44]. Thus, if the repulsive states correlating to this asymptote are similar to those in methoxy, considerably more excitation in the C-O stretch is needed in ethoxy for predissociation to occur, and the Franck-Condon factors for these transitions may simply be too small to be observable in our PFY spectrum.

B. Dissociation Mechanism

In our experiment, channel (4) ($C_2H_5O \rightarrow C_2H_3 + H_2O$) is observed as a major dissociation channel resulting from excitation of the band in Fig. 1. This result is somewhat surprising, given that several channels (2, 3, and 6) involving simple bond fission are accessible in this energy range. While we cannot easily detect H atom (or H_2) loss with our coincidence scheme, the mass spectra with isotopic substitution in Fig. 2 clearly indicate that channel 4 dominates over channels 2, 5, and 6.

For the ethoxy radical to dissociate into $C_2H_3 + H_2O$, two hydrogen atoms must migrate from carbon atom to oxygen atom of ethoxy radical before the dissociation. If we exclude the possibility of migration of two hydrogen atoms at the same time, the reaction path must pass through either the 1- or 2-hydroxyethyl structures en route to the possible transition states (TS) such as four-centered (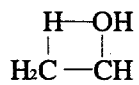), three-centered (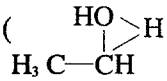) transition states, or CH_2CHOH_2. We consider possible dissociation mechanisms under this assumption.

First, we consider whether the first step in the dissociation mechanism is internal conversion of the electronically excited ethoxy radical to its ground state, followed by isomerization through either 1- or 2-hydroxyethyl radical, formation of the hydrogenated vinyl alcohol transition state, and dissociation:

$$CH_3CH_2O^* \xrightarrow{IC} CH_3CH_2O \rightarrow CH_3CHOH \rightarrow TS \rightarrow C_2H_3 + H_2O \quad (A)$$

$$\xrightarrow{IC} CH_3CH_2O \rightarrow CH_2CH_2OH \rightarrow TS \rightarrow C_2H_3 + H_2O \quad (B)$$

Based on the *ab initio* calculations by Schlegel and coworkers,[32,33] the isomerization barriers from ethoxy radical to 1- and 2- hydroxyethyl radicals are 1.2 and 1.3 eV, respectively. However, the barriers for dissociation of ground state ethoxy radical to CH_3+CH_2O and H+CH_3CHO are considerably lower, 0.8 and 1.0 eV, respectively, so one would expect dissociation to either of these channels rather than isomerization subsequent to internal conversion. Even if isomerization to either hydroxyethyl radical did occur, one would expect 2-hydroxyethyl to dissociate to OH + C_2H_4 rather than access the transition states (TS) to C_2H_3 + H_2O which are expected to lie well above the transition state to OH + C_2H_4 based on the distortion of geometry, and the 1-hydroxyethyl would be far more likely to isomerize to the 2-hydroxyethyl radical or dissociate to H + CH_3CHO than pass through the TS. We also note that C_2H_3 + H_2O is not seen as a product from either the OH + C_2H_4 or O + C_2H_5 reactions, both of which are believed to involve ethoxy radical as a reactive intermediate, instead, channels 2 and 3 are the major products.[1,17] Overall, it appears unlikely that the products we observe result from internal conversion followed by ground state dynamics.

Alternatively, the reaction pathway can occur on electronically excited surfaces as follows:

$$CH_3CH_2O^* \rightarrow CH_3CHOH^* \rightarrow TS \rightarrow C_2H_3 + H_2O \qquad (A')$$

$$\rightarrow CH_2CH_2OH^* \rightarrow TS \rightarrow C_2H_3 + H_2O \qquad (B')$$

For either A' or B' to occur, isomerization must happen more rapidly than either dissociation or internal conversion in the electronically excited ethoxy and hydroxyethyl radicals. These conditions imply that the excited states are bound with respect to dissociation, and that the isomerization barriers between structures are relatively low. Figure 5 shows the relative energies of ethoxy, 1-hydroxyethyl, 2-hydroxyethyl radicals using the calculations by Curtiss *et al.*[34] For these three isomers, we also show the energy interval over which electronic excitation was observed based on our PFY spectrum for ethoxy radical and the absorption spectra by Anastasi *et al.* [29,30] for the other two radicals.

As shown in Fig. 5, the excited state of 1-hydroxyethyl radical lies 4.13- 5.63 eV above the ground state and 2.51-1.01 eV below CH_3CHOH^+. A similar species, the isopropyl radical ($CH_3C(CH_3)H$), was found to have an ionization potential (7.37±0.02eV) 0.73eV higher than 1-hydoxyethyl radical (6.64±0.02eV).[48] It has three excited states which lie 2.78, 2.05, 1.20 eV below $CH_3C(CH_3)H^+$ and were assigned as 3s, 3p, and 3d Rydberg states.[49] Therefore, the excited state of 1-hydroxyethyl radical shown in Fig. 5 might be a Rydberg state. A Rydberg state of 1-hydroxyethyl radical can be regarded as $(CH_3CHOH)^+(e)$. The reaction paths for intramolecular hydrogen transfer in the ground states of malonaldehyde neutral and cations were calculated by Sobolewski *et al.*[50] It is found that the barrier height ($30cm^{-1}$) in the ground state of the cation is much smaller than that ($1100cm^{-1}$) of the neutral. Therefore, hydrogen migration from ethoxy to 1-hydroxyethyl or from 1-hydroxyethyl to TS might have a small barrier on the excited state, if this state has significant Rydberg character.

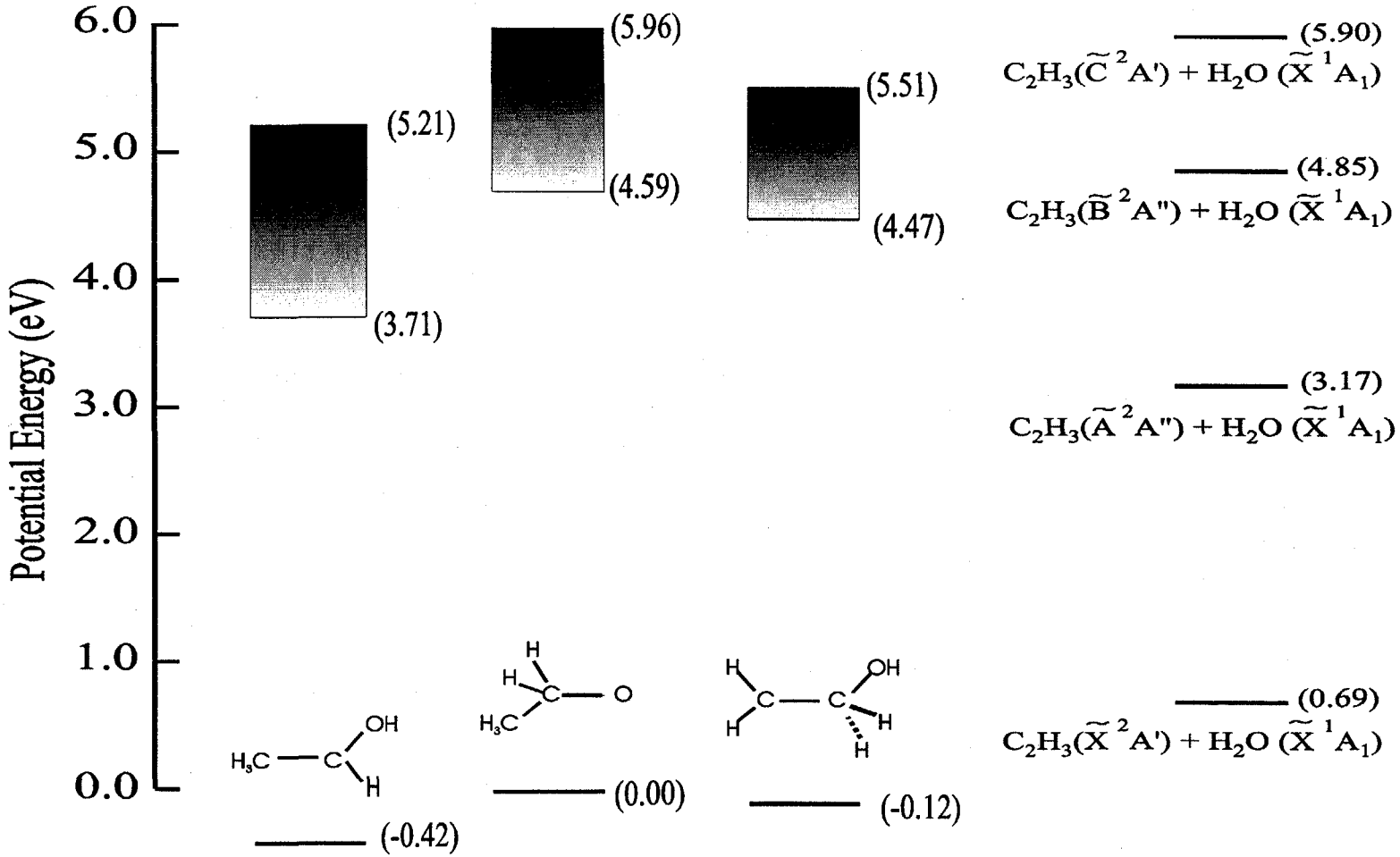

Figure 5: Potential energy diagram for C_2H_5O. Relative energies of C_2H_5O isomers are obtained from reference.[34] Filled boxes represent absorption bands observed by us for the ethoxy radical (C_2H_5O) and by Anastasi *et al.*[29,30] for the 1-hydroxyethyl (CH_3CHOH) and the 2-hydroxyethyl (CH_2CH_2OH) radicals. Relative energies for the photoproducts are determined using values in references [51-53].

We regard mechanisms A' or B' as the most likely candidates to explain our observation of significant production of $C_2H_3 + H_2O$ from excitation of ethoxy radical, but further experimental and/or theoretical investigation of the excited states involved is clearly necessary.

Finally, we consider the low energy feature ($E_T \leq 0.3$eV) in the $P(E_T)$ distributions shown in Figs. 3 and 4 at photon energies ≥ 5.51 eV. This feature likely corresponds to formation of C_2H_3 in a low-lying excited state. Two such states, the $\tilde{A}\ ^2A''$ and $\tilde{C}\ ^2A'$ states, have been observed in absorption spectra[51,52] and the $\tilde{B}\ ^2A''$ state was theoretically identified.[53] In our experiment, the production of these three excited states is energetically possible as follows:

$$C_2H_5O\,(\tilde{X}\ ^2A'') + h\nu \rightarrow C_2H_3(\tilde{X}\ ^2A') + H_2O(\tilde{X}\ ^1A_1) \quad \Delta_rH_0 = 0.69\text{ eV} \quad \text{(I)}$$

$$C_2H_3(\tilde{A}\ ^2A'') + H_2O(\tilde{X}\ ^1A_1) \quad = 3.17\text{ eV} \quad \text{(II)}$$

$$C_2H_3(\tilde{B}\ ^2A'') + H_2O(\tilde{X}\ ^1A_1) \quad = 4.85\text{ eV} \quad \text{(III)}$$

$$C_2H_3(\tilde{C}\ ^2A') + H_2O(\tilde{X}\ ^1A_1) \quad \leq 5.90\text{eV} \quad \text{(IV)}$$

In Fig. 4, ($h\nu$=5.96eV), the maximum E_T for channels II-IV are indicated with arrows. Channel III is the closest lying open channel, and we tentatively assign the low energy feature to this channel. However, the dissociation energy for channel IV has not been determined very well because only a broad absorption spectrum has been observed for the $\tilde{C}\ ^2A' \leftarrow \tilde{X}\ ^2A'$ transition of C_2H_3 radical. Therefore, the channel IV cannot be excluded as the origin of the low energy feature. In any case, the appearance of the low energy feature in the $P(E_T)$ distributions coincides with the abrupt increase in the PFY yield at 225 nm, indicating that the excited state of ethoxy radical accessed at that wavelength preferentially dissociates to either III or

V. Conclusions

The photodissociation spectroscopy and dynamics of ethoxy radicals were studied using fast radical beam photofragment translational spectroscopy. The photofragment yield (PFY) spectrum in the range of 270-220 nm is structureless, but clearly exhibits an abrupt increases in intensity at 260 and 225nm. These are tentatively assigned as two different electronic transitions. No significant dissociation signal was observed in the region where the fluorescence from $\tilde{B}\ ^2A' \rightarrow \tilde{X}\ ^2A''$ transition of C_2H_5O radicals was observed, indicating that the $\tilde{B}\ ^2A'$state of C_2H_5O is not dissociative.

The photofragment mass distribution shows that the major dissociation channel is $C_2H_3 + H_2O$. Most of the $P(E_T)$ distributions for $C_2H_3 + H_2O$ from C_2H_5O dissociation shows a single feature, peaking around 0.7eV and extending up to 4 eV. However, at photon energies beyond the onset of the second electronic band (225 nm or 5.51 eV), a new feature appears at $E_T \leq 0.3$eV which is attributed to production to an excited state of C_2H_3.

The observation of $C_2H_3 + H_2O$ products is surprising, because two hydrogen atoms must move before the dissociation. We propose a dissociation mechanism in which the excited ethoxy radicals isomerize through excited states of either the 1- or 2-hydroxyethyl radicals and then undergo dissociation to $C_2H_3 + H_2O$. Confirmation of this mechanism would be greatly aided by further *ab initio* work on the excited states of ethoxy and its isomers.

ACKNOWLEDGEMENTS

This research is supported by the Director, Office of Energy Research, Office of Basic Energy Sciences, Chemical Sciences Division, of the U. S. Department of Energy under Contract No. DE-AC03-76SF00098.

References

[1] E. D. Morris, Jr., D. H. Stedman, and H. Niki, J. Am. Chem. Soc **93,** 3570 (1971).

[2] I. W. Smith and R. J. Zellner, J. Chem. Soc., Faraday Trans. 2 **69,** 1617 (1973).

[3] A. V. Pastrana and R. W. Carr, Jr., J. Phys. Chem **79,** 765 (1975).

[4] R. Overend and G. Paraskevpoulos, J. Chem. Phys. **67,** 674 (1977).

[5] C. J. Howard, J. Chem. Phys. **65,** 4771 (1976).

[6] A. C. Lloyd, K. R. Darnall, A. M. Winer, and J. N. Pitts, Jr., J. Phys. Chem. **80,** 789 (1976).

[7] N. R. Greiner, J. Chem. Phys. **53,** 1284 (1970).

[8] S. Gordon and N. A. Mulac, Int. J. Chem. Kinet. Symp. **1,** 289 (1975).

[9] D. D. Davis, S. Fischer, R. Schiff, R. T. Watson, and W. J. Bolliner, J. Chem. Phys. **65,** 1707 (1975).

[10] R. A. Cox, Int. J. Chem. Kinet. Symp. **1,** 379 (1975).

[11] R. Atkinson, R. A. Perry, and J. N. Pitts, Jr., J. Chem. Phys **66,** 1197 (1977).

[12] R. Zellner and K. Lorenz, J. Phys. Chem. **88,** 984 (1984).

[13] F. P. Tully, Chem. Phys. Lett. **96,** 148 (1983).

[14] T. Klein, I. Barnes, K. H. Becker, E. H. Fink, and F. Zabel, J. Phys. Chem. **88,** 5020 (1984).

[15] J. N. Bradley, W. D. Capey, R. W. Fair, and D. K. Pritchard, Int. J. Chem. Kinet. **8,** 549 (1976).

[16] L. Batt and R. T. Milne, Int. J. Chem. Kinet. **9,** 549 (1977).

[17] I. R. Slagle, D. Sarzynski, D. Gutman, J. A. Miller, and C. F. Melius, J. Chem. Soc., Faraday Trans. 2 **84,** 491 (1988).

[18] D. L. Osborn, D. J. Leahy, E. M. Ross, and D. M. Neumark, Chem. Phys. Lett. **235,** 484 (1995).

[19] K. Ohbayashi, H. Akimoto, and I. Tanaka, J. Phys. Chem. **81,** 798 (1977).

[20] G. Inoue, M. Okuda, and H. Akimoto, J. Chem. Phys. **75,** 2060 (1981).

[21] T. Ebata, H. Yanagishita, K. Obi, and I. Tanaka, Chem. Phys. **69,** 27 (1982).

[22] S. C. Foster, Y. Hsu, C. P. Damo, X. Liu, C. Kung, and T. A. Miller, J. Phys. Chem. **90,** 6766 (1986).

[23] X. Q. Tan, J. M. Williamson, S. C. Foster, and T. A. Miller, J. Phys. Chem. **97,** 9311 (1993).

[24] X. Zhu, M. M. Kamal, and P. Misra, Pure Appl. Opt. **5,** 1021 (1996).

[25] B. Ruscic and J. Berkowitz, J. Chem. Phys. **101,** 10936 (1994).

[26] G. B. Ellison, P. C. Engelking, and W. C. Lineberger, J. Chem. Phys. **86,** 4873 (1982).

[27] T. M. Ramond, G. E. Davico, R. L. Schwartz, and W. C. Lineberger, J. Chem. Phys. **(submitted)** (1999).

[28] T. T. Dang, E. L. Motell, M. J. Travers, E. P. Clifford, G. B. Ellison, C. H. Depuy, and V. M. Bierbaum, Int. J. Mass Spectrom. Ion Proc. **123,** 171 (1993).

[29] C. Anastasi, V. Simpson, J. Munk, and P. Pagsberg, Chem. Phys. Lett. **164,** 18 (1989).

[30] C. Anastasi, V. Simpson, J. Munk, and P. Pagsberg, J. Phys. Chem. **94,** 6327 (1990).

[31] J. M. Dyke, A. P. Grooves, E. P. F. Lee, and M. H. Zamanpour Niavaran, J. Phys. Chem. A **101,** 373 (1997).

[32] C. Sosa and H. B. Schlegel, J. Am. Chem. Soc. **109,** 7007 (1987).

[33] C. Gonzalez, C. Sosa, and H. B. Schlegel, J. Phys. Chem. **93,** 2435 (1989).

[34] L. A. Curtiss, D. J. Lucas, and J. A. Pople, J. Chem. Phys. **102,** 3292 (1995).

[35] S.-W. Chiu, K. Lau, and W. Li, J. Phys. Chem. A **103,** 6003 (1999).

[36] R. E. Continetti, D. R. Cyr, R. B. Metz, and D. M. Neumark, Chem. Phys. Lett. **182,** 406 (1991).

[37] D. R. Cyr, R. E. Continetti, R. B. Metz, D. L. Osborn, and D. M. Neumark, J. Chem. Phys. **97,** 4937 (1992).

[38] D. L. Osborn, D. J. Leahy, D. R. Cyr, and D. M. Neumark, J. Chem. Phys. **104,** 5026 (1996).

[39] D. L. Osborn, D. H. Mordaunt, H. Choi, R. T. Bise, and D. M. Neumark, J. Chem. Phys. **106,** 10087 (1997).

[40] R. E. Continetti, D. R. Cyr, D. L. Osborn, D. J. Leahy, and D. M. Neumark, J. Chem. Phys. **99,** 2616 (1993).

[41] K. M. Ervin, S. Gronert, S. E. Barlow, M. K. Giles, A. G. Harrison, V. M. Bierbaum, C. H. DePuy, W. C. Lineberger, and G. B. Ellison, J. Am. Chem. Soc. **112,** 5750 (1990).

[42] S. G. Lias, J. E. Bartmess, J. F. Liebman, J. L. Holmes, R. D. Levin, and W. G. Mallard, *Gas-Phase Ion and Neutral Thermochemistry, J. Chem. Phys. Ref. Data 17, Suppl. No. 1* (1988).

[43] M. W. Chase Jr., C. A. Davies, J. R. Downey Jr., D. J. Fruip, R. A. McDonald, and A. N. Syverud, *JANAF Thermochemical Tables, 3rd Ed., J. Chem. Phys. Ref. Data* ***14****, Suppl. No. 1.* (1985).

[44] D. L. Osborn, D. J. Leahy, and D. M. Neumark, J. Phys. Chem. A **101,** 6583 (1997).

[45] U. Meier, H. H. Grotheer, G. Riekert, and T. Just, Chem. Phys. Lett. **115,** 221 (1985).

[46] D. E. Powers, M. B. Pushkarsky, and T. A. Miller, J. Chem. Phys. **106,** 6878 (1997).

[47] Q. Cui and K. Morokuma, Chem. Phys. Lett. **263,** 54 (1996).

[48] J. Dyke, A. Ellis, N. Jonathan, and A. Morris, J. Chem. Soc. Faraday Trans. 2 **81,** 1573 (1985).

[49] H. R. Wendt and H. E. Hunziker, J. Chem. Phys, **81,** 717 (1984).

[50] A. L. Sobolewski and W. Domcke, Chem. Phys. Lett. **310,** 548 (1999).

[51] H. E. Hunziker, H. Kneppe, A. D. McLean, P. Siegbahn, and H. R. Wendt, Can. J. Chem. **61,** 993 (1983).

[52] A. Fahr, P. Hassanzadeh, and D. B. Atkinson, Chem. Phys. **236,** 43 (1998).

[53] A. M. Mebel, Y. Chen, and S. Lin, Chem. Phys. Lett. **275,** 19 (1997).

Chapter 4. PHOTODISSOCIATION OF LINEAR CARBON CLUSTERS C_n (n=4-6)

Abstract

The photodissociation of mass-selected linear carbon clusters (C_n, n = 4 – 6) is studied using fast beam photofragment translational spectroscopy. The photofragment yield (PFY) spectra consist of several continua spanning the whole visible and ultraviolet region. The product mass distributions for dissociation of C_n clusters are dominated by C_3 and its partner fragment C_{n-3}, although some minor channels are also identified for dissociation of C_4 and C_5 clusters. Translational energy $P(E_T)$ distributions for the C_3 + C_{n-3} channel were measured at several photolysis energies. The PFY spectra and $P(E_T)$ distributions indicate that multi-photon dissociation occurs at photon energies below the dissociation threshold, and that both single- and multi-photon dissociation occur above the threshold. The one-photon components of the $P(E_T)$ distributions can be modeled by phase space theory (PST), suggesting that photoexcitation is followed by internal conversion to the ground state. The PST analysis yields dissociation energies for $C_n \rightarrow C_n + C_{n-3}$ in reasonable agreement with recent Knudsen effusion mass spectrometry measurements.

I. INTRODUCTION

Linear carbon clusters have been identified as key reaction intermediates in combustion[1] and the interstellar medium[2-5] leading to the formation of fullerenes[6,7] and soot.[8] These observations have motivated numerous spectroscopic studies resulting in extensive characterization of the ground and, to a lesser extent, the low-lying electronic states of linear carbon clusters. However, there is less information on the photochemical and thermodynamic properties of carbon clusters. These properties are important for understanding the evolution of carbon cluster geometries with increasing size, namely the transformation from chains to mono- and polycyclic rings and ultimately to fullerenes and other three-dimensional structures. In this article, we address these issues by employing the technique of fast radical beam photofragment translational spectroscopy to study the photodissociation of mass-selected linear carbon clusters. By measuring photofragment yield spectra, product branching ratios, and product translational energy distributions, our experiments probe both the energetics and dissociation dynamics of these clusters.

Much of our understanding of carbon clusters derives from the classic paper of Pitzer and Clementi,[9] who proposed that small neutral clusters are linear molecules with cumulenic bonds. The even-numbered clusters were predicted to be open shell species with $^3\Sigma_g^-$ ground states and high electron affinities, while the odd-numbered clusters were expected to have closed shell $^1\Sigma_g^+$ ground states with considerably lower electron affinities. These predictions have generally been confirmed by experiment and theory.

The properties of carbon clusters have been extensively reviewed by Weltner and Van Zee[10] in 1989 and by Van Orden and Saykally[11] in 1998. As is described in the more recent review, a combination of high resolution gas phase and matrix spectroscopy, anion photodetachment spectroscopy, and electronic structure calculations has yielded rotational constants and vibrational frequencies for the ground states of linear carbon clusters as large as C_{13}. Ion mobility studies provide further information on these and larger clusters,[6,12,13] showing how the geometry of carbon cluster cations and anions evolve from linear to more complex structures as the number of atoms increases. From the perspective of the work to be presented here, the most important results are that the C_n^- anions are linear for $n \leq 9$ and that photodetachment of these anions yields linear neutral carbon clusters. [14-16]

There has also been considerable interest in the excited states of carbon clusters. Electronic transitions in carbon clusters have been proposed as possible candidates for the diffuse interstellar bands.[3,4,17,18] This has motivated Maier and coworkers[19-22] to study the ultraviolet (UV) and visible absorption spectroscopy of mass-selected carbon clusters deposited in a cryogenic matrix, obtaining vibrationally resolved electronic transitions for C_4, C_5 and C_6. Further information on excited electronic states comes from anion photoelectron spectroscopy,[14-16] which reveals states that are optically inaccessible from the neutral ground state, and electronic structure calculations.[23-28] Both experiment and theory indicate a large number of low-lying singlet and triplet states in carbon clusters, an important property from the point of view of the current paper.

Experimental heats of formation ΔH_f for carbon clusters have been previously

determined using Knudsen effusion mass spectrometry, in which the relative concentrations of C_n clusters in equilibrium with graphite at high temperature (2000-3000K) are measured. In 1959, Drowart *et al.* [29] obtained heats of formation of C_2-C_5 using this method. However, "third law" extrapolation to ΔH_f at 298 K (or 0 K) requires knowledge of the entropy of carbon clusters, and since some bend frequencies for these species were later found to be very low (i.e. 63 cm^{-1} for C_3 [30]), the entropy was underestimated in this early measurement.[31,32] More recently, Gingerich and co-workers[33-35] have performed improved Knudsen measurements. Using the most current spectroscopic data on carbon clusters in their third law extrapolation, they obtained new values of ΔH_f for C_2-C_7, and found significant differences (0.4-0.8 eV) from the original study.

The heats of formation and reaction of carbon clusters have also been calculated in a series of semi-empirical and *ab initio* studies. [23-25,36-41] There are significant differences in the calculated heats of formation, but because of the particular stability of C_3, dissociation of a larger cluster to at least one C_3 fragment is always the lowest energy channel. This is consistent with calculations and experiments for dissociation of carbon cluster anions and cations,[38,42-48] where neutral C_3 elimination is the dominant photodissociation channel.

In this paper, the photodissociation of mass-selected neutral carbon clusters C_4, C_5 and C_6 is investigated for the first time, using fast beam photofragment translational spectroscopy. Neutral carbon clusters are generated by laser photodetachment of the corresponding mass-selected anions. The neutral clusters are then photodissociated and

the photofragments detected. The apparatus is described in Sect. II. The experimental results for the photodissociation of C_4, C_5 and C_6 clusters are presented in Sect. III and analyzed in Sect. IV. The results show that multiphoton absorption occurs over a wide range of photon energies, while single-photon dissociation shows statistical behavior near the dissociation threshold. This unusual competition between single and multi-photon processes is discussed in Sect. V.

II. EXPERIMENTAL

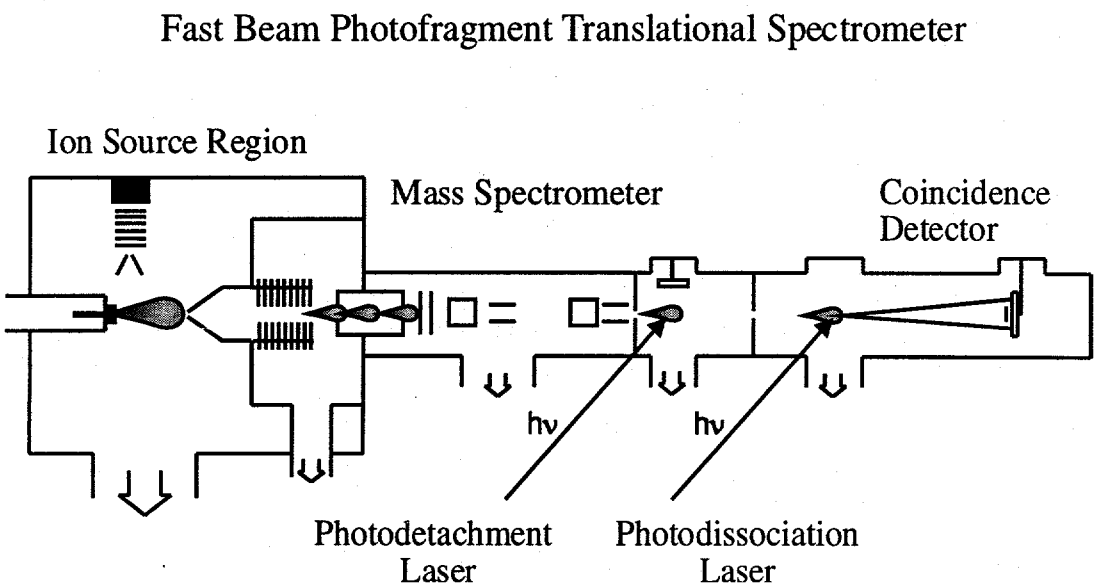

Figure 1. Schematic diagram of the experimental apparatus.

The experimental apparatus shown in Figure 1 has been previously described in detail;[49,50]only a brief description is given here. To generate carbon cluster anions, a pulsed free jet expansion of the gas mixture CO_2:C_2H_2:Ne (mole fraction 1:10:89) passes

through a pulsed electric discharge assembly[51] bolted onto the faceplate of the pulsed valve. The core of the free jet passes through a 2 mm diameter skimmer and the anions are accelerated to 6.5 keV. Mass-separation of the ions is accomplished using a collinear Bakker[52] type time-of-flight mass spectrometer. After collimation of the ion beam by a 1.0 mm pinhole, ions are photodetached by an excimer-pumped pulsed dye laser, triggered such that it photodetaches only the ion packet with the mass-to-charge ratio of interest. Thus a packet of mass-selected neutral radicals is produced. The remaining ions are deflected from the beam. Table 1 lists the photodetachment energy selected for each carbon cluster; this energy was chosen to lie just above the detachment threshold[16,53,54] so that the neutral clusters are produced in their vibrational ground states.

Table 1: Electron affinities and detachment energies used to generate carbon clusters. ([a] As reported by Arnold et. al.[15,53].)

	Literature Electron Affinity / eV[a]	Detachment Energy / eV
$C_4^- \rightarrow C_4 + e^-$	$3.882 \pm .010$	4.025
$C_5^- \rightarrow C_5 + e^-$	$2.839 \pm .008$	2.877
$C_6^- \rightarrow C_6 + e^-$	$4.185 \pm .006$	4.305

The radicals are collimated by another 1.0 mm pinhole and intersect a second pulsed laser, either an excimer-pumped dye laser or an ArF excimer laser operating at 193 nm. If photodissociation occurs, fragments recoiling out of the parent radical beam are detected with high sensitivity, *without* an ionization step, using microchannel plate

detectors. A beam block immediately in front of the detector stops the remaining neutral beam. Photodissociation occurs under collisionless conditions (10^{-9} Torr), and two types of experiments are performed.

First, the photofragment yield spectrum is obtained by integrating the total fragment flux as a function of photodissociation laser wavelength. Second, at selected fixed photon energies, the dissociation dynamics are investigated by detecting both fragments *in coincidence* from dissociation of a single parent radical. We directly measure three parameters using the time- and position-sensitive detector: the difference in fragment arrival times at the detector, τ, and the distances from the center of the parent neutral beam to each fragment on the detector face, r_1 and r_2. The mass ratio of the photofragments is determined by conservation of linear momentum,

$$\frac{m_1}{m_2} = \frac{r_2}{r_1}\left(1 - \frac{v_0\tau}{L}\right), \tag{1}$$

where v_0 and L are the parent neutral beam velocity and distance from the photolysis interaction region to the detector. The photofragment translational energy, E_T is also determined from the timing and position information and neutral parent beam energy, E_0,

$$E_T = E_0 \cdot \frac{m_1 m_2}{(m_1 + m_2)^2} \cdot \frac{\left[(v_0\tau)^2 + (r_1 + r_2)^2\right]}{L^2} \quad . \tag{2}$$

In the present experimental configuration the translational energy resolution is given by $\Delta E_T / E_T = 2.2\%$.

The flight length to detector (L) can be varied to optimize collection of low or high translational energy fragments. In this paper, $P(E_T)$ distributions for C_4 are reported at 1 m flight length, whereas those for C_5 and C_6 are reported at 2 m flight length. All data shown here are corrected with a "detector acceptance function" (DAF)[49] that accounts for the reduced acceptance of the detector for both high and low energy fragments.

III. RESULTS

A. Spectroscopy

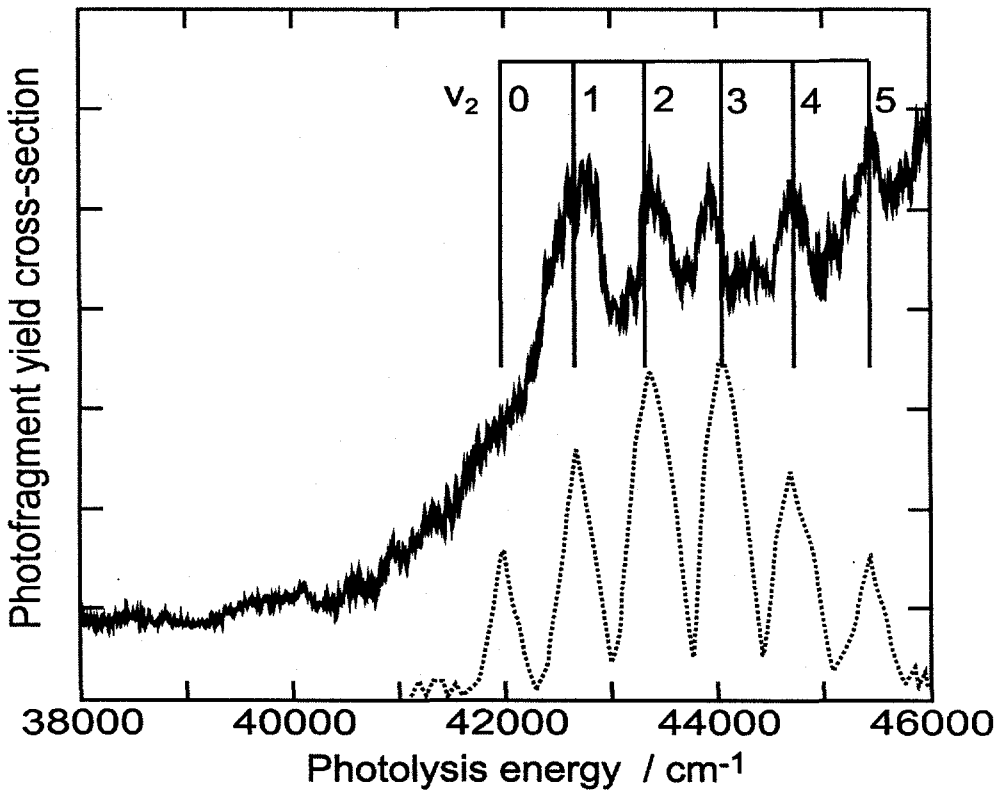

Figure 2. Ultraviolet photofragment yield cross-section of C_5 (solid line), and electronic absorption cross-section (dashed line) reproduced from Forney *et al.*[21] The energy comb plotted above the spectra corresponds to the 2_0^n vibrational progression of the $^1\Sigma_u^+ - \tilde{X}^1\Sigma_g^+$ electronic transition.

Photofragment yield (PFY) spectra were measured over several energy ranges covering the spectral regions 17980 - 43550, 39990 - 42910, and 34500 - 48000 cm^{-1}, for C_4, C_5 and C_6, respectively. A non-zero but unstructured PFY signal was observed over virtually the entire spectral region investigated for each species, generally increasing in intensity with photon energy. C_5 was the only species for which a structured band was observed. This is shown in Figure , superimposed on the spectrum obtained by Maier[21] in the same region and assigned to the 2_0^n (symmetric stretch) progression of an optically forbidden (vibronically allowed) electronic transition. The PFY and absorption spectra are not identical; the vibrational features in the PFY spectrum appear to be superimposed on a broader underlying continuum.

Since PFY signal is seen only when dissociation occurs, it is not surprising that the PFY and absorption spectra of carbon clusters are different. What is more intriguing is that any PFY signal is seen at over such an extended range of photon enerties. Based on the most recent experimental heats of formation by Gingerich and co-workers,[33-35] the bond dissociation energies for C_4, C_5, and C_6 are 5.08 eV (40970 cm^{-1}), 5.86 eV (47260 cm^{-1}), and 3.62 eV (29200 cm^{-1}), respectively. The observation of PFY signal at energies well below these values implies that multiphoton processes are at play here, in which dissociation occurs only after two or more photons are absorbed. Even the band in Figure 2 begins 0.6 eV below the Gingerich's bond dissociation energy, suggesting that it too is from multiphoton absorption. While power dependence studies were attempted at selected photolysis wavelengths, these were generally inconclusive because of the low signal levels observed. Note that similar multiphoton effects were observed in the

photodissociation of carbon cluster cations.[44,47]

B. Photofragment mass distributions

Analysis of the coincidence time and position data identifies the mass spectrum of the photofragments via Eq. (1). Quantitative branching ratios between competing photofragment channels are determined by convoluting the raw product mass distribution with the detector acceptance functions[49] for the respective product channels. C_4 primarily dissociates to $C + C_3$, with $C_2 + C_2$ products ranging from 5 to 17 % over the photolysis energy range in this study. C_5 dissociates mainly to $C_2 + C_3$; the yield of the minor $C + C_4$ channel is approximately 10 % at 5.74 and 5.96 eV and less than 1 % at all other incident photolysis energies. C_6 clusters exclusively dissociate to form two C_3 fragments. Overall, production of C_3 is either the dominant or exclusive channel.

C. Translational energy distributions

Figures 3, 4, and 5 report the $P(E_T)$ distributions obtained at selected photolysis energies for C_n dissociation into C_3 and its partner fragment (C_{n-3}) for n = 4, 5, and 6. The low E_T cutoff for each distribution represents the minimum value for which the detector acceptance function is non-zero; at lower values of E_T, no coincident events occur because one (or both) fragments is blocked by the beam block across the detector face. The larger error bars at low E_T reflect the amplification of the raw data in this energy range by the detector acceptance function.

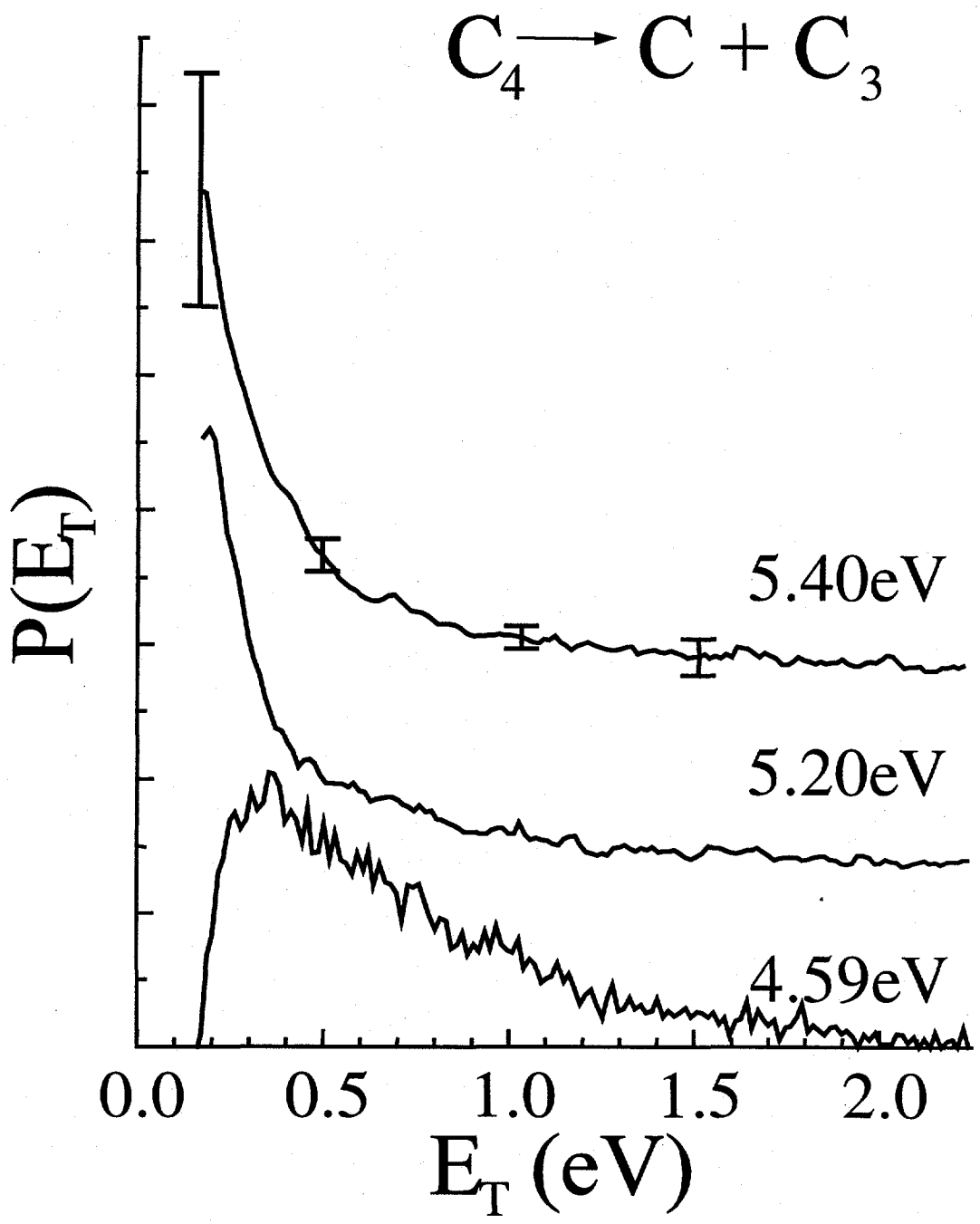

Figure 3. Photofragment translational energy $P(E_T)$ distributions for C_4 dissociation into C_3 + C at 1m flight length .

Three P(E_T) distributions for C_4 at a flight length of 1 m are shown in Figure 3. At a photon energy of 4.59 eV, signal is seen at translational energy as high as 2.1 eV. Distributions measured at lower photon energies (not shown) are essentially the same. At 5.20 eV, a new feature appears at $E_T \leq 0.4$eV which rises steeply toward low E_T while the high E_T part of the distribution is essentially unchanged. At 5.40 eV, the new feature broadens somewhat toward higher E_T, whereas the distribution beyond 0.7 eV is very similar to that seen at hν=4.59 eV. If the signal at 4.59 eV were due to a one-photon process, then the maximum observed E_T of ~ 2.1 eV would imply a bond dissociation energy of 2.5 eV, approximately 2.5 eV below the value of 5.08 eV obtained by Gingerich.[35] Thus it is reasonable to assume that two-photon processes contribute to the P(E_T) distribution. On the other hand, the sharp feature at low E_T seen for hν≥5.20 eV is consistent with one-photon dissociation and is assigned as such. We thus attribute the entire signal at hν = 4.59 eV to two-photon dissociation. The signal beyond E_T =0.6-0.7 eV at higher photon energies is also assigned to two-photon dissociation.

Figure 4 shows the P(E_T) distribution for C_5 at two different photon energies, 4.59 and 6.42 eV. The distribution at hν = 4.59 eV is broad and extends beyond E_T =1.0 eV, whereas an additional sharp peak at E_T =0.08 eV appears at hν = 6.42 eV. As with C_4, the feature at low E_T is assigned to one-photon dissociation whereas the entire distribution at 4.59 eV and the high E_T component of the distribution at 6.42 eV is assigned to two-photon dissociation. These data were obtained at a flight length of 2 m. The sharp peak at 6.42 eV is not apparent at 1 m flight length, because the translational energy of the photofragments is so low that they are largely blocked by the beam block at

the shorter flight length.

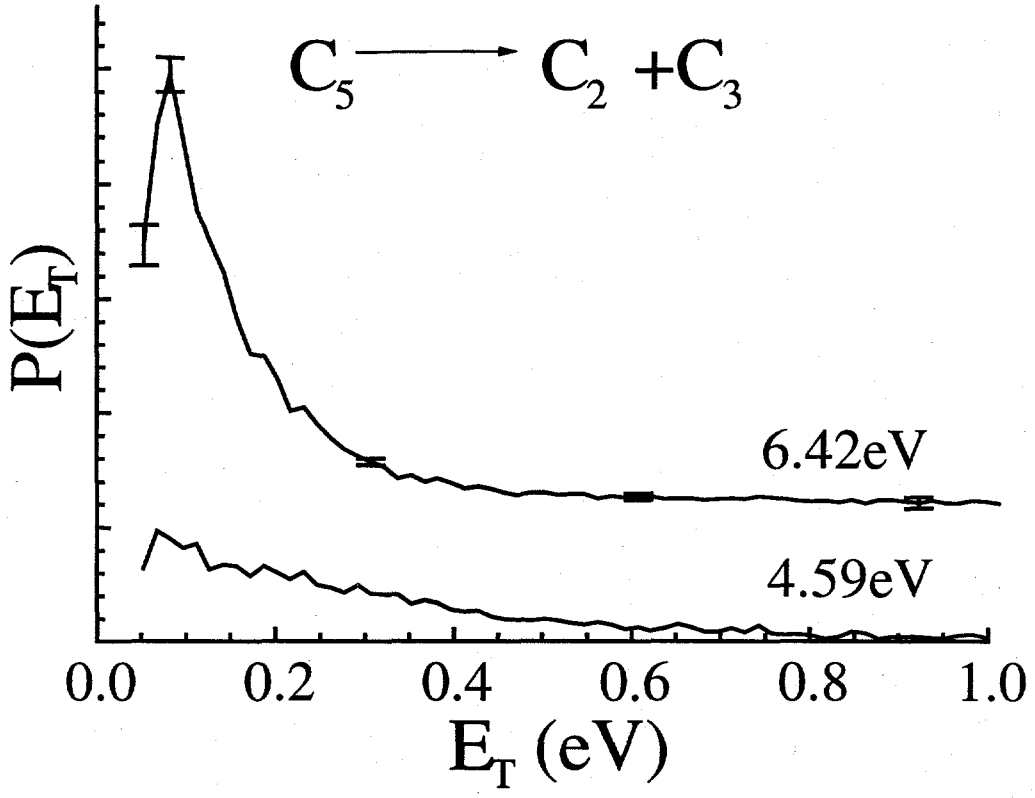

Figure 4. Photofragment translational energy P(E_T) distributions for C_5 dissociation into C_3 + C_2 at 2m flight length.

Figure 5 shows several P(E_T) distributions for C_6 dissociation measured at a flight length of 2 m. The distributions at 3.20 eV and 3.64 eV are quite similar, extending to E_T =1.3 eV. At hν=3.87 eV, a sharp feature at $E_T \leq 0.3$eV appears, and this feature shifts toward higher E_T and broadens as the photon energy is raised, similar to the trends seen for the sharp peak in C_4 photodissociation. Just as for the smaller clusters, the feature at low E_T is assigned to one-photon dissociation while the high E_T signal is attributed to two-photon dissociation. At photon energies where both processes occur, the delineation

between the one- and two-photon components is not as clear as for the smaller clusters. However, if the two-photon component is assumed to be independent of photon energy, as it appears to be for C_4 and C_5, then one can determine the two contributions using the $P(E_T)$ distributions at hν=3.64 eV where no one-photon signal is apparent.

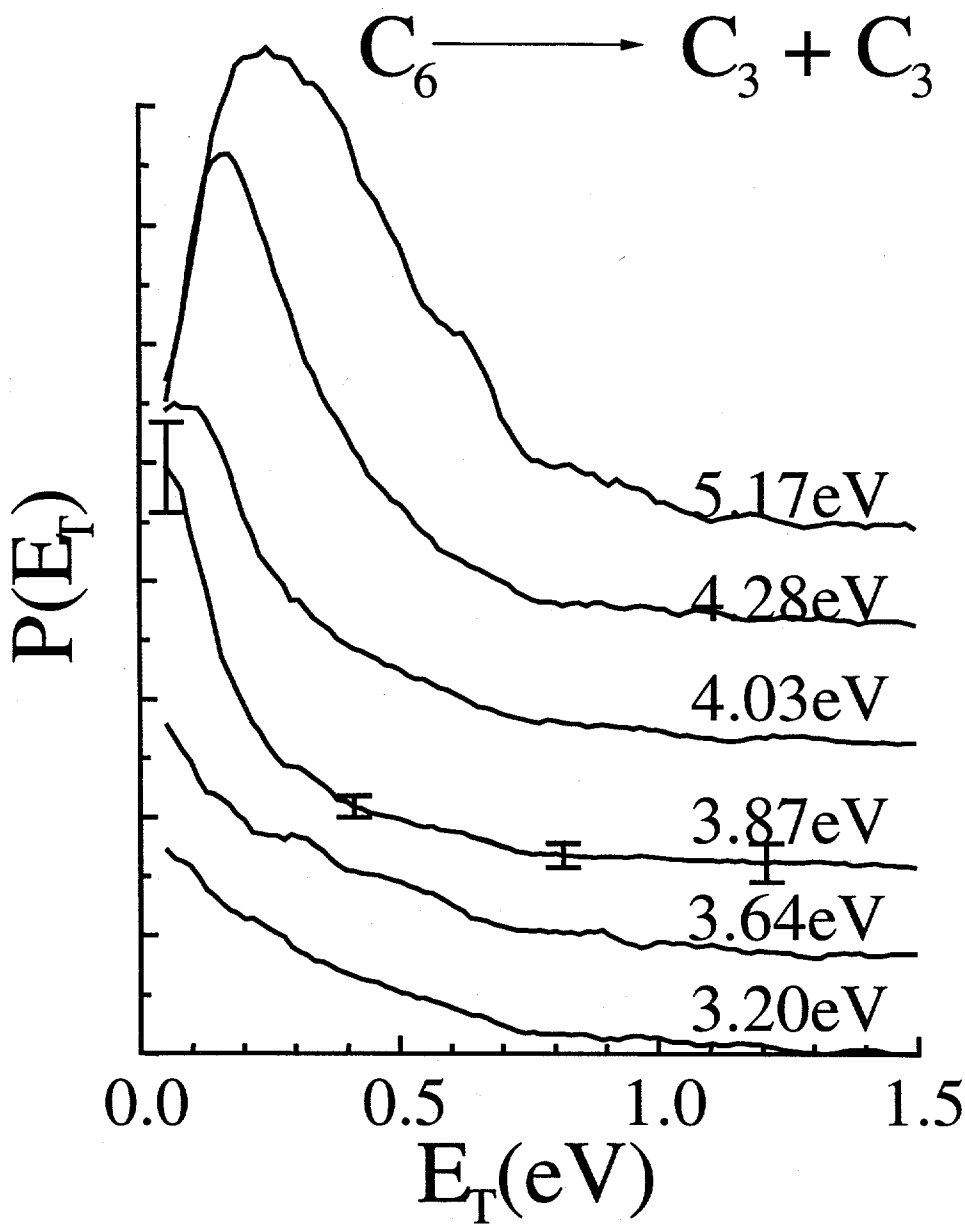

Figure 5. Photofragment translational energy $P(E_T)$ distributions for C_6 dissociation into $C_3 + C_3$ at 2m flight length.

IV. ANALYSIS

Our P(E_T) distributions show contributions from single and multi-photon dissociation. Both the form and energy dependence of one photon and multi-photon distributions are of importance in deducing the underlying dynamics. The one-photon distribution peaks at low E_T, and shows a weak but noticeable dependence on the photon energy, shifting toward higher E_T as the photon energy is raised above the threshold for the one-photon process. The multi-photon component of the P(E_T) distributions also is maximal at low E_T and appears to be independent of the photon energy. Translational energy distributions that peak at low E_T and show a weak dependence on total energy are often a signature of statistical dissociation on a potential energy surface with no exit barrier. Such a distribution could result if photoexcitation is followed by internal conversion to the ground state surface, and the resulting microcanonical ensemble lives long enough for the available energy to be randomized among the vibrational modes of the molecule. In order to test this possibility, both the one-photon and multi-photon distributions are calculated using phase space theory (PST), [55] a reasonable statistical model to apply in the case of barrierless dissociation.

In PST, all product states allowed by conservation of energy and angular momentum are assumed equally probable. Conservation of angular momentum requires that

$$\mathbf{J_{AB}} = \mathbf{J_A} + \mathbf{J_B} + \mathbf{L}, \qquad (3)$$

where $\mathbf{J_{AB}}$, $\mathbf{J_A}$, and $\mathbf{J_B}$ are the total angular momenta of parent (AB) and fragments (A and B), and **L** is the relative orbital angular momentum of the photofragments. Energy conservation and dynamical constraints (e.g. the centrifugal barrier) impose an upper limit l_{max} on L assuming a $V(r) = -C_0/r^6$ potential[56]

$$L(L+1)h^2 \leq 24\pi^2\mu C_0^{1/3}(E_T/2)^{2/3}, \qquad (4)$$

where μ is the reduced mass of the photofragments.

The resulting translational energy distributions are calculated using[56]

$$P^{PST}(E_T) = \int_0^{nh\nu - E_T - D_0} \sum_{J_A}^{J_A^{max}} \sum_{J_B}^{J_B^{max}} \rho_V(E_V) \cdot N_R(J_A, J_B) \cdot \delta(nh\nu - E_T - E_V - E_R - D_0) \cdot dE_V \qquad (5)$$

Here D_0 and $nh\nu$ (we assume n=2 in modeling the multiphoton component) are dissociation energies of C_n and total energy, respectively. The energy for product vibrational (V) and rotational (R) degree of freedom are denoted by $E_{V,R}$ and the density of state for vibrational (V) degree of freedom is denoted by ρ_V. In equation (5), $N_R(J_A,J_B)$ represents the number of possible combinations of $\mathbf{J_A}$ and $\mathbf{J_B}$ which satisfy equations (3) and (4), weighted by a Boltzmann distribution for J_{AB} (see Eq. 9 below).

Using energy conservation the maximum rotational angular momenta of the fragments can be obtained:

$$J_A^{max} = [\,(nh\nu - D_0 - E_T - E_V)/B_A + 0.25]^{1/2} - 0.5 \qquad (6)$$

$$J_B^{max} = [\,(nh\nu - D_0 - E_T - E_R^A - E_V)/B_B + 0.25]^{1/2} - 0.5 \qquad (7)$$

$$E_R^A = B_A * J_A * (J_A + 1) \qquad (8)$$

J_A^{max} and J_B^{max} are the maximum angular momenta of fragment A with E_T and E_V specified, and of fragment B with E_T, E_V and E_R^A (rotational energy of fragment A with $\mathbf{J}_A$) specified, while B_A and B_B are the rotational constants of fragments A and B.

The vibrational density of states, $\rho_V(E_V)$, is calculated for all energetically allowed vibrational levels within the harmonic oscillator approximation, using the Beyer-Swinehart algorithm[57] and the vibrational frequencies summarized in Table 2. $N_R(J_A, J_B)$, is calculated using:[56]

$$N_R(J_A, J_B) = \sum_{J_{AB}} \sum_{J=|J_{AB}-J_A|}^{J_{AB}+J_A} N_S(J_B, J) \cdot P_{Bolt}(J_{AB}) \qquad (9)$$

for which

$$N_S(J_B, J) = 0 \qquad l_{max} \leq |J_B - J|$$

$$= l_{max} - |J_B - J| + 1 \qquad |J_B - J| < l_{max} < J_B + J$$

$$= J_B + J - |J_B - J| + 1 \qquad l_{max} \geq J_B + J$$

$$P_{Bolt}(J_{AB}) = g_{J_{AB}} \cdot \exp(-B_{AB} \cdot J_{AB} \cdot (J_{AB}+1)/k_B T) / Q_{J_{AB}}$$

Here $N_S(J_B,J)$ is the number of product rotational states with J_A, J_B, and J_{AB} specified, T is the rotational temperature of AB, and P_{Bolt} is the population of state J_{AB}. The rotational temperature of our beam is estimated to be 50 K. At selected energies, we found essentially no difference in $P^{PST}(E_T)$ distributions calculated at T=50 K or T=0 K (J_{AB}=0), so the latter condition was assumed for all calculations reported below.

Table 2: Constants for PST calculations. (cm^{-1})

	Vibrational frequencies [a]	Rotational constant [a]
C_2	1854	1.8198
C_3	1227,2040,63[b]	0.4305

[a] Most of vibrational frequencies from Ref. 19.
[b] Degenerate vibrational modes.

To compare the PST distributions with experiment, the calculated distributions were convoluted with a Monte Carlo simulation program[49,50] which simulates all the apparatus parameters, including the ion/radical beam angular and velocity distribution, the finite interaction volumes, the resolution of the time and position detector, the size of the beam block, and the area of the two-particle detector. It became apparent by inspection that the multiphoton component of the $P(E_T)$ distributions could *not* be fit by PST. The calculated distributions extended to much higher translational energies than the experimental distributions, even assuming only two photons were absorbed. Therefore, since this component appears independent of the photon energy, we simply added the one-photon distribution calculated via PST at a particular photon energy to the experimental multiphoton distribution obtained at a photon energy where no one-photon dissociation was observed; this hybrid distribution could then be directly compared to the experimental distribution.

To find the best one-photon PST distribution which can properly describe the experimental data, C_0 and D_0 in equations (4) and (5) are used as variable parameters. Varying C_0 from 10 to 100 eV·Å^6 yielded only small changes in the calculated

distributions. The value of 10 eV·Å^6, a reasonable number for species in this size range,[58] was chosen for all calculations. The calculated distributions were more sensitive to the dissociation energy (D_0), for which optimal values are given in Table 3 along with those obtained previously by Gingerich.[33-35]

Table 3: Measured bond dissociation energies for carbon clusters.

Photofragmentation Channel	Bond dissociation Energies / eV	
	PST calculation, this work	Gingerich *et al.*[34,35]
$C_4 \rightarrow C + C_3$	4.71 ± 0.20	5.08 ± 0.21
$C_5 \rightarrow C_2 + C_3$	5.96 ± 0.20	5.88 ± 0.23
$C_6 \rightarrow C_3 + C_3$	3.32 ± 0.20	3.63 ± 0.27

Calculated and experimental P(E_T) distributions are compared in Figures 6, 7 (upper panel), and 8 for dissociation of C_4, C_5, and C_6, respectively. Each figure shows the assumed multi-photon distribution, the Monte Carlo convoluted PST distribution, and the sum of the two. We find excellent agreement for the C_4 and C_5 distributions, and for C_6 at the two lower photolysis energies shown in Figure 8.

The agreement between experimental and simulated P(E_T) distributions using dissociation energies similar to those obtained by Gingerich[34,35] supports our statistical hypothesis for the one-photon component of the distributions. However, for C_6 dissociation at $h\nu \geq 4.28$ eV, the one-photon component of the experimental P(E_T) distributions clearly peaks at nonzero E_T, and this is not reproduced by the PST

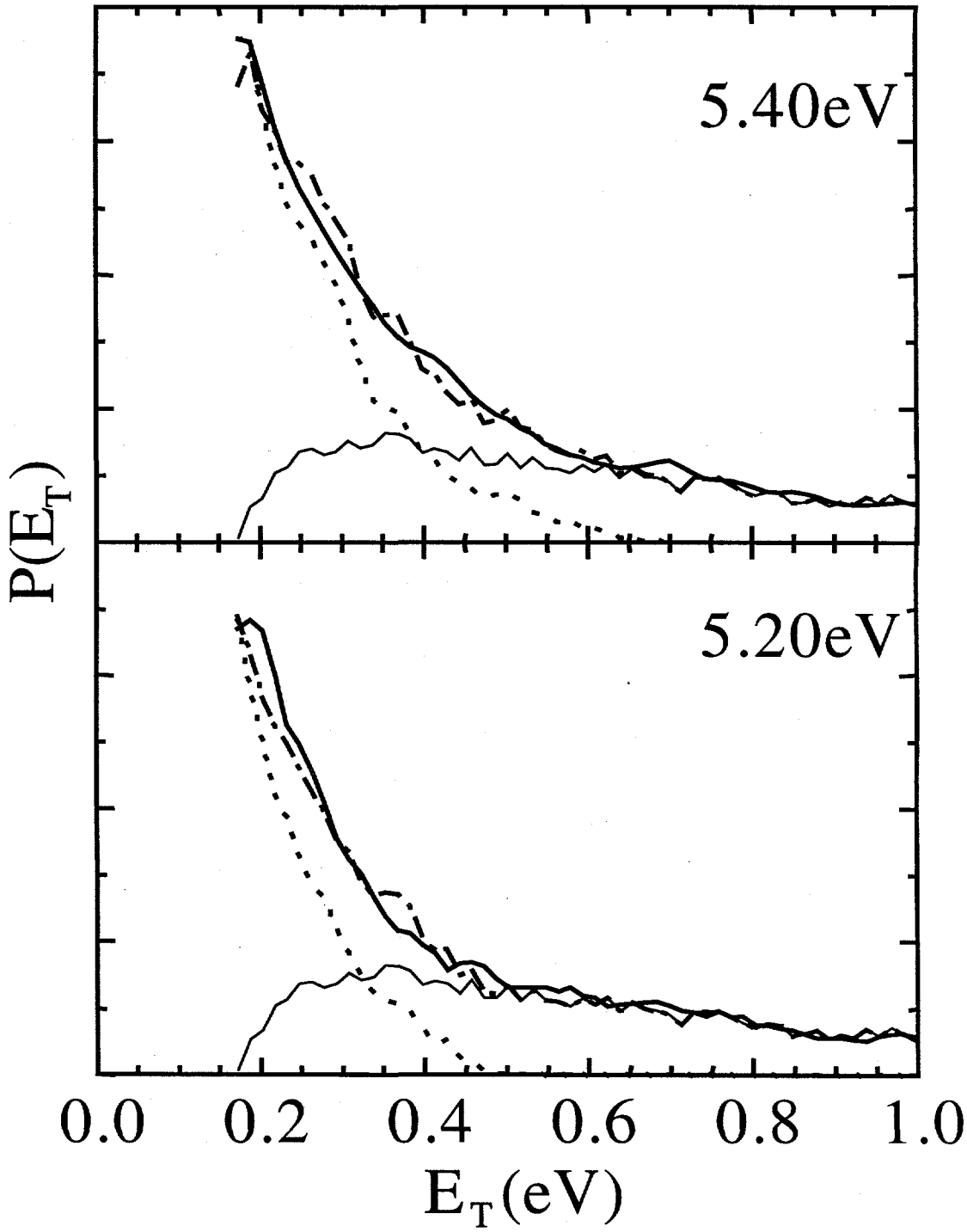

Figure 6. Comparison of experimental $P(E_T)$ distributions to calculated PST distributions for unimolecular dissociation of the C_4 into C_3 + C products. The assumed multi-photon distribution (thin solid line), the Monte-Carlo convoluted PST distribution (dotted line), and the sum of two (dash-dotted line) are plotted with the experimental $P(E_T)$ distribution (thick solid line).

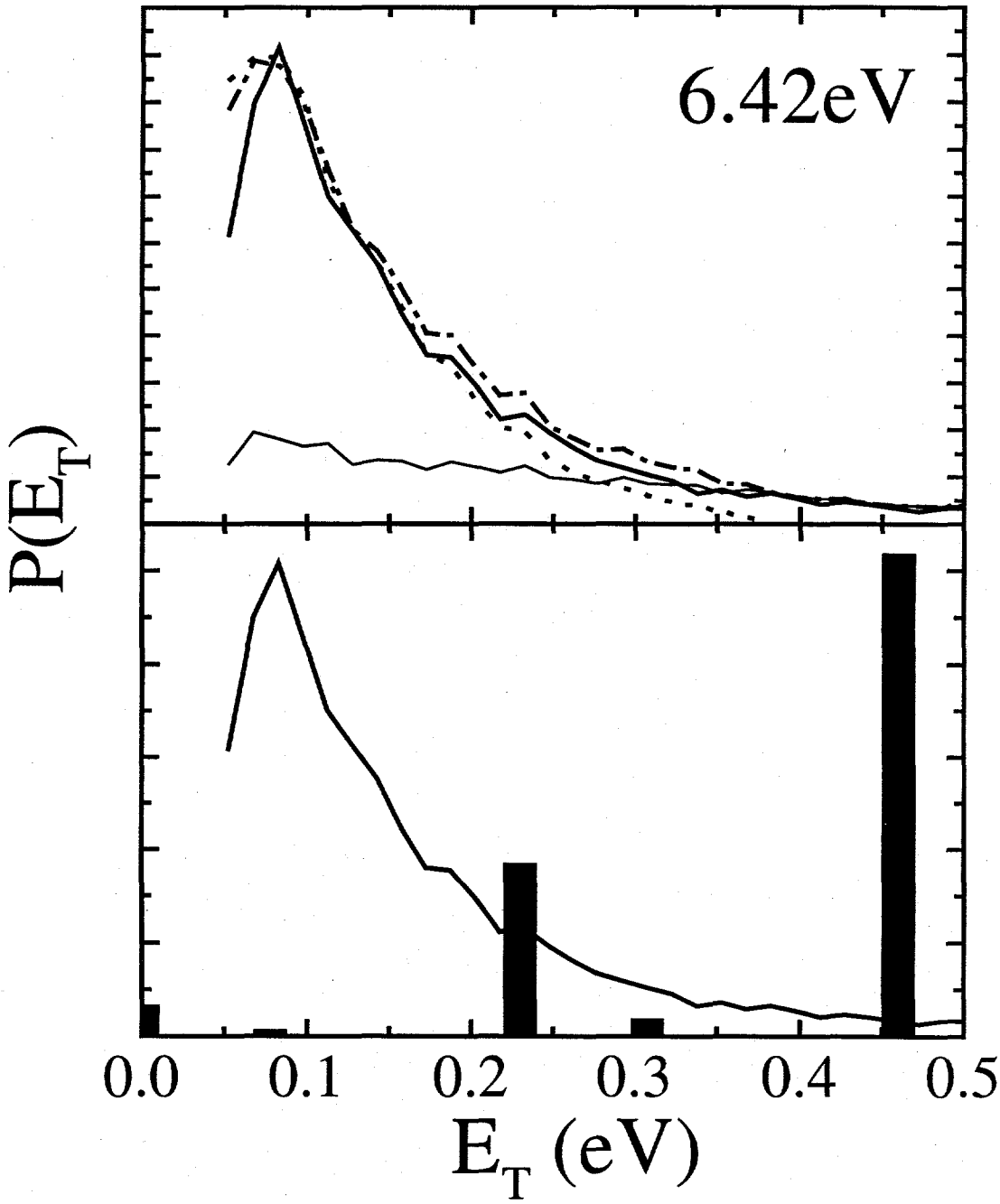

Figure 7. Comparison of experimental $P(E_T)$ distribution for unimolecular dissociation of C_5 into $C_3 + C_2$ products at 6.42eV to calculated PST distribution (upper panel) and Franck-Condon (FC) vibrational distribution (lower panel). In the upper panel, the assumed multi-photon distribution (thin solid line), the Monte-Carlo convoluted PST distribution (dotted line), and the sum of two (dash-dotted line) are plotted with the experimental $P(E_T)$ distribution (thick solid line). In the lower panel, the results of the FC model are histogrammed since only widely spaced C_2 and C_3 stretching vibrational levels are populated.

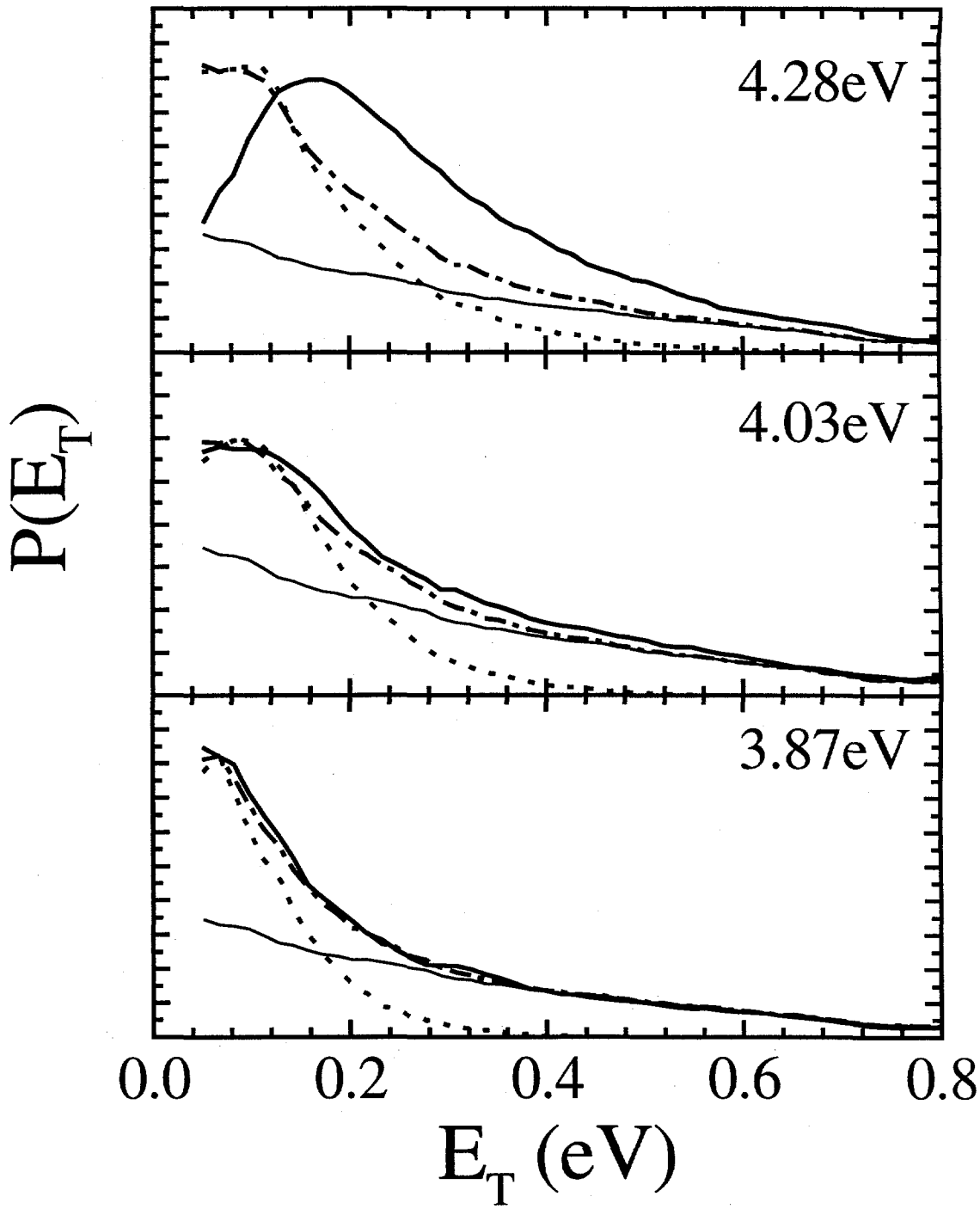

Figure 8. Comparison of experimental $P(E_T)$ distributions to calculated PST distributions for unimolecular dissociation of the C_6 into $C_3 + C_3$ products. The assumed multi-photon distribution (thin solid line), the Monte-Carlo convoluted PST distribution (dotted line), and the sum of two (dash-dotted line) are plotted with the experimental $P(E_T)$ distribution (thick solid line).

distribution as shown in the upper panel of Fig. 8. This disagreement may reflect ground state dissociation that is too fast for a statistical model to be applicable. It is also possible that the dissociation dynamics are fundamentally different for C_6 at these higher energies, involving, for example, a potential energy surface with a significant barrier.

Although our results are generally consistent with statistical dissociation on the ground state, one might ask if there are excited state dissociation mechanisms that would produce similar translational energy distributions peaking at low E_T and showing little variation with photon energy. One simple mechanism of this type is the Franck-Condon model,[59] applicable for rapid dissociation on a repulsive excited state surface, in which the product vibrational distribution is given by a Franck-Condon projection of the reactant geometry onto the product vibrational states. Results are given in the lower panel of Figure 7 for photodissociation of C_5; the primary Franck-Condon activity is in the C_2 stretch. Clearly, this distribution peaks at higher E_T than the experimental and statistical distributions (assuming the same bond dissociation energy). Note that any relaxation of the Franck-Condon vibrational distribution due to dynamics on the excited state surface is likely to increase the fraction of available energy appearing as product translation, resulting in even poorer agreement with the experimental and statistical distributions.

V. DISCUSSION

The principal results from the photodissociation of linear carbon clusters are summarized as follows:

(i) The photofragment yield cross-sections consist of several continua spanning the whole visible and ultraviolet region.

(ii) Product branching ratios for dissociation of mass-selected carbon C_n clusters are dominated by the $C_3 + C_{n-3}$ channel, although some minor channels are also identified for dissociation of C_4 and C_5 clusters.

(iii) Analysis of the photofragment translational energy $P(E_T)$ distributions above the dissociation threshold comprise of single- and multi-photon contributions, confirming that these two processes compete.

(iv) Single photon dissociation near threshold result in $P(E_T)$ distributions which are consistent with calculated PST distributions, i.e., the product state distributions are statistical. This implies that dissociation occurs on the ground state potential energy surface, and that no barriers are present along the dissociation coordinates.

(v) Multi-photon dissociation results in structureless $P(E_T)$ distributions extending to high E_T which show no change with increasing photon energy.

The agreement between the single photon distributions and PST predictions indicates that there are no significant barriers present along the minimum energy pathway from the ground state minimum to dissociation asymptotes. Linear C_4 and

C_6 have $\tilde{X}\,^3\Sigma_g^-$ ground states, while C_5 has a $\tilde{X}\,^1\Sigma_g^+$ ground state. For C_4 and C_5, the ground state surfaces adiabatically correlate with ground state products, i.e., $C(^3P)$ + $C_3(X\,^1\Sigma_g^+)$ and $C_2(X\,^1\Sigma_g^+)$ + $C_3(\tilde{X}\,^1\Sigma_g^+)$, so the absence of an exit barrier for ground state dissociation is not unexpected. However, the ground state of C_6 correlates to the $C_3(\tilde{X}\,^1\Sigma_g^+)$ + $C_3(\tilde{a}\,^3\Pi_u)$ excited state asymptote, whereas dissociation to the lowest energy $C_3(\tilde{X}\,^1\Sigma_g^+)$ + $C_3(\tilde{X}\,^1\Sigma_g^+)$ channel is spin-forbidden. The $C_3(\tilde{a}\,^3\Pi_u)$ state lies 2.12 eV above the $C_3(\tilde{X}\,^1\Sigma_g^+)$ state, and it is extremely unlikely that the one photon distributions in Figure 5 are due to the triplet product channel since this would imply a bond dissociation energy of 1.2 eV for C_6.

The $C_3(\tilde{X}\,^1\Sigma_g^+)$ + $C_3(\tilde{X}\,^1\Sigma_g^+)$ channel can only result from intersystem crossing (ISC) to a low lying singlet surface. The $\tilde{b}\,^1\Sigma_g^+$ state is the lowest singlet state that correlates adiabatically to this channel. Liang *et al.*[60] calculate the $\tilde{b}\,^1\Sigma_g^+$ to lie only 0.16 eV above the $\tilde{X}\,^3\Sigma_g^-$ ground state, while the C_6^- photoelectron spectrum[16] indicates this splitting is around 0.25 eV. In any case, there will be a curve-crossing between the two states below the dissociation energy. In addition, at the excitation energies in Fig. 6 (3.2 eV and higher), the density of vibrational levels in the two C_6 electronic states is quite high ($>10^{10}/cm^{-1}$), so that each triplet vibrational level will be nearly degenerate with a singlet level. Since even a small spin-orbit interaction can result in strong mixing of nearly degenerate singlet and triplet levels, ISC between the two states should be reasonably rapid, consistent with our $P(E_T)$ distributions for C_6 dissociation. We point out that equal mass (i.e. C_3+C_3) channel has the most favorable mass

combination for detection. As a result, fragments with E_T as low as 0.050 eV can be detected (see Fig. 5), so we would be particuarly sensitive to an exit barrier for dissociation of C_6.

The facile multi-photon absorption and dissociation observed for these carbon clusters is similar to that seen in carbon clusters cations (C_n^+), as discussed by Sowa *et al.*[47] In both cases, this phenomenon is likely related to a rather large number of low-lying electronic states for these species. For example, nine electronically excited states, three of which are singlets, are calculated to lie within 3 eV of the ground state in C_5,[28] and the photoelectron spectra of C_4^-, C_5^-, and C_6^- all show transitions to numerous low-lying electronic states of the neutral.[14,16] While transitions to many of these excited states from the neutral ground states are optically forbidden, Maier[21] does observe several weak transitions in his matrix absorption spectra of neutral carbon clusters that are assigned to forbidden transitions allowed by vibronic coupling, including the band that we also observe in Figure 2. Our observation of a finite and essentially continuous photofragment yield across much of the visible and ultraviolet suggests that a combination of vibronic and possibly spin-orbit coupling results in a small but finite oscillator strength for absorption of one photon over a broad energy range, followed by absorption of a second photon and dissociation.

There are two limits for the mechanism of subsequent photon absorption. One is that the excited state generated by the first photon absorbs a second photon before undergoing any significant relaxation. This results in a state with electronic energy 2hν, which could either dissociate or absorb another photon; we did observe nonzero PFY

signal at photon energies which would require three-photon absorption to dissociate. Given that there appears to be a resonant (if weak) transition available from the ground state over a wide energy range, it would not be too surprising if a similar condition held for the one-photon excited state.

Alternatively, absorption of each photon could be followed by internal conversion back to the ground state prior to absorption of the next photon. Thus, electronic energy is converted into vibrational energy on the ground state surface before a second photon is absorbed, and this process continues until $nh\nu > D_0$. This model is more consistent with the single-photon dynamics seen here; if IC to the ground state dominates just above the dissociation threshold, then it is likely to dominate below the threshold too. It is similar to the mechanism we have proposed for resonant multi-photon detachment of carbon cluster anions.[61] However, as discussed in Section IV, the multiphoton $P(E_T)$ distributions appear to be non-statistical. Thus, it is not clear if absorption of the last photon would be followed by internal conversion and then dissociation on the ground state, or by excited state dissociation. Non-statistical dissociation on the ground state could occur if the total energy is so high that dissociation is faster than energy randomization; this situation could certainly arise in the case of multi-photon absorption, yielding total energies well in excess of the bond dissociation energy.

VI. CONCLUSIONS

We have employed the technique of fast radical beam photofragment translational

spectroscopy to study the photodissociation of mass-selected linear carbon clusters C_n (n = 4 – 6), and measured the photofragment yield cross-section, product branching ratios, and $P(E_T)$ distributions. The results and analysis indicate somewhat surprising photophysics for these clusters, as they appear to absorb light and dissociate over a wide range of visible and ultraviolet wavelengths. Multi-photon absorption and dissociation occurs at photon energies below the dissociation threshold, while both single and multi-photon dissociation occur above threshold. The single-photon mechanism appears to involve rapid internal conversion to the ground state followed by dissociation primarily to the lowest energy $C_3 + C_{n-3}$ channel.

Our results, particularly the observation of dissociation at photon energies well below the bond dissociation energy, suggest an unprecedented level of electronic and vibrational state mixing for species in this size regime. We attribute this to the large number of low-lying electronic states in carbon clusters, along with the high density of vibrational levels arising from the low frequency bends in these species. It would be of considerable interest to attempt to track the energy flow subsequent to electronic excitation in these clusters in order to assess the role of the low-lying electronic states. The dominance of ground state dissociation in our experiments indicate that nanosecond lasers are too slow for doing this, but femtosecond pump-probe measurements based on either ionization or photoelectron detection may provide significantly more insight into the detailed intramolecular dynamics of these species.

Acknowledgments:

This research is supported by the Director, Office of Energy Research, Office of Basic Energy Sciences, Chemical Sciences Division of the US Department of Energy under Contract No. DE-AC03-76SF00098.

References:

[1] P. Gerhardt, S. Loffler, and K. H. Homann, Chem. Phys. Lett. **137,** 306 (1987).

[2] J. H. Goebel, J. D. Bregman, D. W. Strecker, F. C. Witteborn, and E. F. Erckson, Astrophys. J. **222,** L129 (1978).

[3] K. H. Hinkle, J. J. Keady, and P. F. Bernath, Science **241,** 1319 (1988).

[4] P. F. Bernath, K. H. Hinkle, and J. J. Keady, Science **244,** 562 (1989).

[5] H. W. Kroto, J. R. Heath, S. C. O'Brien, R. F. Curl, and R. E. Smalley, Astrophys. J. **314,** 352 (1987).

[6] G. von Helden, M.-T. Hsu, N. Gotts, and M. T. Bower, J. Phys. Chem. **97,** 8182 (1993).

[7] A. L. Alexandrov and V. A. Schweigert, Chem. Phys. Lett. **263,** 551 (1996).

[8] L. B. Ebert, Science **247,** 1468 (1990).

[9] K. S. Pitzer and E. Clementi, J. Am. Chem. Soc. **81,** 4477 (1959).

[10] W. Weltner and R. Van Zee, Chem. Rev. **89,** 1713 (1989).

[11] A. Van Orden and R. J. Saykally, Chem. Rev. **98,** 2313 (1998).

[12] G. von Helden, M. T. Hsu, N. G. Gotts, P. R. Kemper, and M. T. Bowers, Chem. Phys. Lett. **204,** 15 (1993).

[13] M. T. Bowers, P. R. Kemper, G. von Helden, and P. van Koppen, Science **260,** 1446 (1993).

[14] S. H. Yang, K. J. Taylor, M. J. Craycraft, J. Conceicao, C. L. Pettiette, O. Cheshnovsky, and R. E. Smalley, Chem. Phys. Lett. **144,** 431 (1988).

[15] D. W. Arnold, S. E. Bradforth, T. N. Kitsopoulos, and D. M. Neumark, J. Chem. Phys.

95, 8753 (1991).

[16] C. Xu, G. R. Burton, T. R. Taylor, and D. M. Neumark, J. Chem. Phys. **107,** 3428 (1997).

[17] A. E. Douglas, Nature **269,** 130 (1977).

[18] J. Fulara, D. Lessen, P. Freivogel, and J. P. Maier, Nature **366,** 439 (1993).

[19] P. Freivogel, M. Grutter, D. Forney, and J. P. Maier, Chem. Phys. Lett. **249,** 191 (1996).

[20] P. Freivogel, J. Fulara, M. Jakoi, D. Forney, and J. P. Maier, J. Chem. Phys. **103,** 54 (1995).

[21] D. Forney, P. Freivogel, M. Grutter, and J. P. Maier, J. Chem. Phys. **104,** 4954 (1996).

[22] D. Forney, J. Fulara, P. Freivogel, M. Jakoi, D. Lessen, and J. P. Maier, J. Chem. Phys. **103,** 48 (1995).

[23] J. M. L. Martin, J. P. Francois, and R. Gijbels, J. Chem. Phys. **93,** 8850 (1990).

[24] J. M. L. Martin, J. P. Francois, and R. Gijbels, J. Chem. Phys. **94,** 3753 (1991).

[25] J. M. L. Martin, J. P. Francois, and R. Gijbels, J. Comput. Chem. **12,** 52 (1991).

[26] V. Parasuk and J. Almlof, J. Chem. Phys. **91,** 1137 (1989).

[27] V. Parasuk and J. Almlof, J. Chem. Phys. **94,** 8172 (1991).

[28] M. Kolbuszewski, J. Chem. Phys. **102,** 3679 (1995).

[29] J. Drowart, R. P. Burns, G. DeMarie, and M. G. Inghram, J. Chem. Phys. **31,** 1131 (1959).

[30] L. Gausset, G. Herzberg, A. Lagerquist, and B. Rosen, Disc. Faraday Soc. **35,** 1131 (1963).

[31] H. L. Strauss and E. Thiele, J. Chem. Phys. **46,** 2473 (1967).

[32] M. W. Chase Jr., C. A. Davies, J. R. Downey Jr., D. J. Fruip, R. A. McDonald, and A. N. Syverud, *JANAF Thermochemical Tables, 3rd Ed., J. Chem. Phys. Ref. Data 14, Suppl. No. 1.* (1985).

[33] K. A. Gingerich, Chem. Phys. Lett. **196,** 245 (1992).

[34] K. A. Gingerich, H. C. Finkbeiner, and W. Schmude Jr., Chem. Phys. Lett. **207,** 23 (1993).

[35] K. A. Gingerich, H. C. Finkbeiner, and W. Schmude Jr., J. Am. Chem. Soc. **116,** 3884 (1994).

[36] J. M. L. Martin, J. P. Francois, and R. Gijbels, J. Chem. Phys. **90,** 3403 (1989).

[37] K. Raghavachari, R. A. Whiteside, and J. A. Pople, J. Chem. Phys. **85,** 6623 (1986).

[38] K. Raghavachari and J. S. Binkley, J. Chem. Phys. **87,** 2191 (1987).

[39] J. D. Watts, J. Gauss, J. F. Stanton, and R. J. Bartlett, J. Chem. Phys. **97,** 8372 (1992).

[40] J. Szczepanski, S. Ekern, and M. Vala, J. Phys. Chem. **101,** 1841 (1997).

[41] Z. Slanina, Chem. Phys. Lett. (1987).

[42] M. J. Deluca and M. A. Johnson, Chem. Phys. Lett. **152,** 67 (1988).

[43] B. Pozniak and R. C. Dunbar, Int. J. Mass Spec. and Ion Proc. **133,** 97 (1994).

[44] M. E. Geusic, T. J. McIlrath, M. F. Jarrold, L. A. Bloomfield, R. R. Freeman, and W. L. Brown, J. Chem. Phys, **84,** 2421 (1986).

[45] P. P. Radi, T. Bunn, P. R. Kemper, M. Molchan, and M. T. Bower, J. Chem. Phys. **88,** 2809 (1988).

[46] K. B. Schelimov, J. M. Hunter, and M. F. Jarrold, Int. J. Mass Spectrom. Ion Processes

138, 17 (1994).

[47] M. B. Sowa, P. A. Hintz, and S. L. Anderson, J. Chem. Phys. **95,** 4719 (1991).

[48] M. B. Sowa-Resat, P. A. Hintz, and S. L. Anderson, J. Phys. Chem. **99,** 10736 (1995).

[49] R. E. Continetti, D. R. Cyr, D. L. Osborn, D. J. Leahy, and D. M. Neumark, J. Chem. Phys. **99,** 2616 (1993).

[50] R. E. Continetti, D. R. Cyr, R. B. Metz, and D. M. Neumark, Chem. Phys. Lett. **182,** 406 (1991).

[51] D. L. Osborn, D. J. Leahy, D. R. Cyr, and D. M. Neumark, J. Chem. Phys. **104,** 5026 (1996).

[52] J. M. B. Bakker, J. Phys. E **6,** 785 (1973).

[53] T. N. Kitsopoulos, C. J. Chick, Y. Zhao, and D. M. Neumark, J. Chem. Phys. **95,** 5479 (1991).

[54] C. C. Arnold, Y. X. Zhao, T. N. Kitsopoulos, and D. M. Neumark, J. Chem. Phys. **97,** 6121 (1992).

[55] P. Pechukas and J. C. Light, J. Chem. Phys. **42,** 3281 (1965).

[56] P. Pechukas, J. C. Light, and C. Rankin, J. Chem. Phys. **44,** 794 (1966).

[57] P. J. Robinson and K. A. Holbrook, *Unimolecular reactions* (Wiley-Interscience, New York, 1972).

[58] V. Aquilanti, D. Cappellitti, V. Lorent, E. Luzzatti, and F. Pirani, J. Phys. Chem. **97,** 2063 (1993).

[59] R. Schinke, *Photodissociation dynamics* (Cambridge University Press, New York, 1993).

[60] C. Liang and H. F. Schaeffer III, Chem. Phys. Lett. **169,** 150 (1990).

[61] Y. Zhao, E. de Beer, C. Xu, T. Taylor, and D. M. Neumark, J. Chem. Phys **105,** 4905 (1996).

Chapter 5. Photodissociation Dynamics of Triiodide anion (I_3^-)

Abstract

We have investigated the spectroscopy and dissociation dynamics of I_3^- in the range of 390-290nm, utilizing the method of fast beam photofragment translational spectroscopy. This paper reports the photofragment yield (PFY) spectrum of I_3^- in the gas phase, consisting of two absorption bands that correspond to the bands seen in solution. Two product mass ratios from the photodissociation of I_3^- are observed: 1:2 and 1:1 mass ratios. The $P(E_T)$ distribution with 1:2 mass ratio from the photodissociation of I_3^- shows that electronic transitions to those two absorption bands produce the I_2^- ($\tilde{X}$) and either spin-orbit ground or excited state of I. Based on our detection scheme, the product channel with 1:1 mass ratio is assigned to symmetric three-body dissociation.

I. Introduction

The triiodide ion, I_3^-, is a well known chemical species with unusual properties. It is one of the classic examples of a molecule that violates the octet rule. It is also one of relatively few closed-shell negative ions that has excited electronic states below its electron detachment threshold. During the last several years, there has been considerable interest in the time-resolved photodissociation dynamics of I_3^-. These experiments have been performed in polar solvents and in the gas phase, and yield markedly different results attributed to solvent effects on the short-time reaction dynamics. A better understanding of these effects requires more detailed information on the gas phase and solutions phase dynamics. In this paper, we present a frequency domain study of gas phase I_3^- photodissociation using fast beam photofragment translational spectroscopy.

The spectroscopy of triiodide ion (I_3^-) has been extensively studied in the condensed phase. Its absorption spectrum consists of two broad bands centered at 290 and 360 nm,[1-7] henceforth referred to as the upper and lower bands. The assignment of these two bands has proved controversial. Based on a semiempirical molecular orbital calculation with 5p orbitals of iodine atoms, the molecular term symbol for the ground state of I_3^- was obtained by Gabes *et al*[2,8]:

$$\tilde{X}\ ^1\Sigma_g^+ : \ldots\ldots(\sigma_u)^2(\pi_u)^4(\sigma_g)^2(\pi_g)^4(\pi_u^*)^4(\sigma_u^*)^0$$

From this, the two absorption bands of I_3^- were assigned to the $\sigma_g \rightarrow \sigma_u^*$ and $\pi_g \rightarrow \sigma_u^*$ transitions by Gabes *et al.*[2,8], while Mizuno *et al.*[3] suggested that these two bands were ascribed to the $\sigma_g \rightarrow \sigma_u^*$ transitions split by the spin-orbit coupling. Later, a semiempirical calculation including spin-orbit interaction was performed by Okada *et*

al.,[4] yielding the orbital configuration of the excited states with the order of σ_g and π_g orbitals switched:

$$\tilde{X}\ ^1\Sigma_g^+ : (\sigma_u)^2(\pi_u)^4(\pi_g)^4(\sigma_g)^2(\pi_u^*)^4(\sigma_u^*)^0$$

$$^{1,3}\Pi_g : (\sigma_u)^2(\pi_u)^4(\pi_g)^4(\sigma_g)^2(\pi_u^*)^3(\sigma_u^*)^1$$

$$^{1,3}\Sigma_u^+ : (\sigma_u)^2(\pi_u)^4(\pi_g)^4(\sigma_g)^1(\pi_u^*)^4(\sigma_u^*)^1$$

$$^{1,3}\Pi_u : (\sigma_u)^2(\pi_u)^4(\pi_g)^3(\sigma_g)^2(\pi_u^*)^4(\sigma_u^*)^1$$

Okada *et al.* assigned the two bands to the transitions to intermixed spin-orbit states between $^3\Pi_{0+u}$ and $^1\Sigma_{0+u}$ states, both of which are 0^+ states in Hund case (c). This assignment was supported by the electronic and magnetic circular dichroism spectra (MCD) of triiodide in solution by Isci and Mason.[7]

Early photodissociation studies of I_3^- in solution have shown that excitation into either band produces diiodide ions (I_2^-) in the ground state.[9,10] The resonance Raman spectrum of I_3^- reveals a long progression of the symmetric stretch, indicating that the initial motion on the excited state is along this coordinate.[5,6,11] Recently, femtosecond time resolved transient absorption was used to study the photodissociation of I_3^- in solution. Banin *et al.*[12-17] observed coherent vibrational motion of I_2^- product anions in their $\tilde{X}\ ^2\Sigma_u^+$ state, following excitation to the upper band at 308nm. This coherent vibrational motion appears as early as 500 fs after the initial excitation, shows an average vibrational state of <v>=12, and is irreversibly lost within 4 ps due to interaction with the solvent molecules. Using the same technique, the quantum yield of photoproduct I_2^- was obtained by Kuhne *et al.*[18-20] They found that the quantum yield of I_2^-, which depends on the excitation energy, is 1 at 400nm (the lower band) and 0.8 at 266nm (the upper band).

Recent experiments have characterized I_3^- in the gas phase. Do *et al.*[21] measured the bond strength of I_3^- through collision-induced dissociation in a tandem mass spectrometer, obtaining a value of 1.31±0.06 eV for dissociation to I_2+I^-. The photoelectron spectrum of I_3^- was taken by Taylor *et al.*[22] and the electron affinity of I_3^- was determined as 4.226±0.013eV (293nm). From these two experiments, one can construct the energy diagram for I_3^- photodissociation shown in Fig. 1.

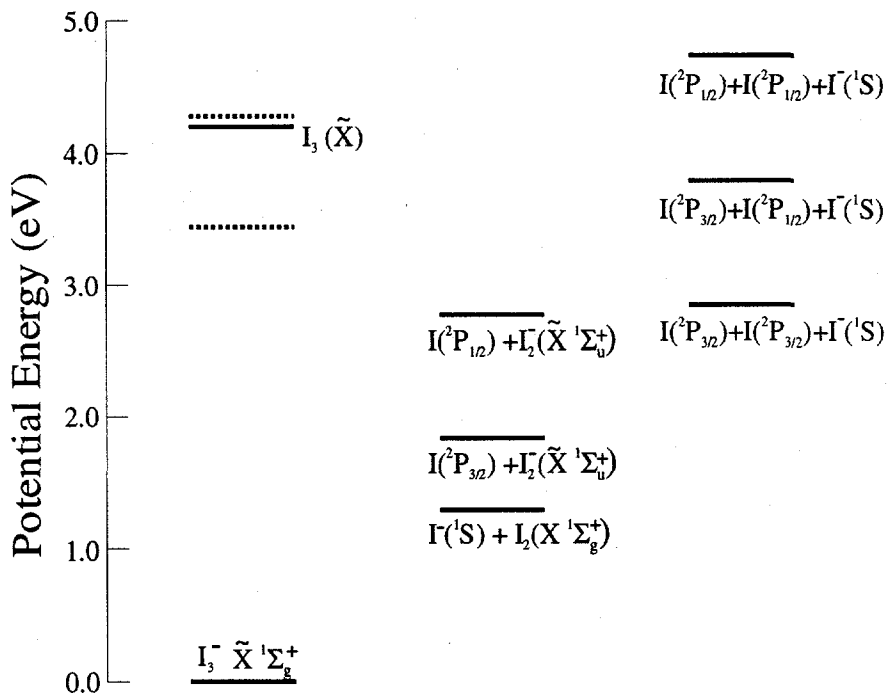

Figure 1 : Energetics of I_3^-. The most intense position of the upper and lower absorption bands for I_3^- are shown in dotted lines.

Recently, Zanni *et al.*[23,24] studied the photodissociation of I_3^- in the gas phase using femtosecond photoelectron spectroscopy (FPES). In this study, I_2^- and I^- were found as photoproducts at 390nm (lower band) with approximate 1:1 yield. In addition,

coherent vibrational motion of $I_2^-(\tilde{X})$ was recorded at a much higher vibrational quantum number (<v>=67) than that in solution. To model the dynamics of this reaction, they used wave packet simulations, which showed significant motionpopulation along the symmetric stretching coordinate 500 fs after the initial excitation. Based on these simulations, the formation of I^- was attributed to the three-body dissociation rather than the lower energy I_2+I^- channel.

The significant differences between the gas phase and solution results suggest a more detailed photodissociation study is needed. Here, we present results using a frequency-resolved technique that is complementary to the FPES work, namely fast beam photofragment translational spectroscopy. We are particularly interested in the following: First, the absorption spectrum of I_3^- in the gas phase has never been taken. Second, the photodissociation processes of I_3^- have not been studied at multiple photon energies. Third, experimental efforts on this reaction have been focused on detecting I_2^-. Therefore, there is no information about the spin-orbit state of I as photoproduct, which prevents us from understanding the correlation between the excited state of I_3^- and photoproduct. Fourth, as pointed out by Zanni *et al.*,[23,24] there are possibilities of three-body dissociation as an alternative dissociation. In this paper, we address these four issues using our fast radical beam photofragment translational spectrometer.

II. Experimental Setup

Photodissociation of the triiodide anions (I_3^-) was studied using our fast beam photofragment spectrometer. In this experiment,[25-27] argon gas (3psig) flows over iodine

crystals (I_2) at room temperature. The resulting mixture supersonically expands through a pulsed valve into the source region of the apparatus. Anions were generated by a 1 keV electron beam, which crosses the expansion, and cooled to 20-50 K during the expansion.

Negative ions formed in the source region are accelerated to 8 keV and separated temporally by a time-of-flight (TOF) mass spectrometer. The I_3^- ion packet is intersected by a linearly polarized excimer-pumped pulsed dye laser beam and some I_3^- ions absorb a photon and dissociate. A blocking strip across the center of detector prevents parent molecules from reaching the detector, whereas photofragments with sufficient recoil energy miss the beam block and strike the detector. These fragments are generally detected with high efficiency (up to 50%) due to their high laboratory kinetic energy.

Two types of experiments are performed to characterize the photodissociation of I_3^-. First, the photofragment yield (PFY) spectrum is obtained by collecting the total flux of fragments as a function of the photodissociation laser wavelength. To investigate the photodissociation dynamics at a fixed wavelength, two photofragments from a parent molecule are collected in coincidence using a time- and position-sensitive detector. In this experiment, we measure the distance R between the two fragments on the detector, the time difference τ of their arrival, and the individual displacements of the two fragments, r_1 and r_2, from the detector center for each dissociation event. From these we obtain the center-of mass translational energy E_T, the scattering angle with respect to laser polarization, θ, and the two photofragment mass ratio m_1/m_2 via

$$\frac{m_1}{m_2} = \frac{r_2}{r_1} \qquad (1)$$

$$\theta = \tan^{-1}\left(\frac{R}{\upsilon_0 \cdot \tau}\right) \qquad (2)$$

$$E_T \cong E_0 \cdot \frac{\mu}{M} \cdot \frac{(\upsilon_0 \cdot \tau)^2 + R^2}{l^2} \qquad (3)$$

Here E_0 and υ_0 are the ion beam energy and velocity, respectively, μ is the reduced mass, and l is the flight length from the photodissociation region to the detector. Although the relative recoil distance R is determined with high precision ($R/\Delta R \approx 100$), the individual recoil distance r_1 and r_2 are less precisely determined due the finite size of the parent beam, resulting in $m/\Delta m \approx 10$. The energy resolution ($\Delta E_T/E_T$) under the conditions in these studies is around 2%.

The dynamics experiment requires that two fragments be detected in coincidence. However, the front of the detector is biased at a high negative potential, such that only neutral fragments can be detected. Although the dissociation of I_3^- yields an ion and a neutral, the experimental conditions are such that the anion fragment is typically neutralized prior to reaching the detector. At all dissociation wavelengths, the I^- and I_2^- products, for which the electron affinities are 3.059[28] and 2.524 eV,[29] can be photodetached by absorption of another photon.

In case of three-body dissociation, photodissociation of I_3^- generate three fragments. However, we detect only two out of three photofragments, the consequence of which will be further discussed in Sect. III.B.

III. Results

A. Photofragment Yield (PFY) Spectrum

The PFY spectrum of I_3 from 416 to 246 nm, shown as the solid line with circles in Fig. 2, was acquired with a step size of 5 nm. Every point was obtained at the same laser power (0.5mJ/mm^2) and the same parent ion density. The whole spectrum is covered by using 11 different dyes.

The PFY spectrum shows two intense features around 360 nm and 290 nm. In the limit that the quantum yield for dissociation is equal to 1, as we expect for gas phase I_3^-, the PFY spectrum is identical to the absorption spectrum. Hence, this is the first absorption spectrum of I_3^- in the gas phase.

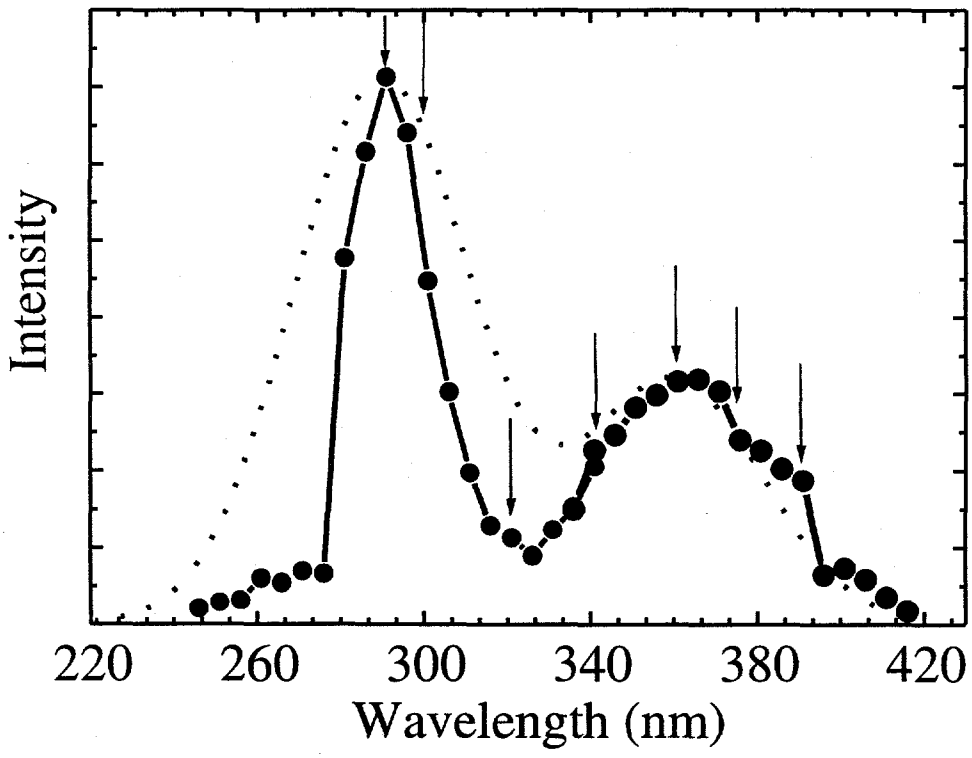

Figure 2 : Photofragment Yield (PFY) spectrum of I_3^-. The solid and circle represents our PFY spectrum in gas phase and the dotted line represents the absorption spectrum in the ethanol.

The PFY spectrum is compared with the absorption spectrum of aqueous I_3^-,[4] shown as a dotted line in Fig. 2. The band maxima agree well, as do the overall band profiles for the lower band. For the upper band, however, the PFY spectrum is much narrower than the absorption spectrum in solution. This difference might be caused by photodetachment of I_3^-, energetically possible below 293nm.[22] On the other hand, the upper band on the PFY spectrum is narrower to the red of the band maximum, too.

B. Photodissociation dynamics of I_3^-

1. Photofragment Mass Ratio (m_1/m_2)

Photodissociation dynamics experiments were performed at selected photon energies marked by arrows in Fig.2. The first information we get from this experiment is the fragment mass ratio, shown in Fig. 3 at 3.87eV (320nm). It is immediately seen that there are two product channels occurring at this photon energy with mass ratios of 1:2 and 1:1. The fragment mass ratio in Fig. 3 shows very broad peaks around 0.5 and 1.0 because of the poor mass resolution ($m/\Delta m \approx 10$). At every photon energy we probed, a similar product mass ratio is obtained.

As shown in Fig. 1, there are several product channels that are thermodynamically feasible following UV excitation of I_3^-:

$I_3^-(\tilde{X}) + h\nu_{photon} \rightarrow$	$I^-(^1S) + I_2(X)$	$D_0 = 1.31 \pm 0.06$ eV	(channel 1)
	$I(^2P_{3/2}) + I_2^-(\tilde{X})$	1.85 ± 0.06 eV	(channel 2)
	$I^*(^2P_{1/2}) + I_2^-(\tilde{X})$	2.79 ± 0.06 eV	(channel 3)
	$I(^2P_{3/2}) + I(^2P_{3/2}) + I^-(^1S)$	2.85 ± 0.06 eV	(channel 4)
	$I(^2P_{3/2}) + I^*(^2P_{1/2}) + I^-(^1S)$	3.80 ± 0.06 eV	(channel 5)

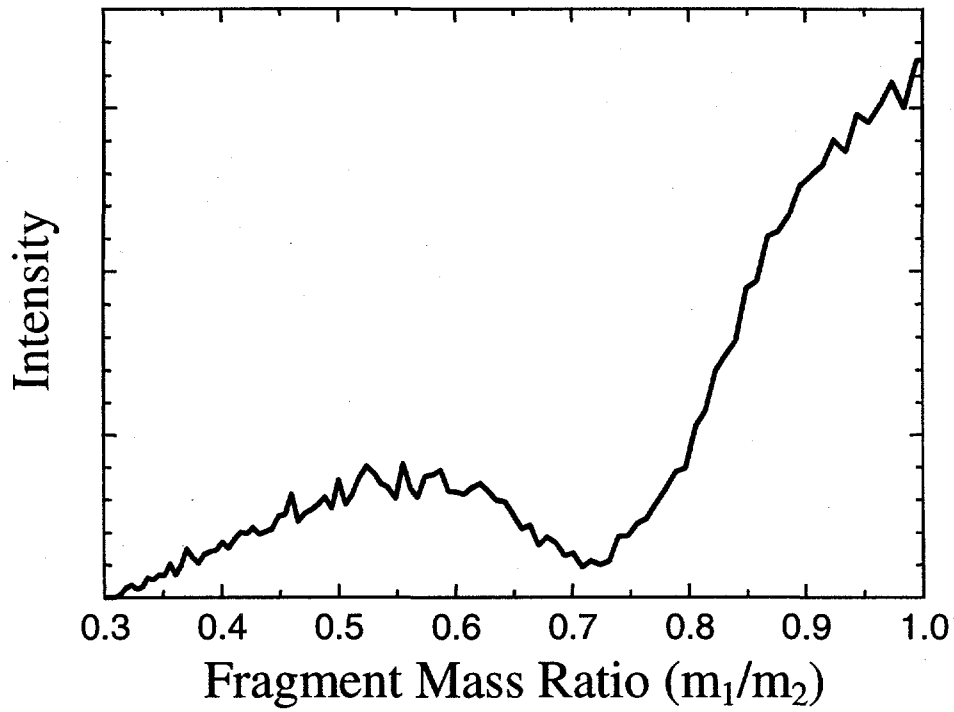

Figure 3 : Photofragment mass ratio (m_1/m_2) of I_3^- at the photon energy of 3.64 eV (341nm).

The energetics are based on the bond strength (1.31 ± 0.06 eV) of I_3^- from the collision-induced dissociation experiment by Do *et al.*[21], the spin-orbit coupling constant for I atom (0.943eV), and the dissociation energies for I_2 (1.542eV)[30] and I_2^- (1.007eV).[29] In addition to the above channels, the low-lying excited states of I_2 (A' $^3\Pi_{2u}$ and A $^3\Pi_{1u}$)[31] and I_2^- ($\tilde{A}$ or $\tilde{A}$' $^2\Pi_g$)[32,33] are also accessible at excitation energies used here. However, we cannot distinguish these I_2 and I_2^- states from vibrationally excited I_2^- in the $\tilde{X}$ state.

Channels 1-3 are two-body dissociation channels that are possible candidates for the products with 1:2 mass ratios, while channels 4-5 are three-body dissociation channels. There are two kinds of three-body dissociation for the triatomic molecules with

$D_{\infty h}$ symmetry: symmetric and asymmetric three-body dissociation. In symmetric three-body dissociation, two identical bond lengths of triatomic molecule increase at approximately the same rate as the dissociation proceeds. In our dynamics experiment, only two photofragments from the parent molecule are collected in coincidence. If the triiodide (I_3^-) anions undergo symmetric three-body dissociation, two end atoms fly apart and the central atom remains stationary in the center of mass frame. Thus, the central atom follows the same trajectory of parent molecule and will hit the beam block in front of detector. As a result, symmetric three-body dissociation of I_3^- can generate the 1:1 mass ratio in our experiment.

For each channel, the joint translational energy and angular distribution is given by

$$P(E_T,\theta) = P(E_T)\cdot(1+\beta(E_T)\cdot P_2(\cos(\theta))) \qquad (4)$$

, in which $\beta(E_T)$ is the anisotropy parameter. For the channel with 1:1 mass ratio, $\mu = 1/2\cdot m_I$ (m_I = mass of I atom) is used in equation (3). The limiting cases of $\sin^2\theta$ and $\cos^2\theta$ angular distribution are given by $\beta = -1$ and $+2$, respectively. Generally speaking, a parallel transition shows a positive β parameter while $\beta<0$ for a perpendicular transition.

Both mass channels show a positive β parameter in agreement with the observation of a parallel transition in (xanthotoxin)·KI_3 crystal by Mizuno *et al.*[3] However, the accurate measurement of the β parameter is hampered because the geometrical constraint of detector allows us to collect photofragments at very restricted angles.

In the following two sections, translational energy P(E_T) distributions with 1:2 and 1:1 mass ratio are presented at selected photon energies.

2. 1:2 mass Channel

P(E_T) distributions for the 1:2 mass channel from I_3^- dissociation are shown in Fig. 4. Those associated with transitions to the lower and the upper bands are shown on the left and right sides of Fig. 4, respectively. The P(E_T) distributions show two main features at every photon energy labeled as A and B in Fig. 4. Both features move toward higher E_T with increasing photon energy.

Channels 1-3 are possibilities for the 1:2 mass channel. With our detection scheme we cannot distinguish between $I^- + I_2$ and $I + I_2^-$ products. However, at all excitation energies studied here, no products are seen at energies above the maximum allowed for channel 2 (rightmost arrows in Fig. 4). We therefore attribute all products in Fig. 4 to channels 2 and 3. The two combs in each plot show the maximum and minimum translational energy for the two channels; at energies below the minimum, the I_2^- internal energy would exceed its bond dissociation energy and it would dissociate long before reaching the detector. Features A and B always fall within the allowed range for channels 2 and 3, respectively, so feature A is assigned to channel 2 and feature B to channel 3. For all excitation energies in the lower band, feature A drops abruptly at the translational energy corresponding to the opening of channel 3.

With these assignments, average internal excitation energies of I_2^- product for both channels ($\langle E_{int} \rangle$) are obtained by

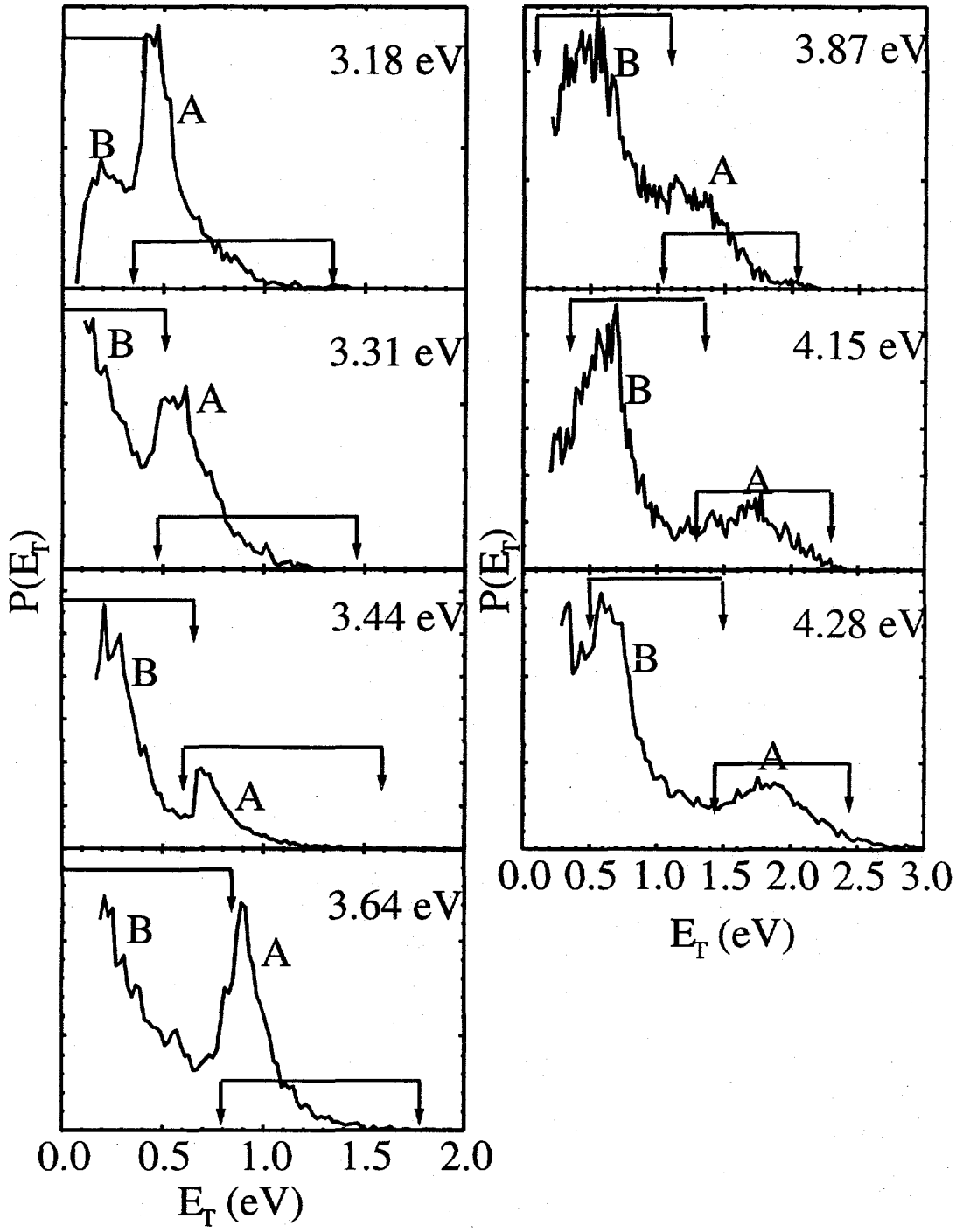

Figure 4 : Translational energy $P(E_T)$ distributions of I_3^- with 1:2 mass ratio at selected photon energies shown at the right upper corner.

$$\langle E_{int}\rangle = h\nu_{photon} - D_0 - \langle E_T\rangle, \qquad (5)$$

where $h\nu_{photon}$ and D_0 are photon energy and dissociation energy for each channel. The average translational energy ($\langle E_T\rangle$) for each channel is obtained by averaging the $P(E_T)$ distribution over the range of I (or I*) + bound I_2^- ($\tilde{X}$).

In photodissociation of I_3^-, the internal excitation energy is the sum of rotational energy and vibrational energy of I_2^- product. If we neglect the rotational excitation in I_2^- photoproduct, the average internal excitation energy ($\langle E_{int}\rangle$) of I_2^- can be converted into an upper bound on $\langle v\rangle$ for I_2^- product using the following equation:

$$\langle E_{int}\rangle = \omega_e\cdot\langle v\rangle - \omega_e\chi_e\cdot(\langle v\rangle + ½)^2 + ¼\cdot\omega_e\chi_e \qquad (6)$$

In the equation (6), the vibrational frequency (ω_e) and anharmonicity ($\omega_e\chi_e$) of I_2^- are 110 and 0.370 cm^{-1}, as determined from the photoelectron spectrum by Zanni *et al.*[29] These values of $\langle E_{int}\rangle$ and $\langle v\rangle$ are summarized in Table 1. In addition, we calculate the branching ratio, channel 2/3, in Table 1. However, the I_2^- ions must be photodetached prior to the detector, as we discussed in Sec. II. Therefore, these values in Table 1 might be distorted by photodetachment efficiency of I_2^- product, which depend on the internal excitation of I_2^-.

The $\langle v\rangle$ values in Table 1 show an interesting trend as a function of photon energy. For channel 3, $\langle v\rangle$ increases with $h\upsilon$ over the full range of excitation energies, while for channel 2, $\langle v\rangle$ is approximately constant throughout the lower band and drops once the upper band is accessed. The branching ratio (channel 2/3) decreases with $h\upsilon$

throughout the lower band mainly due to the increasing range of channel 3 except at 3.64eV, while that remains around 0.3 – 0.4 over the upper band.

Table 1. Summary for 1:2 mass channel

$h\nu_{photon}$	$\langle E_{int} \rangle$ (eV)		$\langle v \rangle$		Branching Ratio
	Channel 2	Channel 3	Channel 2	Channel 3	Channel 2/3
3.18eV	0.79	0.19	79	15	2.62
3.31eV	0.81	0.33	83	27	0.97
3.44eV	0.80	0.39	81	32	0.37
3.64eV	0.82	0.53	84	46	0.72
3.87eV	0.69	0.53	65	46	0.37
4.15eV	0.58	0.68	52	64	0.33
4.28eV	0.58	0.69	52	65	0.41

3. 1:1 mass channel

As we discussed in Sec. III. B., the 1:1 mass channel corresponds to symmetric three-body dissociation. Three-body dissociation of I_3^- generates three atomic photofragments. Thus, all the available energy after the dissociation goes to translational or possible electronic energy of photofragments. The $P(E_T)$ distributions for 1:1 mass channel from I_3^- dissociation in Fig. 5 show sharp peaks along with some small features toward low E_T. The arrows in Fig. 5 indicate the expected E_T in the symmetric three-body

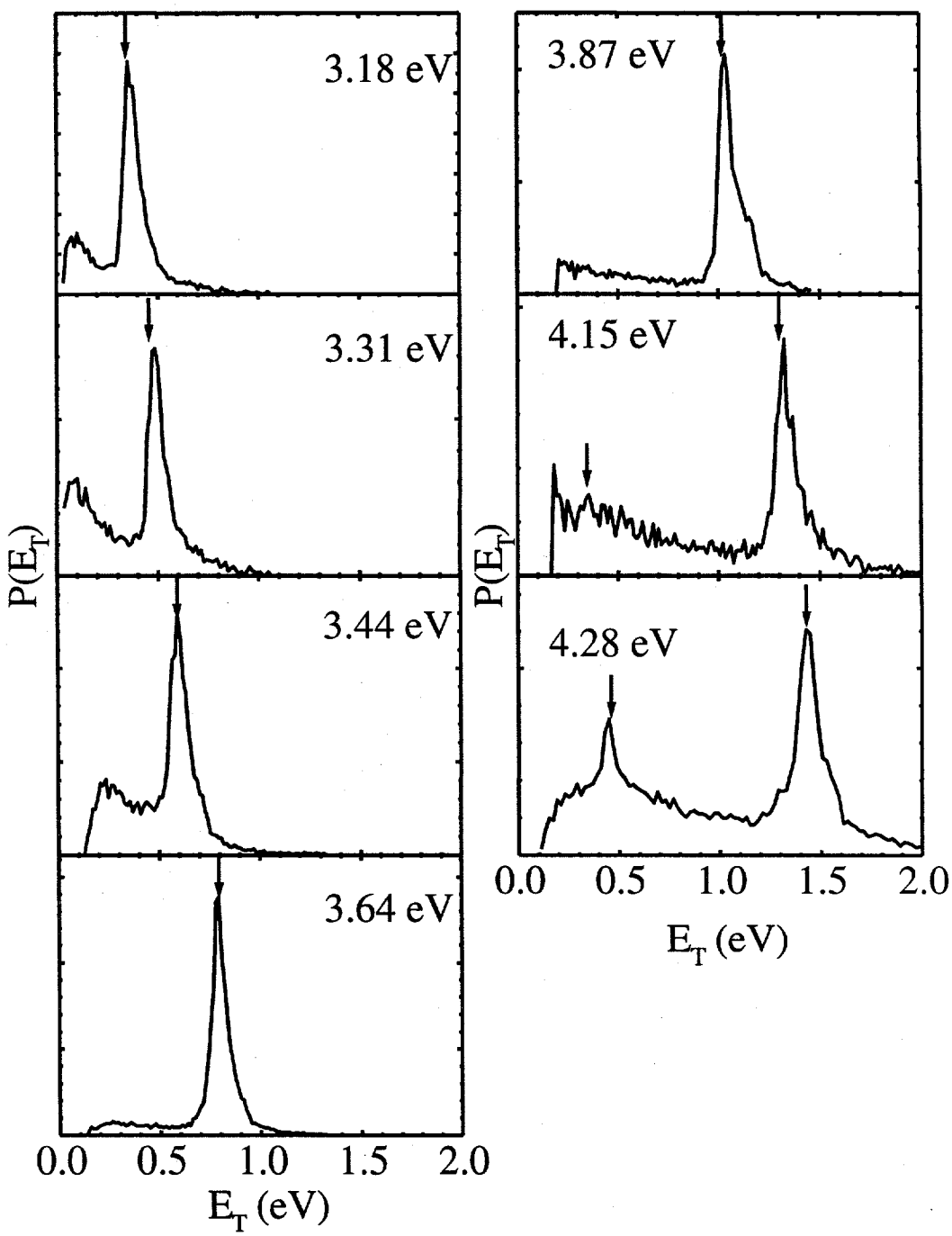

Figure 5 : Translational energy $P(E_T)$ distributions of I_3^- with 1:1 mass ratio at selected photon energies shown at the right upper corner.

dissociation for channels 4 and 5. Positions of sharp features show excellent agreement with arrows, providing further proof that the three-body dissociation is symmetric. Even though channel (5) becomes energetically accessible above 3.80eV, we observe this channel only at 4.28eV, not at 4.15eV.

While the sharp peaks in Fig. 5 correspond to the appropriate kinetic energies for symmetric three-body dissociation, we note that (a) the peaks are considerably broader than the experimental kinetic energy resolution, ~150 meV vs. ~20 meV, and (b) there are broad features in addition to the sharp peaks. The origin of these two aspects of the $P(E_T)$ distributions is considered in the next section.

Finally, we analyze the branching ratio of two-body dissociation versus three-body dissociation in Table 2 by averaging the $P(E_T)$ distribution in Figs. 4 and 5.The production of three-body dissociation decreases in the lower band and increase in the upper band with $h\upsilon$, except at 3.64eV.

Table 2. Summary for I_3^- photodissociation. (unit : %)

$h\nu_{photon}$	1:2 mass channel	1:1 mass channel
3.18eV	47	53
3.31eV	57	43
3.44eV	67	33
3.64eV	55	45
3.87eV	59	41
4.15eV	52	48
4.28eV	45	55

IV. Classical Trajectory calculation for symmetric three-body dissociation of I_3^-

In Sect. III. B. 3, symmetric three-body dissociation of I_3^- is observed. To visualize this process, classical trajectory calculation is performed on the excited state potential energy surface, which was summarized in Table 3. This potential energy surface was previously used for wave packet simulations by Zanni *et al.*[24] Trajectories were computed by standard methods.[34,35] The numerical integration of Hamilton's equations used the sixth-order Gear's method with variable step size. Initial conditions were selected by projecting the zero-point symmetric and asymmetric stretching motion of I_3^- on the ground state surface to excited state surface. Due to Franck-Condon overlap

Table 3. Parameters for the potential energy surface. ($I \overset{r_{ab}}{—} I \overset{r_{bc}}{—} I$)

Ground state potential surface for I_3^-
$V_g(Q_1,Q_3)=\frac{1}{2}\mu_1\omega_1^2(Q_1-Q_{eq})^2+\frac{1}{2}\mu_2\omega_2^2Q_3^{\ 2}$
$Q_1 = r_{ab} + r_{bc}$ $Q_3 = r_{ab} - r_{bc}$
ω_1[a]=112 cm^{-1} ω_2[b]=145 cm^{-1} Q_{eq}=5.358 Å μ_1=63.5 amu μ_3=21.2 amu
Excited state potential surface for I_3^-
$V_e(r_{ab},r_{bc},r_{ac})=\Delta E_0+Q_{ab}+Q_{bc}+Q_{ca}-(J_{ab}^2+J_{bc}^2+J_{ca}^2-J_{ab}J_{bc}-J_{bc}J_{ca}-J_{ca}J_{ab})^{1/2}$
$Q_{\alpha\beta}=\frac{[(1+S_{\alpha\beta})^1E(r_{\alpha\beta})+(1-S_{\alpha\beta})^3E(r_{\alpha\beta})]}{2(1+S_{\alpha\beta})}$ $^1E(r_{\alpha\beta})=D_{\alpha\beta}[1-e^{-\beta_{\alpha\beta}(r_{\alpha\beta}-r_{\alpha\beta}^{eq})}]^2-D_{\alpha\beta}$
$J_{\alpha\beta}=\frac{[(1+S_{\alpha\beta})^1E(r_{\alpha\beta})-(1-S_{\alpha\beta})^3E(r_{\alpha\beta})]}{2(1+S_{\alpha\beta})}$ $^3E(r_{\alpha\beta})=\{D_{\alpha\beta}[1+e^{-\beta_{\alpha\beta}(r_{\alpha\beta}-r_{\alpha\beta}^{eq})}]^2-D_{\alpha\beta}\}/2$
$r_{ab}^{eq}=r_{bc}^{eq}$=3.205 Å $D_{ab}=D_{bc}$=1.014 eV $\beta_{ab}=\beta_{bc}$=1.181 Å^{-1} $S_{ab}=S_{bc}$=0.50
r_{ca}^{eq}=2.983 Å D_{ca}=1.010 eV β_{ca}=1.000 Å^{-1} S_{ca}=0.00
ΔE_0=2.890 eV

between the ground and excited state surface, there is an excitation energy spread in this calculation. Therefore, the direct comparison between trajectory calculation and our experiment, which is performed at fixed excitation energy, is difficult. However, we hope this calculation can give us some idea about three-body dissociation of I_3^-.

A total of 1764 trajectories were run, of which 70 produced three-body dissociation. In some of trajectories for three-body dissociation, distances (r_{ab} and r_{bc} in Table 3) between adjacent I atoms are recorded at each step and plotted in Fig. 6. It shows that three-body dissociation of I_3^- follows a symmetric stretching coordinate until r_{ab} (or r_{bc}) reaches 6Å and spreads along the asymmetric stretching coordinate. None of the trajectories which reach the repulsive walls in the I_2^- product valleys lead to three-body dissociation in this calculation. If we define the asymmetric three-body dissociation as three-body dissociation through I_2^-, there is no asymmetric three-body dissociation observed in trajectory calculation.

As the next step, we extract velocities of three I atoms at the end of trajectory calculation and we use flight time (~31μs) of these atoms in our experiment using the laboratory velocity of parent I_3^- (E_{kin} = 8 keV) and flight length (2m). Then we obtain the position of these I atoms at the detector. Through this process, we can determine what portion of above trajectories can be detected as 1:1 mass channel in our experiment. In Fig. 7, trajectories shown in dotted lines can be detected as 1:1 mass channel. Part of the rest trajectories shown in solid lines can generate three I atoms, all of which can have recoiling energies enough to miss the beam block in front of detector and hit the detector. In this case, only two of three fragments can be detected as 1:1 or 1:2 mass channels at low E_T due to less than 100% detection efficiency of photofragments. Therefore, part of

small feature at low E_T in Fig. 5 can be explained by trajectories in solid lines, while peaks with broader width than our instrumental resolution can be explained by some spread along asymmetric stretching coordinate in trajectories shown in dotted lines.

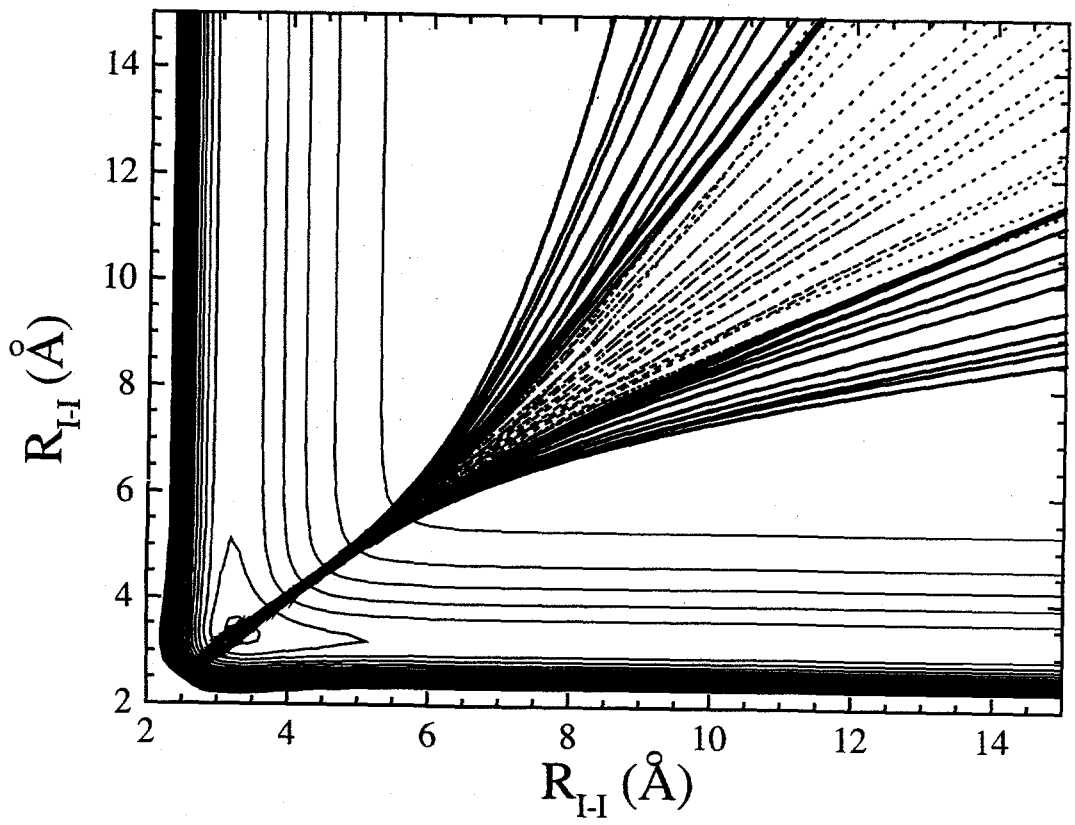

Figure 6 : Classical trajectories for symmetric three-body dissociation of I_3^- on potential energy surface.

V. Discussion

A. PFY spectrum

We studied the dissociation processes over two absorption bands of I_3^- in the range of 390nm (3.18eV) - 290nm (4.28eV). The consensus on the spectral assignment for those two bands is that those bands are due to transitions to either $^1\Sigma_{0+u}$ and $^3\Pi_{0+u}$ or mixed states of these two. These assignments are supported by the positive value of β parameter in our present photodissociation experiment.

Our PFY spectrum of I_3^- in the gas phase, which consists of two absorption bands, shows good agreement with the absorption spectrum of aqueous I_3^- as shown in Fig. 2. Specifically, there is no difference in positions of band maxima between solution and gas phase within our experimental error. This indicates little perturbation by solvent in these bands. However, there is a significant difference in width of the upper band, which is much narrower in our PFY spectrum than that in solution. As we pointed out in Sec. III. A., photodetachment of I_3^- plays a role in narrowing the upper band below 293nm. However, we still observe the band to be narrower on the red side of band maximum.

There are two possibilities for this difference. First, there might be more than one electronic transition in the lower band, while there might be one electronic transition in the upper band. Even though our tentative assignments for those two bands are made with only two symmetry-allowed transitions, these assignments are based on very simple calculations. With high level calculation, there might be more than two transitions with reasonable oscillator strength in our experimental range. Especially, the branching ratio into several dissociation channels shown in Tables 1 and 2 shows a big change around 3.64eV, which might be due to a new transition in the lower band.

Second, difference in width of the upper band can be due to the shape of potential energy surface. The photodissociation dynamics of I_3^- on the excited state surface was studied using the wavepacket simulation. In those studies, the London-Eyring-Polanyi-Sato (LEPS) potential energy surface was used for the excited state. Even though there are some difference in LEPS potential used by Banin[14] and Zanni,[24] the wavefunction of the ground state was projected onto the repulsive wall of the excited state in both cases. In those studies, it shows the consistent results with the resonant Raman study by Johnson *et al.*,[11,36] which observed the symmetric stretching motion as an initial motion on the excited state. If we assume that the Franck-Condon region for electronic transition only covers the repulsive wall for both upper and lower bands, the width of each band reflects the slope of repulsive wall for those surfaces. In our PFY spectrum, we observed that the upper band has much narrower width than the lower band. Therefore, the upper band in the Franck-Condon region might become steeper in the condensed phase than in the gas phase.

B. Photodissociation dynamics of I_3^-

In photodissociation of I_3^-, we observed channels 2 and 3 as two-body dissociation associated with the electronic transition to either upper or lower band. The energy difference between these two bands closely resembles the spin-orbit splitting of atomic iodine. Therefore, the lower and upper bands were originally assigned to the excited states of I_3^- that correlate with channels 2 and 3, respectively. However, pseudopotential calculations by Tasker *et al.*[37] connect these two bands with either

channel 3 or I + repulsive state I_2^- ($^2\Pi_g$) leading to channel 4 by examining symmetries of excited states of I_3^-, which are the mixed states of $^1\Sigma_{0+u}$ and $^3\Pi_{0+u}$.

In our experiment, we observed channels 2-4 from the electronic transition to either of those two bands and also channel 5 at the highest excitation energy (4.28eV). In addition, we observe the complicate behavior in branching ratio to channels 2-4 shown in Tables 1 and 2. These observations indicate that there are various curve-crossing during the dissociation of I_3^-. Therefore, a simple correlation diagram between excited states of I_3^- and dissociation asymptote is not appropriate for I_3^- dissociation.

Given this basic picture, we can compare our results with previous result in solution and gas phase.

First, in Fig. 4, the feature A at $h\upsilon \leq 3.64$eV drops abruptly at the translational energy corresponding to the opening of channel 3 instead of minimum translational energy for channel 2. It suggests that once channel 3 is energetically accessible, two-body dissociation prefers channel 3 over channel 2. Therefore, our $P(E_T)$ distroibutions in Fig. 4 show that the population of vibrational excited I_2^- product in channel 2 increases monotonically with v and drops very rapidly before it reaches dissociation limit of I_2^-.

Second, we compared our vibrational excitation with that observed in solution. In femtosecond dissociation experiments on I_3^- in solution,[12-17] the I_2^- products were observed in an average vibrational state of $\langle v \rangle = 12$ after initial excitation at 308nm (4.03eV). In our experiment at 4.15eV, we observe much higher vibrational excitations of I_2^-, that is the upper bound $\langle v \rangle = 52$ and 65 for channel 2 and 3, respectively. This hotter vibrational distribution of I_2^- product in the gas phase was also observed in the

previous FPES study[23,24] at lower hυ (3.18eV) and this difference is explained by strong coupling between the excited state surface of I_3^- and solvent molecule.

Third, we compare our result with the previous FPES study following 390nm (3.18eV) excitation.[23,24] In those study, they found a vibrational quantum number of <v> = 67, or 0.70 eV of vibrational energy of I_2^- product and 1:1 ratio for I^-: I_2^- photoproducts. Our data at excitation energy of 390nm (3.18eV) shows the upper bound <v> = 79, or 0.79 eV for channel 2. These two values shows close agreement, suggesting that most of excess energy goes into vibration of I_2^- product, instead of rotation. In addition, we observe around 1:1 ratio for two-body versus three-body dissociation in Table 2, which shows good agreement with FPES study. However, the upper bound <v> (=15, 0.19eV) for channel 3 is very different from that observed in FPES study. In FPES study, they measured vibrational energy by recording the coherent motion of I_2^-. At this excitation energy, less than one third of I_2^- product corresponds to channel 3 in our experiment. Therefore, it might be too small to detect the contribution from channel 3 in FPES signal.

Fourth, there have been some theoretical efforts to simulate the experimental results in solution[14] and gas phase[24] using wavepacket simulations on the LEPS potential. In those studies, the single LEPS potential surface was used to reproduce the lower absorption band and the average vibrational excitation of I_2^- product. As we prove in our experiment, simulations of vibrational excitation of I_2^- product on the single potential surface is clearly oversimplified.

VI. Conclusions

We have investigated the spectroscopy and dissociation dynamics of I_3^- in the range of 290-390nm, utilizing the method of fast beam photofragment translational spectrometer. This paper reports the first photofragment yield (PFY) spectrum of I_3^- in the gas phase. Two product mass ratios from the photodissocaition of I_3^- subsequent to the electronic transition are observed: 1:1 and 1:2 mass ratios. Based on our detection scheme, the product channel with 1:1 mass ratio is assigned to the symmetric three-body dissociation.

In the PFY spectrum of I_3^-, two absorption bands are observed with peaks around 290 and 360 nm. Compared to the absorption bands of I_3^- in solution, our PFY spectrum shows no significant solvent effect except for the band around 290nm, part of which are affected by the photodetachment process of I_3^-.

We probe the photodissociation dynamics of the I_3^- by measuring the translational energy of the 1:1 and 1:2 mass channel. For the 1:2 mass channel, the photodissociation of I_3^- produces the I_2^- ($\tilde{X}$) and either spin-orbit ground or the excited state of I atom. Based on our detection scheme, we assign the 1:1 mass channel as symmetric three-body dissociation.

ACKNOWLEDGEMENTS

This research is supported by the Director, Office of Energy Research, Office of Basic Energy Sciences, Chemical Sciences Division, of the U. S. Department of Energy under Contract No. DE-AC03-76SF00098.

References

[1] R. E. Buckles, J. P. Yuk, and A. I. Popov, J. Am. Chem. Soc. **74,** 4379 (1952).

[2] W. Gabes and D. J. Stufkens, Spectrochim. Acta **30A,** 1835 (1974).

[3] M. Mizuno, J. Tanaka, and I. Harada, J. Phys. Chem. **85,** 1789 (1981).

[4] T. Okada and J. Hata, Mol. Phys. **43,** 1151 (1981).

[5] K. Kaya, N. Mikami, Y. Udagawa, and T. Ito, Chem. Phys. Lett. **16,** 151 (1972).

[6] W. Kiefer and H. J. Bernstein, Chem. Phys. Lett. **16,** 5 (1972).

[7] M. Isci and W. R. Mason, Inorg. Chem. **24,** 271 (1985).

[8] W. Gabes and M. A. M. Nijman-Meester, Inorg. Chem. **12,** 589 (1973).

[9] J. C. Roy, W. H. Hanillm, and R. R. Williams Jr., J. Am. Chem. Soc. **77,** 2953 (1955).

[10] P. Fornier De Violet, R. Bonneau, and J. Jooussot-Dubien, Chem. Phys. Lett **28,** 569 (1974).

[11] A. E. Johnson and A. B. Myers, J. Chem. Phys. **102,** 3519 (1995).

[12] U. Banin, A. Waldman, and S. Ruhman, J. Chem. Phys. **96,** 2416 (1992).

[13] U. Banin and S. Ruhman, J. Chem. Phys. **98,** 4391 (1993).

[14] U. Banin, R. Kosloff, and S. Ruhman, Israel J. of Chem. **33,** 141 (1993).

[15] U. Banin, A. Bartana, S. Ruhman, and R. Kosloff, J. Chem. Phys. **101,** 8461 (1994).

[16] U. Banin, R. Kosloff, and S. Ruhman, Chem. Phys. **183,** 289 (1994).

[17] U. Banin and S. Ruhman, J. Chem. Phys. **99,** 9318 (1993).

[18] T. Kuhne, R. Kuster, and P. Vohringer, Chem. Phys. **233,** 161 (1998).

[19] T. Kuhne and P. Voringer, J. Chem. Phys. **105,** 10788 (1996).

[20] T. Kuhne and P. Vohringer, J. Phys. Chem. A. **102,** 4177 (1998).

[21] K. Do, T. P. Klein, C. A. Pommerening, and L. S. Sunderlin, J. Am. Soc. Mass Spectrom. **8,** 688 (1997).

[22] T. R. Taylor, K. R. Asmis, M. T. Zanni, and D. M. Neumark, J. Chem. Phys. **110,** 7607 (1999).

[23] M. T. Zanni, B. J. Greenblatt, A. V. Davis, and D. M. Neumark, Proceedings of SPIE **3271,** 196 (1998).

[24] M. T. Zanni, B. J. Greenblatt, A. V. Davis, and D. M. Neumark, J. Chem. Phys. **111,** 2991 (1999).

[25] D. R. Cyr, R. E. Continetti, R. B. Metz, D. L. Osborn, and D. M. Neumark, J. Chem. Phys. **97,** 4937 (1992).

[26] R. E. Continetti, D. R. Cyr, R. B. Metz, and D. M. Neumark, Chem. Phys. Lett. **182,** 406 (1991).

[27] D. L. Osborn, D. J. Leahy, D. R. Cyr, and D. M. Neumark, J. Chem. Phys. **104,** 5026 (1996).

[28] D. Hanstorp and M. Gustafsson, J. Phys. B. **25,** 1773 (1992).

[29] M. T. Zanni, T. R. Taylor, B. J. Greenblatt, B. Soep, and D. M. Neumark, J. Chem. Phys. **107,** 7613 (1997).

[30] K. P. Huber and G. Herzberg, *Molecular Spectra and Molecular Structure. IV. Constants of Diatomic Molecules* (Van Nostrand Reinhold Co., New York, 1979).

[31] R. S. Mulliken, J. Chem. Phys. **55,** 288 (1971).

[32] M. T. Zanni, V. S. Batista, B. J. Greenblatt, W. H. Miller, and D. M. Neumark, J. Chem. Phys, **110,** 3748 (1999).

[33] J. Faeder, N. Delaney, P. E. Malsen, and R. Parson, Chem. Phys. Lett. **270,** 196 (1997).

[34] D. G. Truhlar and J. T. Muckerman, in *Atom-Molecule Collision Theory - A Guide for the Experimentalist*, edited by R. B. Bernstein (Plenum, New York, 1979), pp. .

[35] S. K. Kim and D. R. Herschbach, Faraday Discuss. Chem. Soc. **84,** 159 (1987).

[36] A. E. Johnson and A. B. Myers, J. Phys. Chem. **100,** 7778 (1996).

[37] P. W. Tasker, Mol. Phys. **33,** 511 (1977).

Chapter 6. Photodissociation Dynamics of the Triiodine radical (I_3)

Abstract

The excited states of I_3 radical are investigated using anion photoelectron spectroscopy and fast beam photofragment translational spectroscopy. The ground and three excited states of I_3 radical are characterized by photoelectron spectroscopy of I_3^- at 213nm. At selected photon energies (4.59, 4.96, and 5.17eV), photodissociation of I_3 radical is observed, which is the first evidence for electronic transition of I_3. Two product channels from the photodissociation of I_3 subsequent to the electronic transition are observed: channels with 1:1and 1:2 fragment mass ratios. The $P(E_T)$ distributions for products with mass ratio 1:2 shows that electronic transitions at the above photon energies produce I_2 in various electronic states along with atomic I in its $^2P_{3/2}$ or $^2P_{1/2}$ state. For the channel with mass ratio 1:1, the $P(E_T)$ distributions shows several sharp peaks with some broad background at low translational energy. This channel is assigned to symmetric three-body dissociation.

I. Introduction

The triiodine radical (I_3) has been proposed to be a key intermediate in the halogen atom recombination reaction ($I+I_2 \rightarrow I_2+I$).[1-6] In addition, the existence of stable excited state of I_3 radical has been postulated to explain the efficient quenching of $I^*(^2P_{1/2})$ by I_2 leading to the nearly resonant energy transfer to the $I\ (^2P_{3/2}) + I_2\ (25<v<43)$ products by a non-adiabatic process[7-9]. Despite the proposed key role of triiodine radical (I_3) in those reactions, only the ground state of I_3 radical has been proved as a stable species by anion photoelectron spectroscopy.[10] Therefore, there has been little information on electronic excited states of I_3 radical and how I_3 radical dissociates after electronic excitation. In this paper, we address these issues using a combination of photoelectron spectroscopy and photofragment translational spectroscopy.

The only experimental data on I_3 comes from the photoelectron (PES) spectra of I_3^-. The PES spectrum of I_3^- anion was taken by Taylor *et al.*[10] and the electron affinity of I_3^- was determined to be 4.226±0.013eV. They observed the vibrational progression in the ground state of I_3 radical and found an excited state 0.27eV above the ground state. Simulation of the PES spectrum suggests that the I_3 ground state is linear and centrosymmetric with a symmetric stretch frequency of 115±5 cm^{-1} and is bound by 0.14eV. In another low-resolution PES spectra by Zanni *et al.*,[11,12] two more electronically excited states of I_3 radical were identified and found to lie 0.68 and 1.48 eV above the ground state of I_3 radical.

However, the ground and excited states of I_3 radical have not been assigned to electronic states. Recently, the semiempirical DIM (diatomic in molecules) method was used to simulate the PES spectrum of I_3 radical by Margulis *et al.*[13] In this calculation, the

ground state of I_3 radical was identified as the centrosymmetric molecule with Ω (the projection of total angular momentum on the molecular axis) = 1/2 and was bound by 0.192 eV. This assignment on the ground state differs from the ground state of the isovalent molecule XeF_2^+. Photoelectron spectra of XeF_2 were taken by Brundle *et al.*[14] and Yates *et al.*[15], and the ground and five excited states of XeF_2^+ were assigned as $^2\Pi_{u,3/2}$, $^2\Pi_{u,1/2}$, $^2\Sigma_{g,1/2}$, $^2\Pi_g$, $^2\Pi_u$, and $^2\Sigma_{u,1/2}$ states in order of increasing energy. In addition, The PES spectrum of Cl_3^- was also taken by Kaledin et. al,[16] which showed two features. By comparing the PES spectrum with *ab initio* calculation,[17] these two features were assigned as the $^2\Pi_u$ or $^2\Sigma_g^+$ states, which were nearly degenerate, and the $^2\Pi_g$ state.

In this paper, we investigate the low-lying excited state of I_3 radical with anion photoelectron spectroscopy and the higher excited states of I_3 radical with fast beam photofragment translational spectroscopy. In anion photoelectron spectroscopy of I_3^-, three electronically excited states of I_3 radical are identified with better resolution than previously.[11] We also investigate the photodissociation of I_3 radical at selected photon energies (4.59, 4.96, and 5.17eV) by preparing a pure source of I_3 radicals through photodetachment of the mass-selected I_3^- anion. We present the first evidence of electronic transition in I_3 by observing photodissociation of I_3 radical and identify the several dissociation channels, including three-body dissociation of I_3.

II. Experimental Setup

Two different instruments, a negative ion photoelectron spectrometer and a fast radical beam photofragment translational spectrometer, are used for this study. In both, argon gas (3psig) flows over iodine crystals (I_2) at the room temperature. The resulting

mixture supersonically expands through a pulsed valve into the source region of the apparatus. Anions were generated by a 1 keV electron beam, which crosses the expansion, and cooled to 20-50 K during expansion.

In the anion photoelectron spectrometer,[18,19] negative ions generated in the ion source pass through a skimmer into a differentially pumped region. They are extracted perpendicular to their flow direction by a pulsed electric field and injected into a linear reflectron time-of-flight (TOF) mass spectrometer,[20,21] affording a mass resolution ($m/\Delta m$) of 2000. The ion of interest is selectively photodetached using the fifth harmonic (5.822 eV) of a pulsed Nd:YAG laser. The electron kinetic energy (*eKE*) distribution is determined by TOF analysis in a 1 m field-free flight tube. The energy resolution is 8-10 meV at 0.65 eV and degrades as $(eKE)^{3/2}$. The data in electron kinetic energy is converted to electron binding energy (*eBE*) by subtracting it from the photon energy. The anion photoelectron is plotted in *eBE* as described by equation (1) where *EA* is the adiabatic electron affinity and E^o and E^- are the internal energies of the neutral and anion, respectively.

$$eBE = h\nu - eKE = EA + E^o - E^- \qquad (1)$$

The angular dependence of the photodetachment intensity for polarized light and randomly oriented molecules is given by equation (2) below[22]

$$\frac{d\sigma}{d\Omega} = \frac{\sigma_{total}}{4\pi}\left[1 + \frac{\beta(eKE)}{2}(3\cos^2\theta - 1)\right] \qquad (2)$$

where θ is the angle between the electric vector of the photon and the direction of electron ejection, σ_{total} is the total photodetachment cross section and $\beta(eKE)$ is the asymmetry parameter ($-1 \leq \beta \leq 2$). Each electronic state typically has a characteristic

asymmetry parameter (β) and this can be used to distinguish peaks of overlapping electronic transitions. The asymmetry parameter of a peak can be calculated[23] using equation (3)

$$\beta = \frac{I_{0^o} - I_{90^o}}{\frac{1}{2} I_{0^o} + I_{90^o}} \qquad (3)$$

where I_{0^o} and I_{90^o} are the intensities of the peak taken at the polarization angles $\theta = 0^o$ and 90°.

Photodissociation of I_3 radical was studied using the fast radical beam photofragment translational spectrometer. In this instrument,[24,25] negative ions formed in the source region are accelerated to 8 keV and separated temporally by a time-of-flight (TOF) mass spectrometer. The I_3^- ion packet is intersected by a pulsed beam from KrF excimer laser (248nm) photodetaching some of anions to yield neutral I_3 radicals. Any remaining ions are removed by the application of an electrical deflection pulse. The I_3 neutral packet is then intersected by linearly polarized pulsed dye laser beam and some of I_3 neutrals absorb a photon and dissociate. Part of I_3^- ion can photodissociate instead photodetch at 248nm. However, any photofragments from I_3^- are blocked by 1mm pinhole installed before the second laser.

A block strip across the center of detector prevents parent molecules from reaching the detector, whereas photofragments with sufficient recoil energy miss the beam block and strike the detector. These fragments are generally detected with high efficiency (up to 50%) due to their high laboratory kinetic energy.

In the photodissociation experiment, two photofragments from a parent molecule are collected in coincidence using a time- and position-sensitive detector at a fixed

wavelength and the dissociation dynamics are investigated. We measure the distance R between the two fragments on the detector, the time difference τ of their arrival, and the individual displacements of the two fragments, r_1 and r_2, from the detector center for each dissociation event. From these we obtain the center-of mass translational energy E_T, the scattering angle with respect to laser polarization, θ, and the two photofragment mass ratio m_1/m_2 via

$$\frac{m_1}{m_2} = \frac{r_2}{r_1}(1 - \frac{\upsilon_0 \tau}{l}) \tag{4}$$

$$\theta = \tan^{-1}(\frac{R}{\upsilon_0 \cdot \tau}) \tag{5}$$

$$E_T \cong E_0 \cdot \frac{\mu}{M} \cdot \frac{(\upsilon_0 \cdot \tau)^2 + R^2}{l^2} \tag{6}$$

Here E_0 and υ_0 are the ion beam energy and velocity, respectively, μ is the reduced mass of photofragment, and l is the flight length from the photodissociation region to the detector. Although the relative recoil distance R is determined with high precision ($R/\Delta R \approx 100$), the individual recoil distance r_1 and r_2 are less precisely determined due the finite size of the parent beam, resulting in $m/\Delta m \approx 10$. The energy resolution ($\Delta E_T/E_T$) under the conditions in these studies is around 2%.

III. Results

A. Photoelectron spectrum of I_3^- anion

Fig. 1 shows the anion photoelectron spectra of I_3^- taken at 213nm (5.822eV). These spectra taken at two polarization angles have been normalized with respect to laser shots to facilitate comparison of peak intensities. All features in the $\theta=90^0$ spectrum

(solid line) are much more intense than the features in the $\theta=0^0$ spectrum (dotted line). The four main features are labeled as X, A, B, and C in the spectra. The two additional features labeled with an asterisk (*) are due to photodetachment of I^-, which is formed from the photodissociation of the parent I_3^- anion.

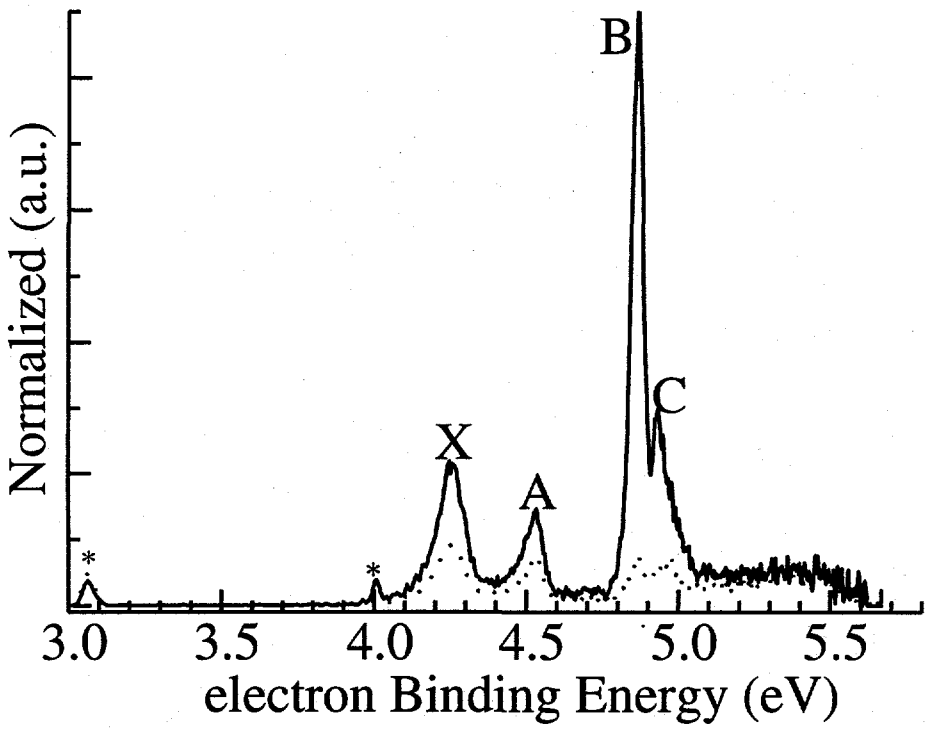

Figure 1 : Photoelectron spectrum of I_3^- anion at 5.822eV taken at laser polarization $\theta = 90^0$ (the solid line) and 0^0 (the dotted line).

Absolute peak positions and the asymmetry parameters (β) for corresponding peaks are listed in Table 1. In the previous PES spectrum at 4.657eV,[10] vibrational structure in the ground state (peak X) was resolved, but the first excited state (peak A) showed no such structure.[10] The additional features we observe here, B and C, do not exhibit vibrational structure either.

Table 1. Peak position and asymmetry parameter (β) for the I_3^- photoelectron spectrum.

Peak	Position (eV)	Asymmetry parameter (β)	Splitting from the origin of $\tilde{X}$ state of I_3 (eV).
X	4.254	-0.48	0.028
A	4.533	-0.41	0.307
B	4.869	-0.88	0.643
C	4.933	-0.69	0.707

We first consider the assignment of peaks X and A. Based on the semiempirical calculation with the spin-orbit coupling, the ground state molecular orbital configuration for the I_3^- anion is determined to be $...(\sigma_u)^2(\pi_u)^4(\pi_g)^4(\sigma_g)^2(\pi_u^*)^4$.[26] Removal of an electron from the highest occupied molecular orbital leaves a I_3 radical in $^2\Pi_u$ spin-orbit states ($^2\Pi_{u,3/2}$ and $^2\Pi_{u,1/2}$). In addition, the similar asymmetry parameters for peaks X and A in Table 1 suggests that photoelectrons for these two features might be removed from the same orbital of I_3^-. Therefore, peaks X and A are tentatively assigned to $^2\Pi_{u,3/2}$ and $^2\Pi_{u,1/2}$ states, respectively. This tentative assignment shows good agreement with results on isovalent species XeF_2^+.[14,15] However, it is contradictory to calculation by Margulis *et al.*,[13] which assigned the ground state as the state with Ω=1/2. Also, the asymmetry parameters for peaks X and A showed photon energy dependence and were found to be 0.24 and –0.21 at 266nm, which were misreported in the previous paper.

Peak B shows a little more negative asymmetry parameter than that for peak C. However, part of peak C is overlapped by peak B, indicating that the asymmetry parameter for peak C might be much less negative than that of peak B. This difference in asymmetry parameter suggests these two peaks can be assigned to electronic states

originated by removing a electron from different orbitals of I_3^-. Removal of an electron from the second and third highest occupied molecular orbital leaves a I_3 radical in $^2\Sigma_{g,1/2}$, and $^2\Pi_g$ spin-orbit states ($^2\Pi_{g,3/2}$, $^2\Pi_{g,1/2}$). Therefore, peaks B, and C are tentatively assigned as $^2\Sigma_{g,1/2}$, and one of $^2\Pi_g$ spin-orbit states ($^2\Pi_{g,3/2}$, $^2\Pi_{g,1/2}$). In the absence of an accurate calculation, we cannot make any more specific assignments on the electronic states of I_3.

B. Photodissociation of I_3 radical

Using the dissociation energy of I_3[10] and the well-known energetics of I_2[27] and I,[28] the energy diagram for I_3 photodissociation along with three excited states of I_3 observed in our PES spectrum is shown in Fig. 2. In the photodissociation experiment, the I_3 radical is generated by photodetaching the I_3^- anion. For most system studied on this instrument, the energy of photodetachment is just above threshold, so that only radicals in their vibrationally ground state are produced. However, the PES of I_3^-[10] shows an extended progression in a low frequency vibration, so detachment just above threshold does not produce sufficient I_3 to carry out the experiment. Instead, we detach at 5.00eV, well above the energy needed to populate the entire ground state Franck-Condon envelope of vibrational levels, and the three excited states, too. The excited states lie well above the lowest $I+I_2$ asymptote, and we assume they dissociate in the 10μs delay between the detachment and dissociation pulses.

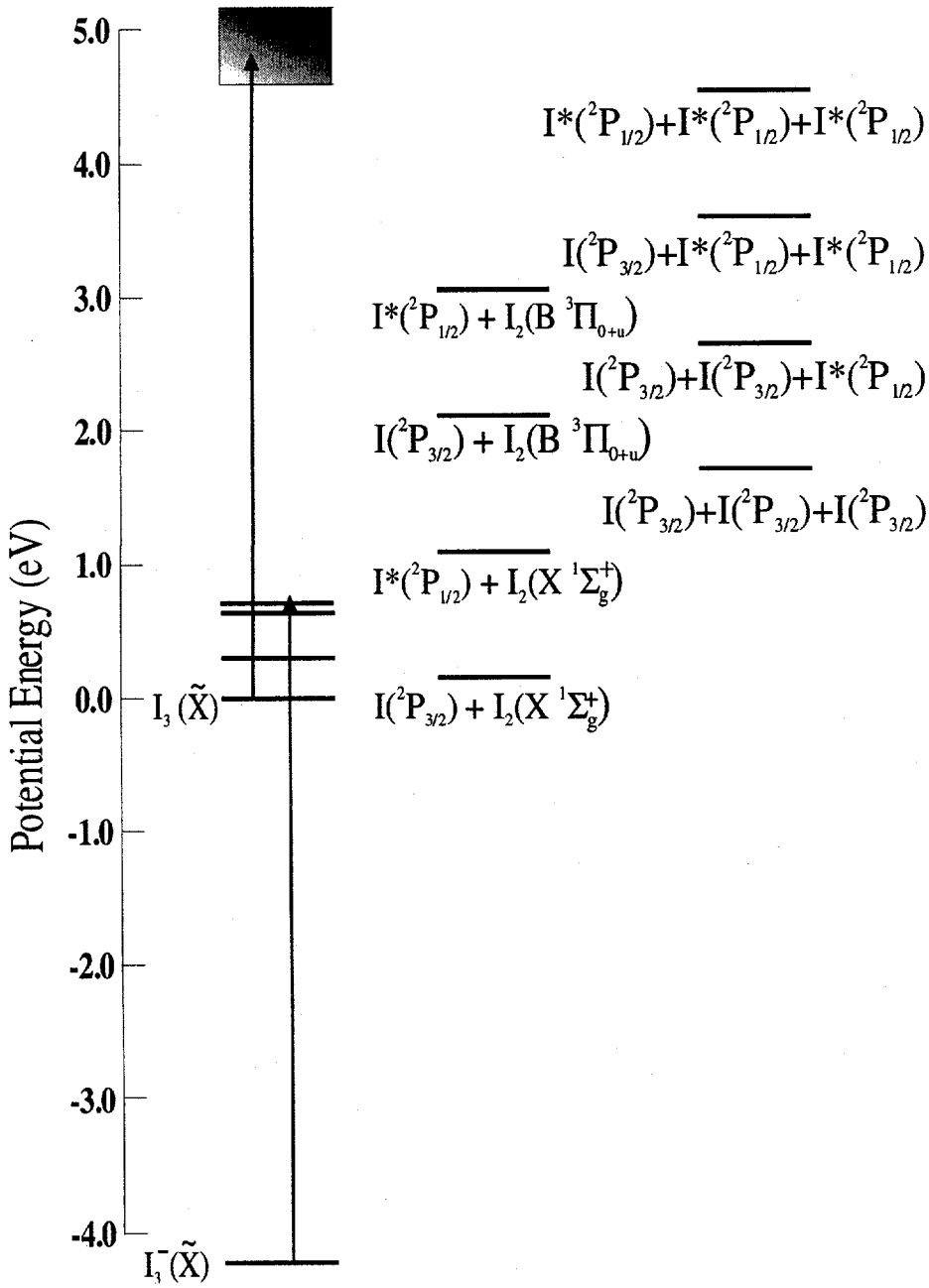

Figure 2 : Energetics of I_3. The relative energies of three excited states of I_3 observed in our PES spectra are shown in solid lines.

1. Photofragment Mass Ratio (m_1/m_2)

The photodissociation experiment with I_3 neutral is performed at selected photon energies: 4.59, 4.96, and 5.17 eV. At these excitation energies, dissociation events are observed and this is the first evidence of the electronic transition of I_3 radical.

The first information we get from this experiment is the fragment mass ratio through equation (4). In Fig. 3, the fragment mass ratio obtained at 4.59eV shows very broad peaks around 0.5 and 1.0 because of the poor mass resolution ($m/\Delta m \approx 10$). However, it clearly shows that there are two product channels occurring at this photon energy: channels with 1:2 and 1:1 mass ratios.

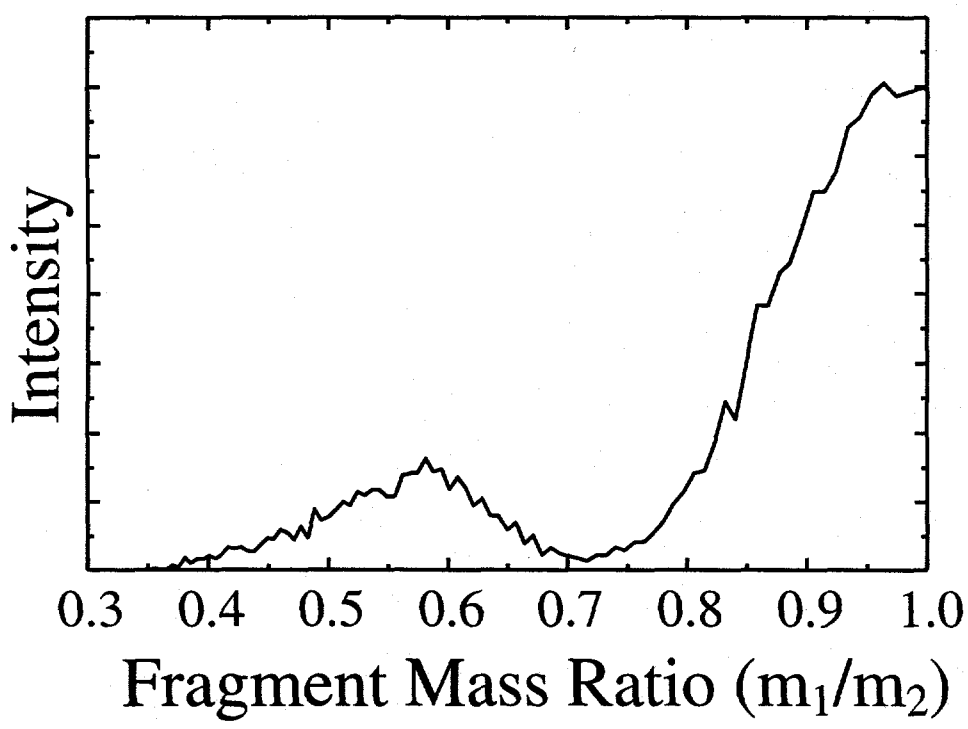

Figure 3 : Photofragment mass ratio (m_1/m_2) of I_3 at photon energy of 4.59 eV (270nm).

As shown in Fig. 2, there are several product channels that are thermodynamically feasible:

$$I_3(\tilde{X}) + h\nu_{photon} \rightarrow I(^2P_{3/2}) + I_2(X\ ^1\Sigma_g^+) \qquad D_0 = 0.14 \pm 0.06\ eV \text{ (channel 1)}$$

$$I^*(^2P_{1/2}) + I_2(X\ ^1\Sigma_g^+) \qquad 1.08 \pm 0.06\ eV \text{ (channel 2)}$$

$$I(^2P_{3/2}) + I_2(B\ ^3\Pi_{u,0}) \qquad 2.10 \pm 0.06\ eV \text{ (channel 3)}$$

$$I^*(^2P_{1/2}) + I_2(B\ ^3\Pi_{u,0}) \qquad 3.04 \pm 0.06\ eV \text{ (channel 4)}$$

$$I(^2P_{3/2}) + I(^2P_{3/2}) + I(^2P_{3/2}) \qquad 1.69 \pm 0.06\ eV \text{ (channel 5)}$$

$$I^*(^2P_{1/2}) + I(^2P_{3/2}) + I(^2P_{3/2}) \qquad 2.63 \pm 0.06\ eV \text{ (channel 6)}$$

$$I^*(^2P_{1/2}) + I^*(^2P_{1/2}) + I(^2P_{3/2}) \qquad 3.57 \pm 0.06\ eV \text{ (channel 7)}$$

$$I^*(^2P_{1/2}) + I^*(^2P_{1/2}) + I^*(^2P_{1/2}) \qquad 4.51 \pm 0.06\ eV \text{ (channel 8)}$$

In addition to the above channels, the low-lying excited states of I_2 (A' $^3\Pi_{2u}$ and A $^3\Pi_{1u}$) are also accessible at excitation used here. However, we cannot distinguish I (or I*) + I_2 (A' $^3\Pi_{2u}$ and A $^3\Pi_{1u}$) from I (or I*) + vibrationally excited I_2 in the X state.

Channels 1-4 are two-body dissociation and channels 5-8 are three-body dissociation channels. In our dynamics experiment, only two photofragments from the parent molecule are collected in coincidence. Therefore, the two-body dissociation of I_3 generates the channel with 1:2 fragment mass ratio. However, if the I_3 radicals undergo symmetric three-body dissociation, the two end atoms fly apart at approximately the same speed and the middle one follows the same trajectory of parent molecule and will hit the beam block in front of detector. As a result, symmetric three-body dissociation of I_3 can generate the channel with 1:1 mass ratio in our experiment. Therefore, we assign peaks around 0.5 and 1.0 in Fig. 3 as two-body dissociation and symmetric three-body dissociation of I_3 radical, respectively. In the photodissociation experiment of I_3^-,[29] two-

and symmetric three-body dissociation were observed, yielding a similar distribution for fragment mass ratio.

At every photon energy we probed, a similar product mass ratio is obtained. For each channel, the joint translational energy and angular distribution is given by

$$P(E_T,\theta) = P(E_T)\cdot(1+\beta(E_T)\cdot(3\cos^2\theta-1)/2) \qquad (7)$$

Here, E_T is the translational energy release, θ is the angle between the photofragment recoil velocity vector and the laser polarization, and $\beta(E_T)$ is the anisotropy parameter. For the channel with 1:1 mass ratio, $\mu=1/2\ m_I$ (m_I = mass of I atom) in equation (6) as discussed previously. The limiting cases of $\sin^2\theta$ and $\cos^2\theta$ angular distributions are given by $\beta = -1$ and $+2$, respectively. Generally speaking, a parallel transition yields $\beta>0$, whereas $\beta<0$ for a perpendicular transition.

We find $\beta>0$ for both mass channels, suggesting that the electronic transition is a parallel transition. However, accurate measurement of the β parameter is hampered because the geometrical constraint of detector allows us to collect photofragments only at very restricted angles.

2. 1:2 mass channel

For the channel with 1:2 mass ratio, $P(E_T)$ distributions are shown in Fig. 4 (a)-(c). The $P(E_T)$ distributions show several trends with increasing photon energy. At the lowest excitation energy (4.59eV), three features labeled as A, B, and C in Fig. 4 (a) are visible. As the photon energy increases, the feature C remains at the same E_T and features B and C moves to the higher E_T. Also, with increasing excitation energy, another feature, labeled as C' in Fig. 4 (b) and (c), becomes visible between features A and B.

At every excitation energy, channels 1-4 are energetically possible. The four combs in each plot show the maximum and minimum translational energies for channels 1-4; at energies below the minimum, the I_2 internal energy would exceed its bond dissociation energy and it would dissociate long before reaching the detector. Then we compare those ranges with appearances of features A, B, C, and C'. Through this comparison, the feature A is assigned as channel 1 because of the nice agreement between the range of channel 1 and the feature A. For the same reason, the feature B can be assigned as either channel 2 or channel 3. However, we cannot distinguish channel 3 from 2, because the ranges of channel 3 is overlapped by that of channel 2. Therefore, we assign feature B as a combination of channels 2 and 3. At the two highest excitation energies (4.96 and 5.17eV), the feature C' can be assigned as channel 4. However, the range of channel 4 overlaps that of the feature C at the lowest excitation energy (4.59 eV). Therefore, it is not clear whether channel 4 is produced at that excitation energy. The assignment of the feature C is not clear, because there is no stable I_2 + I channel in those energy range. Therefore, the origin of feature C is related to three-body dissociation and considered in the next section.

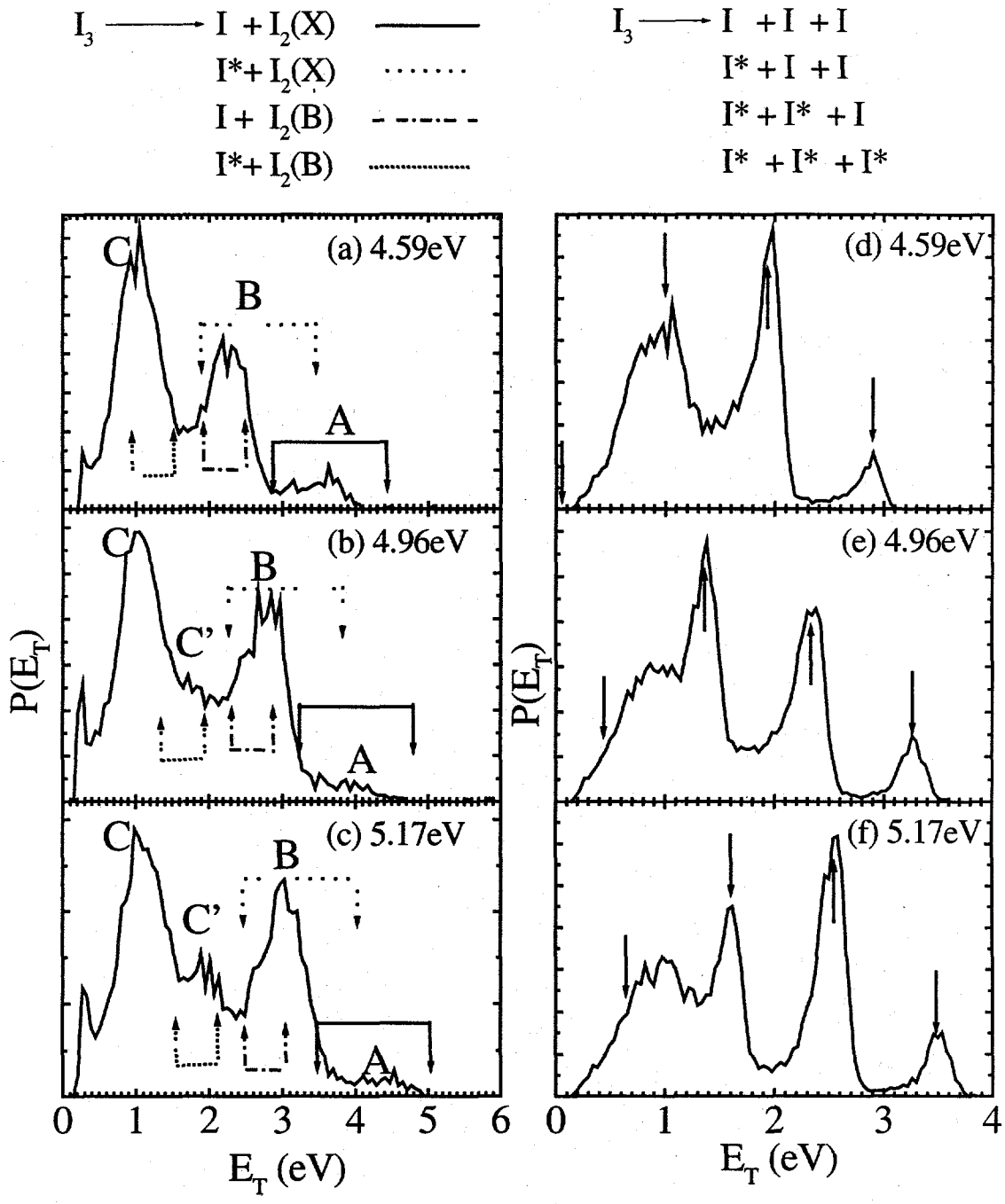

Figure 4 : Translational energy P(E_T) distributions of I_3 at photon energies shown at the right upper corner of each plot: (a)-(c) with 1:2 mass ratio and (d)-(f) with 1:1 mass ratio.

1:1 mass channel

Fig. 4 (d)-(f) shows the P(E_T) distributions for the 1:1 mass channel. Our P(E_T) distributions shows several sharp peaks along with broad feature around E_T= 1.0eV. The three-body dissociation of I_3 generates three I atoms, in which all the available energy goes to the translational or possible electronic energy of photofragments. At every photon energy we probed, channels 5-8 are energetically possible for the three-body dissociation of I_3. The expected E_T for each channel is marked by arrow in Fig. 4 (d)- (f). Positions of sharp features show excellent agreement with positions of arrows, providing further proof that the three-body dissociation is symmetric and the ground state of I_3 radical is linear and centrosymmetric. It is clear that channels 5 and 6 are active at every excitation energy. Channel 7 becomes visible at hν≥ 4.96eV and channel 8 is not seen at any energy used here.

While the sharp peaks in Fig. 4 (d)-(f) correspond to the appropriate kinetic energies for symmetric three-body dissociation, we note that (a) the peaks are considerably broader than the experimental kinetic energy resolution, ~300meV vs. ~20meV, and (b) there are broad features in addition to the sharp peaks. The similar behavior was observed in the previous photodissociation study of I_3^-,[29] in which symmetric three-body dissociation was observed with the same instrument as we use in this study. Therefore, we compare our results with three-body dissociation of I_3^-.

First, in I_3^- dissociation, they observed the broader peaks (~150meV) than instrumental resolution (~20meV), which correspond to symmetric three-body dissociation. Using classical trajectory calculations, it was demonstrated that trajectories for symmetric three-body dissociation do not exactly follow symmetric stretching

coordinate leading to broadening of peaks. However, the width (~300meV) of peaks in three-body dissociation of I_3 is much wider than that (~150meV) of I_3^-. This difference can be explained by the initial condition of I_3^- and I_3 parent molecules. As discussed in the first paragraph of Sect. III. B., the vibrationally hot I_3 radical is generated in the photodetachment process, while only the vibrationally cold I_3^- was prepared through the supersonic expansion. Therefore, peaks for symmetric three-body dissociation of I_3 might be broadened by a combination of the small spread of symmetric three-body dissociation along the asymmetric stretching coordinate and the generation of vibrationally excited I_3 radical in the photodetachment process.

Second, broad features were observed at low E_T in both 1:1 mass channel from I_3^- and I_3 dissociation. In our classical trajectory calculation of I_3^-, some trajectories, which produce three-body dissociation, spread so much along asymmetric stretching coordinate during the dissociation that some of those can be detected as 1:1 or 1:2 mass channels in experimental setup. However, none of trajectories reach the repulsive wall of I_2^- product valley, thus can be still assigned as symmetric three-body dissociation. In that sense, broad features at low E_T in I_3^- photodissociation were assigned as those types of symmetric three-body dissociation.

However, in photodissociation study with I_3, broad features around 1.0eV in Fig. 4 (d)-(f) are much larger than those in I_3^- dissociation and are similar in width and position of feature C in Fig. 4 (a)-(c). Part of P(E_T) distribution in 1:2 mass channel are assigned as channel 3 and 4, which produce the predissociative B state of I_2 product. Therefore, part of I_2 product in the B state, which undergoes the radiation decay to the ground state of I_2, can be detected as 1:2 mass channel leading to feature C' in Fig. 4 (b)

and (c), while rest of I_2 in the B state can predissociate and produce the asymmetric three-body dissociation through process (a).

$$I_3 \rightarrow I + I_2(B) \xrightarrow{\text{predissociation}} I + I + I \qquad (a)$$

$$I^* + I_2(B) \xrightarrow{\text{predissociation}} I^* + I + I$$

In addition, various repulsive states of I_2, which correlate with two I atoms in the spin-orbit ground or excited states, are energetically accessible. Therefore, there is no I_2 product valley in the potential energy surface of I_3 involving these repulsive states. In that sense, broad features around 1.0eV in Fig. 4 (d)-(f) and feature C in Fig. 4 (a)-(c) are tentatively assigned as asymmetric three-body dissociation.

IV. Discussion

In anion photoelectron spectroscopy of I_3^-, the ground and three low-lying excited states of I_3 are observed. The existence of low-lying excited states of I_3 was postulated by Leone and Houston in the quenching experiment ($I^*+I_2 \rightarrow I+I_2(v=25\text{-}43)$).[7-9] As shown in Fig. 2, three excited states of I_3 radical observed in our PES spectrum lie above the first dissociation limit ($I+I_2(X)$) and below the second dissociation limit ($I^*+I_2(X)$). From the dissociation asymptote of $I(^2P_{3/2})+I_2(X)$, two electronic states can be generated: states with either $\Omega = 3/2$ or $1/2$. Therefore, two of the four states observed in the PES spectrum can adiabatically correlate with $I(^2P_{3/2})+I_2(X)$, suggesting that either of other two states might correlate with $I^*+I_2(X)$. Therefore, one of the three excited states observed in PES spectrum might be responsible for the efficient quenching of I^* by I_2 in I^*+I_2 reaction.

We investigate higher excited state in the range of 4.59-5.17 eV above the ground state of I_3 by fast beam photofragment translational spectroscopy. First, consider the

nature of the electronic state of I_3 in that range. Our photodissociation experiment shows that the electronic transition of I_3 radical at photon energies of 4.59, 4.96, and 5.17eV is a parallel transition, suggesting the excited state of I_3 in those photon energy ranges has the same value of Ω as the ground state of I_3.

At every excitation energy, we observe multiple dissociation channels. However, it is very difficult to calculate the branching ratio for these various dissociation channels for following reasons: 1) some of dissociation channels share the same range of E_T and 2) it is difficult to estimate the effect of asymmetric three-body dissociation on 1:2 and 1:2 mass channel in Fig.4. However, some general trends are observed. First, at every excitation energy, the lowest dissociation channels for 2-body ($I+I_2(X)$) and 3-body dissociation (I+I+I) are not dominant channels. As shown in Fig.4, at every excitation energy, feature B (channel 2 and 3) is larger than feature A (channel 1) and the peaks for channel 5 are much smaller than peaks for channels 6 and 7. This indicates that I_3 dissociation at those excitation energy preferentially produce the excited state of product. Second, a peak for channel 8 ($I^*+I^*+I^*$) was not observed in Fig. 4 (d)-(f). In the potential energy curve of I_2, only repulsive states of I_2 correlate with I^*+I^*. Therefore, there is no I_2 product valley in potential energy surfaces of I_3 for channel 8. This might cause the majority of dissociation of I_3 on those potential energy surfaces to undergo the asymmetric three-body dissociation, which is consistent with our tentative assignment on the broad features at low E_T in Fig. 4.

Photodissociation of I_3 radical shows the interesting dissociation dynamics. However, most of processes cannot be fully understood for lack of theoretical

information on the excited states of I_3 radical. We hope that this study encourages people to pursuit the potential energy surface of the excited state of I_3 radical.

ACKNOWLEDGEMENTS

The author thanks Dr. Arthur Suits for allowing me to use the KrF excimer laser for this study. This research is supported by the Director, Office of Energy Research, Office of Basic Energy Sciences, Chemical Sciences Division, of the U. S. Department of Energy under Contract No. DE-AC03-76SF00098.

References

[1] R. M. Noyes and J. Zimmerman, J. Chem. Phys. **18,** 656 (1950).

[2] M. I. Christie, A. J. Harrison, R. G. W. Norrish, and G. Porter, Proc. Royal. Soc. (London) **A231,** 446 (1955).

[3] M. I. Christie, J. Am. Chem. Soc. **84,** 4066 (1962).

[4] D. L. Bunker and N. Davidson, J. Am. Chem. Soc. **80,** 5090 (1958).

[5] J. A. Blake and G. Burns, J. Chem. Phys. **54,** 1480 (1971).

[6] V. I. Balykin, V. S. Lektokhov, V. I. Mishin, and V. A. Semchishen, Chem. Phys. **17,** 111 (1976).

[7] G. E. Hall, W. J. Marinelli, and P. L. Houston, J. Phys. Chem. **87,** 2153 (1983).

[8] H. Hofmann and S. R. Leone, J. Chem. Phys. **69,** 641 (1978).

[9] J. I. Cline and S. R. Leone, J. Phys. Chem. **95,** 2917 (1991).

[10] T. R. Taylor, K. R. Asmis, M. T. Zanni, and D. M. Neumark, J. Chem. Phys. **110,** 7607 (1999).

[11] M. T. Zanni, B. J. Greenblatt, A. V. Davis, and D. M. Neumark, Proceedings of SPIE **3271,** 196 (1998).

[12] M. T. Zanni, B. J. Greenblatt, A. V. Davis, and D. M. Neumark, J. Chem. Phys. **111,** 2991 (1999).

[13] C. J. Margulis, D. A. Horner, S. Bonella, and D. F. Coker, J. Phys. Chem. A. **103,** 9552 (1999).

[14] C. R. Brundle, M. B. Robin, and G. R. Jones, J. Chem. Phys. **52,** 3383 (1970).

[15] B. W. Yates, K. H. Tan, G. M. Bancroft, L. L. Coatsworth, J. S. Tse, and G. J. Schrobilgen, J. Chem. Phys. **84,** 3603 (1986).

[16] A. L. Kaledin, M. C. Heaven, K. Morokuma, and D. M. Neumark, Chem. Phys. Lett. **306,** 48 (1999).

[17] A. L. Kaledin, M. C. Heaven, W. G. Lawrence, Q. Cui, J. E. Stevens, and K. Morokuma, J. Chem. Phys. **108,** 2771 (1998).

[18] R. B. Metz, A. Weaver, S. E. Bradforth, T. N. Kitsopoulos, and D. M. Neumark, J. Phys. Chem. **94,** 1377 (1990).

[19] C. Xu, G. R. Burton, T. R. Taylor, and D. M. Neumark, J. Chem. Phys. **107,** 3428 (1997).

[20] B. A. Mamyrin and D. V. Shmikk, Zhu. Eksp. Teoretic. Fiziki **49,** 762 (1979).

[21] G. Markovich, R. Giniger, M. Levin, and O. Cheshnovsky, J. Chem. Phys. **95,** 9416 (1991).

[22] J. Cooper and R. N. Zare, in *Lectures in Theoretical Physics*, Vol. XI-C, edited by S. Geltman, K. T. Mahanthappa, and W. E. Brittin (Gordon and Breach, New York, 1969), pp. .

[23] K. M. Ervin and W. C. Lineberger, in *Advances in Gas Phase Ion Chemistry*, Vol. 1 (JAI Press Inc, 1992), pp. .

[24] D. R. Cyr, R. E. Continetti, R. B. Metz, D. L. Osborn, and D. M. Neumark, J. Chem. Phys. **97,** 4937 (1992).

[25] R. E. Continetti, D. R. Cyr, R. B. Metz, and D. M. Neumark, Chem. Phys. Lett. **182,** 406 (1991).

[26] T. Okada and J. Hata, Mol. Phys. **43,** 1151 (1981).

[27] K. P. Huber and G. Herzberg, *Molecular Spectra and Molecular Structure. IV. Constants of Diatomic Molecules* (Van Nostrand Reinhold Co., New York, 1979).

[28] S. Bakin and J. O. Stoner Jr., *Atomic Energy Level and Grotrian Diagrams Vol. 2* (North-Holland Pub. Co., New York, 1978).

[29] H. Choi, R. T. Bise, A. A. Hoops, and D. M. Neumark, J. Chem. Phys. (in preparation).

Appendix

Fortran Code for Phase-Space theory calculation

```
      program pst_c2c3

c     This program is designed to calculate P(E_T)ditribution using PST
c        theory, especially for C5-→ C2+C3


      real pst(10000), Eavl1(100), Eavl2(300)
   real amu(10), rho(10000)
   integer llmax(5),imu(10)

      open(unit=12, file='pst.out')
      write(*,*) 'excitation energy in eV ?'
      read(*,*) Eext
      write(*,*) 'Dissociation Energy in eV ?'
      read(*,*) Do
      write(*,*) 'step size in cm-1 ?'
      read(*,*) step
      write(*,*) 'peak height '
      read(*,*) peak

c     Lennard-Jones potential is used to find the centrifugal barrier.
      write(*,*) 'value of C6 in eV A^6 ?'
      read(*,*) multi
      write(*,*) 'Cheking progress every rr step?'
      read(*,*) rr


C     rotational constant and vibrational frequencies for C3

   B1 = 0.4305
   amu(1) = 1224.5
   amu(2) = 2040.02
   amu(3) = 63.41
   amu(4) = 63.41

C     rotational constant and vibrational frequencies for C2
      B2 = 1.8198
      amu(5) = 1854.71

   rumass = 14.4
```

```
do i= 1,5
imu(i) = Nint(amu(i)/step)
enddo


Eavl = (Eext-Do)*8065.479
nmax = Nint(Eavl/step)


pstmax = 0.0
do nl = 1,nmax
pst(nl) = 0.0
enddo

do ij = 1, nmax
rho(ij) = 0.0
enddo
rho(0) = 1.0

do ii = 1, 5
  do jj = imu(ii), nmax
        rho(jj) = rho(jj)+rho(jj-imu(ii))
  enddo
enddo
write(*,*) nmax
do j = 0, nmax

Eavl1(j) = Eavl - j*step*1.0
kmax = sqrt(Eavl1(j)/B1+0.25)-0.5

if (Nint(j/rr)-j/rr.eq.0.0) write(*,*) j, Eavl1(j)

do k = 0, kmax

Eavl2(k) = Eavl1(j) - B1*k*(k+1.0)
kkmax = sqrt(Eavl2(k)/B2+0.25)-0.5

do kk = 0, kkmax
Et = Eavl2(k) - B2*kk*(kk+1.0)
m = Nint(Et/step)

c6 = multi
llmax=sqrt(910.3748368*rumass*c6**0.33*(Et/8065.479)**0.66+0.25)-.5

if (llmax.le.abs(k-kk)) goto 100
if (llmax.ge.abs(k+kk)) then
```

```
            pst(m) = pst(m) + (1 + k + kk - abs(k-kk))*rho(j)
                    else
        pst(m) = pst(m) + (llmax() - abs(k-kk) + 1)*rho(j)
                   endif
    if (pst(m).gt.pstmax) pstmax = pst(m)

100 enddo

    enddo
    enddo

    write(*,*) pstmax
    do nn=1,nmax
    write(12,*)nn*step/8065.479,pst(nn)*peak/pstmax
    enddo

    stop
    end
```